Universitat
Autònoma
de Barcelona

New micro pattern gas detector for x-ray diffraction experiments in the sub-millisecond time scale

Tesis doctoral – Departament de Física
Universitat Autònoma de Barcelona, 2007

Autor:
Ferran Fernàndez Banqué

Directora:
Inmaculada Ramos Lerate

Tutor:
Ramón Pascual de Sans

Als meus pares. Aquesta tesi és
el punt i final d'anys d'esforços
en la meva educació.

A la Maria, per la seva
paciencia i els seus ànims.

Agraïments

En primer lloc vull agrair molt especialment a Inmaculada Ramos la direcció d'aquesta tesi i els consells que, com a directora i com a amiga, m'ha sabut donar en els moments adequats. Així mateix agraeixo la tutela de la tesi a Ramón Pascual. També vull agrair molt especialment la confiança i els consells rebuts de Joan Bordas. Ell és, de fet, el culpable de que em decidís a fer el doctorat.

Agraeixo a David Beltrán, Joan Carles Guilmar i Bern Saló l'esforç i temps que han dedicat al prototip i a aquesta tesi. També agraeixo el suport i l'esforç de les persones que m'han ajudat posant els medis necessaris per tal que aquest treball arribés a bon port: Gemma Rosas, Toni Pérez, Francesc Sentís, Lluís Galindo,... i molt especialment a l'Enric Vinyals i al Ramón Escribà.

Agraeixo molt especialment els consells, el suport, el temps, els ànims, les bromes, els cafès i les partides d'AOM dels bons amics que he fet al sincrotró: el Zeus, el Joan, la Felisa, el Nico, el Jordi, el Pep i el Carles. Sense ells ho hagués aconseguit igualment, però m'hagués costat molt més.

Fora del sincrotró, he d'agrair als meus pares i a la Mariona, el suport, els ànims, les patates fregides i moltes altres coses que m'han facilitat la feina durant aquests quatre anys.

Per concloure, voldria agrair tot el que la Maria ha fet per mi animant-me, suportant-me, ajudant-me,... En definitiva, estant sempre al meu costat.

Preface

We present the design, development and test of a new detection system optimized to carry out time-resolved x-ray diffraction experiments in the sub-millisecond time scale at synchrotron facilities. This work covers a part of the research activities of the Ph. D training of the Universitat Autònoma de Barcelona (UAB) which I have carried out at the Synchrotron Light Laboratory (LLS). This research is supported by the “Departament d’Universitats, Recerca i Societat de la Informació, i el Fons Social Europeu” and by the “Ministerio de Educación y Ciencia” (Grant FPA2003-05050).

The document is organized as follows. The first chapter contains an introduction to the synchrotron light and their production. The requirements for the new detector and the detection technology for time resolved x-ray diffraction experiments are also presented.

The second chapter is concerned to the gas ionization chambers. It sketches the characteristics of x-ray detection with these devices, studying in deep the non basic topics of this field. An outlook of the past and present gas-filled detectors for x-ray detection is also presented.

In the third chapter, the new detector is presented. Firstly, an introduction of its structure and principle of operation is given. Secondly, the building process is described, focusing on its limitations and constrains. In the last section of this chapter, the readout electronics and DAQ that are going to be used for the detector are studied.

The simulations of the new detector are addressed in chapter four. In it, the spatial resolution is first simulated as a function of different parameters. Secondly, the 3D simulations are presented. These cover the mesh transparency (see later); the avalanche and signal development; and, the drift of the avalanche ions. The third section is dedicated to the simulation of the detector capacitances. These concern the crosstalk and the pulse noise.

The fifth chapter is dedicated to the optimization of the new detector. The relations between the detector parameters and the detector features are first presented. After that, the decision process of each parameter is explained.

In chapter six, the experimental work is presented. Firstly, the characterization work is described. The second section covers the setups of both, the detector and the experimental tests. In the third section, the x-ray detection tests and their results are illustrated. The forth section is dedicated to the simulation of the characterized detector.

Finally, the conclusions of this work are summarized in chapter seven.

Contents

1.Introduction

The detector proposed in this work aims to increase the detection capabilities required by some experiments performed at synchrotron light facilities. In this chapter we first briefly describe the synchrotron light and its production. After that, the requirements for the position sensitive detectors used to carry out *Small Angle X-ray Scattering* (SAXS) experiments at synchrotrons are introduced. Finally, a brief introduction to the detector technology for time resolved diffraction experiments is given.

What is the synchrotron light?

The synchrotron light, or synchrotron radiation, is the electromagnetic field radiated by accelerated charged particles. This effect becomes important for relativistic particles; $\gamma >> 1$ (γ is the relativistic constant). At relativistic energies, the radiation is emitted in a cone with an opening angle $\sim 1/\gamma$ in the direction of the velocity. In order to have large accelerations and γ, particles with small rest masses have to be used; i.e. electrons

With the intention of driving the particles to the relativistic regime, high electric fields are used. However, the energy that present devices can give to a charged particle that crosses the electric field of the device one time is much smaller than required to produce synchrotron radiation. Therefore, the particle needs to be recirculated through the electric field many times. This can be done with high magnetic fields that accelerate centripetally the particles to confine them in circular trajectories while an electric field drives them to the required energy.

What is a synchrotron light facility?

A synchrotron light facility is an installation that accelerates electrons to very high energies (typically few GeV) and storages them in a closed orbit by means of magnetic fields with the intention of producing synchrotron radiation.

The electrons are usually generated by an electron gun which delivers the particles to a linear accelerator; the *linac*. This device drives the electrons to an intermediate energy before injecting them to the so-called *booster*.

The booster is an accelerator that accelerates the electrons to their final energy using a *radio-frequency*. Their trajectory is maintained during the increase of energy by different bending magnets; whose field intensity is synchronized with the energy of the electron beam.

Finally, the electrons are injected in the storage ring where the particles are confined in a closed orbit. The accelerations they suffer produce the synchrotron radiation. The loss of energy of the electron beam due to the emission of synchrotron radiation is recovered by radio-frequencies. The storage ring is composed not only by bending magnets and radio-frequencies.

It also has a set of magnets that focuses and maintains the beam in its orbit. These are typically the quadrupoles and sextupoles.

In order to enhance the radiation flux, many small bending magnets can be placed one after the other in straight sections. The magnetic field is oriented alternatively to maintain the electrons around the trajectory (approximately straight). These arrays of magnets are the so-called *insertion devices* (ID). The radiation of ID is emitted in the forward direction adding the flux generated at each magnet. Depending on the period length and magnetic field, the radiation of each period interferes with the radiation of the others (*undulator*) or not (*wiggler*). In the case of an undulator, the constructive interference produces very intense peaks at certain energies.

The synchrotron light produced at the bending magnets or at the insertion devices is delivered to the *beamlines*. The beamlines are typically formed by three different rooms: the *optical hutch*, the *experimental hutch* and the *control room*. The first one prepares the radiation for the experiment. In it, the synchrotron light is focalized and the desired energy bandwidth is chosen. The experimental hutch is where the experiment takes place. Mainly, it has the sample environment and the detector. Finally, the control room is used to control the characteristics of the radiation (optical hutch) and the experiment and detection conditions (experimental hutch).

Requirements for the detector

The detector proposed in this work is designed to carry out one of the most demanding techniques used at synchrotrons, in terms of detector requirements: the time resolved SAXS. SAXS is a useful and complementary method for determining the size, size distribution and structure of a wide range of non-crystalline (or semi-crystalline) materials in the range of 2-200 nm (low scattering angles 1-10°). It covers a large variety of samples such as polymers, liquid crystals, oils, suspensions or biological samples like fibers or protein molecules in solution, it can solve structures. Thanks to the high flux of the present synchrotron light facilities, the technique can be used simultaneously with methods that influence and/or change the samples' structural characteristics in a time-resolved manner. This allows the observation of the changes in the structural characteristics.

Characteristic	Required specification
Spatial resolution	250µm x 250µm
Nº of pixels	1800 x 1800
Global count rate	10^8 Hz
Local count rate	$5 \cdot 10^5$ Hz/mm^2
Frame rate	> 10^3 Hz
Dynamic range	> 10^6
Sensitivity	1 photon/pixel
Typical energy	10 keV

Table 1. 1 Detector requirements for x-ray diffraction experiments [WALENTA1991].

In contrast to the rapid development of sources, de development of detectors for synchrotron radiation has been more modest. Therefore, there is a gap between the capabilities of modern synchrotrons to produce high photon fluxes and the ability of detectors to measure the delivered photons. In 1991 guideline specifications for a suitable detector for synchrotron x-ray diffraction were written in the European Workshop on X-Ray Detectors for Synchrotron Radiation Sources [WALENTA1991]. These are shown in **Table 1. 1**. At synchrotrons, a detector satisfying these specifications would fulfill the requirements, not only of x-ray diffraction but also for x-ray scattering and imaging for dynamic experiments [LEWIS2003].

Detector technology for time resolved diffraction experiments

For more than 90 years *Multi Wire Proportional Counters* (MWPC) have served as a detector for x-ray diffraction experiments requiring 2D photon counting. However, the distances between wires limit the count rate and spatial resolution capabilities of these devices. This limitation is reduced in *Micro Pattern Gas Detectors* (MPGD).

“Introduced at the end of 1980s, micro-pattern gas detectors perform much better that classic wire chambers (…) They possess unique combination of features such as: spatial resolution of less than 100μm, rate capability of higher than 10^5 Hz/mm^2 at a gain of about 10000, time resolution down to 3ns and good aging properties. These set of features together with cheap and reliable manufacturing technology makes MPGD a good candidate to fill the gap between solid state vertex detectors and large wire chambers” [SHEKHTMAN2002]. However, two recurrent problems arise with MPGD: a slow degradation under continuous irradiation (aging) and the rare but often damaging discharges [SAULI2002]. Both effects must be reduced prior to routine use of MPGD at synchrotron light facilities.

In the last years a candidate to fulfill the requirements mentioned above has appeared: the pixel detectors. They are based on a chip containing an array of semiconductor diodes bump bonded to another chip containing an array of readout pixels. Each pixel has the necessary electronics to store the intensity during he exposure and read it out. The PILATUS detector has demonstrated recently its capabilities for its use at protein crystallography diffraction experiments [BRÖNNIMANN2006]. However, these detectors are far from being used for SAXS experiments in the sub-millisecond time scale because the readout technology limits their frame rate.

2.Gas ionization chambers

Gas ionization chambers, and specially the proportional counter, are deeply studied in the literature [KNOLL2000; LEO1994]. They are versatile detectors able to detect, depending on their characteristics and modes of operation, radiation and particles of a wide range of energies.

In this chapter we describe the principles of operation of the gas ionization chambers focusing on the most relevant mechanisms involved in the detection process. This knowledge is necessary to understand, simulate and optimize the proposed detection system. We first describe the primary electron production, looking in deep the mechanisms involved in the photoelectric effect. After that, we describe the transport of charged particles in gases, the electron multiplication process, the requirements of the gas mixture and the features which concerns to the signal. As a final point, we illustrate how the ionization chambers are used for two dimension detection, covering the *Multi Wire Proportional Counter* (MWPC) and the *Micro Pattern Gas detectors* (MPGD). We study the MPGD in deep since the detector geometry we propose in this work belongs to this family of detectors.

Principle of operation

A gas ionization chamber consists of a closed volume filled with the adequate gas containing anode/s and cathode/s. When a particle comes into the volume, it interacts with the gas ionizing the atoms of the gas. The generated electrons, *primary electrons*, drift to the anode which detects the signal. If the *electric field* (E) is intense enough, the electrons are highly accelerated and they ionize again the gas. Under these conditions, the number of electrons grows rapidly forming what is known as *avalanche*. The gas proportional counters have a constant ratio between the initial and final number of electrons in the avalanche.

2.1. Primary electron production: the photoelectric effect

The particle can interact with the gas via different mechanisms depending on different factors such as: the detected particle; its energy; or, the gas mixture. We are interested in detecting x-rays of energies between 8keV and 12keV. In this range of energies and for typical gases like Ar the interaction process that prevails is the *photoelectric effect* (see **Figure 2.1**).

In this section the basics of the energy deposition are first described. The generalities of the photoelectric effect, the photoelectron characteristics and the ion de-excitation mechanisms are described in subsections 2.1.1., 2.1.2 and 2.1.3, in that order.

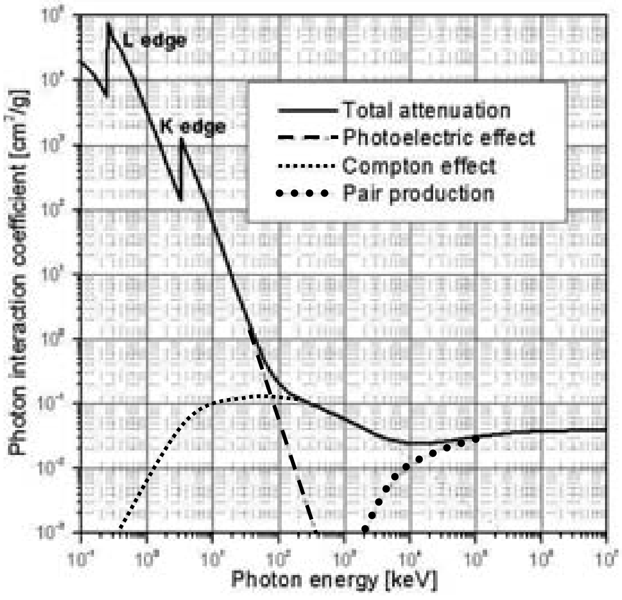

Figure 2.1 Photon interaction coefficients with Argon [NIST2003].

Mean number of electron-ion pairs created

The number of *primary electron-ion pairs* (N_0) depends on the *energy that the detected particle has deposited on the gas* (ΔEnergy) and on the *average energy per ionization of the gas* (W).

$$N = \frac{\Delta Energy}{W} \tag{2.1}$$

Note that W is not equal to the ionization potential of the gas because part of the energy deposited in the gas is lost in excitation (see Table 2.1). The ionization potential is the lowest binding energy of the atom. It corresponds to the outer atom shell; (see **Table 2. 3**).

Gas	W [eV]	Excitation potential [eV]	Ionization potential [eV]
H_2	37	10.8	15.4
He	41	19.8	24.6
N_2	35	8.1	15.5
O_2	31	7.9	12.2
Ne	36	16.6	21.6
Ar	26	11.6	15.8
Kr	24	10.0	14.1
Xe	22	8.4	12.1
CO_2	33	10.0	13.7

Table 2.1 Mean ionizing energy, excitation potential and ionization potential for various gases [LEO1994].

If a gas mixture is used, W is calculated through a weighted average of the W of the different gas molecules. However, if the excitation potential of one gas component is higher than the ionization potential of another one, an excited molecule of the first component can ionize a molecule of the second component. Under these conditions, W presents a lower value than the weighted average of W. This is the so-called *Penning effect* [PENNING1934].

Fano factor

In gas ionization chambers, the energy of the detected particle is proportional to the number of primary electron-ion pairs (N_0). Therefore, the *variance of N_0* ($\sigma(N_0)$) sets a limit for the energy resolution of the detector. **Equation 2.1** implies a variation of N_0 equal to zero. Nevertheless, every ionization or excitation is ruled by Poisson statistic, that implies a variation of N_0 equal to the square root of N_0. The *Fano factor* (F) is an experimental value between 0 and 1, introduced to correct this discrepancy

$$\sigma(N_0) = \sqrt{F \cdot N_0} \qquad (2.2)$$

F varies from 0.05 to 0.20 for most gas mixtures (see **Table 2.2**). The gas mixtures which have the lower values of F are the ones that present a large Penning effect. This is because the larger the proportion of energy used in ionizations is (large Penning effect); the lower the amount of energy ruled by the Poisson statistics is.

Gas	Fano factor
Ne	0.17
Ar	0.17
Xe	0.17
$0.995 \cdot Ar + 0.005 \cdot C_2H_2$	0.09
$0.995 \cdot Ne + 0.005 \cdot Ar$	0.05

Table 2.2 Fano factor for different gas mixtures [KNOLL2000].

2.1.1. Generalities of the photoelectric effect

The photoelectric effect consists on the absorption of an x-ray by an atom. The energy deposited is given to an electron of a bound shell that is ejected from the atom. This electron, called *photoelectron,* is released with the energy of the x-ray minus the *binding energy* and interacts with the gas molecules ionizing and exciting them. The atom that has absorbed the x-ray rearranges its electron configuration to fill the inner shell vacancy. The de-excitation mechanism generates more electron-ion pairs (see section 2.1.3). At the end, the x-ray energy is totally transferred into excitation and ionization of the surrounding atoms.

The binding energies of the K, L, M, N, and O shell of the Ar, Kr, and Xe are shown in **Table 2. 3**. The data is given for these gases because, as we will see in section 2.4, the gas mixtures we are interested in are mainly composed by Ar, Kr and Xe.

Element	K 1_s	L, 2_s	$L_2\ 2_{p1/2}$	$L_3\ 2_{p3/2}$	M, 3_s	$M_2\ 3_{p1/2}$	$M_3\ 3_{p3/2}$	$M_4\ 3_{d3/2}$	$M_5\ 3_{d5/2}$
Ar	3205.9	326.3	250.6	248.4	29.3	15.9	15.7		
Kr	14326	1921	1730.9	1678.4	292.8	222.2	214.4	95.0	93.8
Xe	34561	5453	5107	4786	1148.8	1002.1	940.6	689.0	676.4

Element	N, 4_s	$N_2\ 4_{p1/2}$	$N_3\ 4_{p3/2}$	$N_4\ 4_{d3/2}$	$N_5\ 4_{d5/2}$	$N_6\ 3_{f5/2}$	$N_7\ 3_{f7/2}$	O, 5_s	$O_2\ 5_{p1/2}$	$O_3\ 5_{p3/2}$
Kr	27.5	14.1	14.1							
Xe	213.2	146.7	145.5	69.5	67.5	-	-	23.3	13.4	12.1

Table 2. 3 Electron binding energies, in electron volts, for Ar, Kr and Xe [THOMPSON2001].

Cross section

The photoelectric effect is found to be predominant for electromagnetic radiation of low energy and atoms of high atomic number. Its *photon interaction coefficient* (μ) is

$$\mu = P1 \cdot Z^{b} / Energy_{\gamma}^{m} \qquad (2.\ 3)$$

where b and m are constants that depends on the *x-ray energy* ($Energy_\gamma$) and have typical values of 5 and 3 respectively. P1 is a constant (different for each shell regime). In **Figure 2. 2, Figure 2. 3** and **Figure 2. 4** we show the Ar, Kr and Xe, respectively.

In **Figure 2. 2, Figure 2. 3** and **Figure 2. 4** some discontinuities in the photon interaction coefficient can be observed at $Energy_\gamma$=$Energy_b$; where $Energy_b$ is the *binding energy of the electron on its atom* $shell_b$. This is because if $Energy_\gamma$>$Energy_b$ the interaction with an electron of a $shell_b$ is possible. But if $Energy_\gamma$<$Energy_b$, this interaction can not take place.

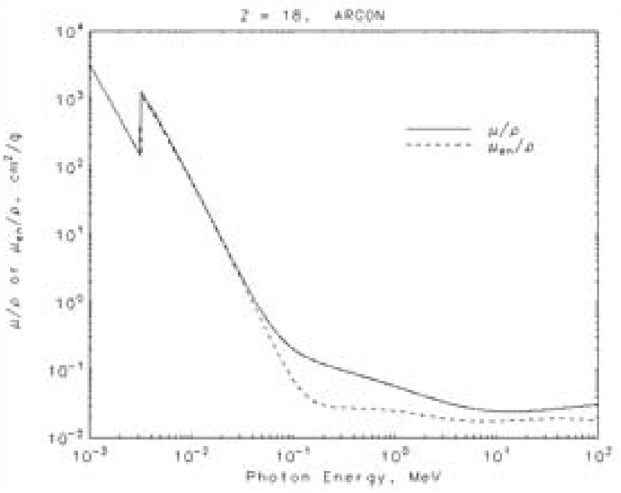

Figure 2. 2 Photon interaction coefficient with Argon [NIST2003].

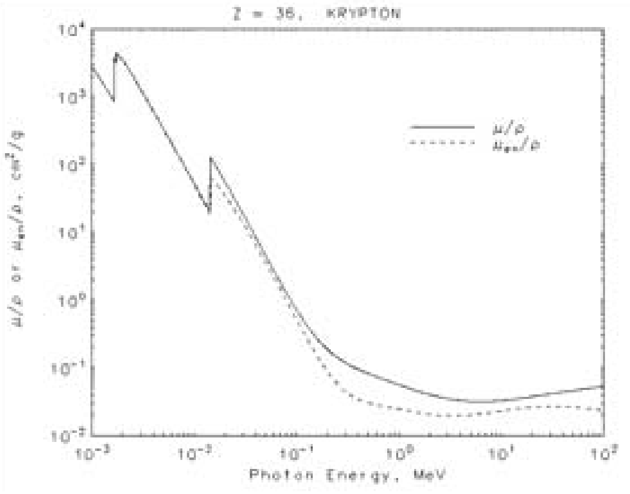

Figure 2. 3 Photon interaction coefficient with Krypton [NIST2003].

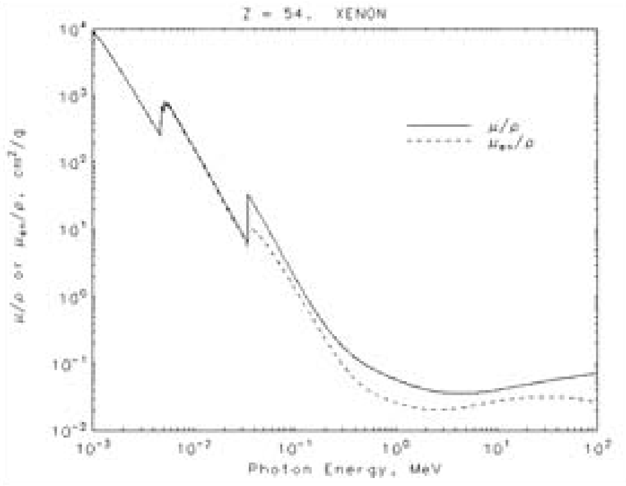

Figure 2. 4 Photon interaction coefficient with Xenon [NIST2003].

Decay constant

The photoelectric effect attenuates the beam intensity exponentially (see **Figure 2.5**) because this interaction absorbs the incident x-ray. This exponential decay is characterized by the probability of interaction per unit length of the x-ray in the gas mixture. This is obtained from the photon interaction coefficient (μ).

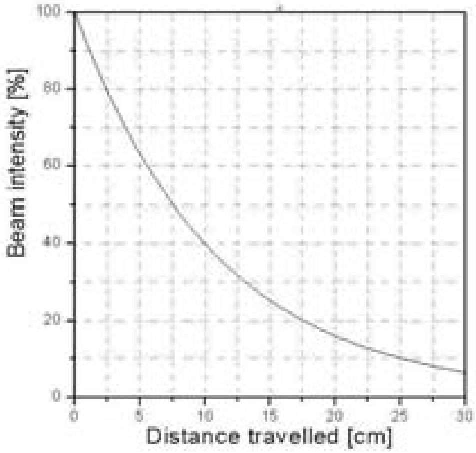

Figure 2.5 10 keV x-ray simulated beam intensity as a function of the distance traveled in Ar 90% + CO_2 10% (1atm). The curve follows an exponential decay with decay constant 0.0922cm^{-1}. The author has made the simulations with Garfield and Magboltz [VEENHOF2001; BIAGGI2000].

Proportion of shell photoionization

The photoelectric effect can occur for all the electrons in the atom, but the probability of interaction is higher for electrons of inner shells. The photon interaction coefficient of the different shells and subshells is required for the simulation of the s-ray detection. They can be found in the literature [YEH1985] for $Energy_\gamma$<8keV. This range of energy is lower than the one of our interest. Therefore, the author computes these coefficients extending the known data. Firstly, the photon interaction coefficient is fitted with **Equation 2.3** for each shell regime (see **Figure 2. 6**). After checking that the m constants are the same, the different values of P1 are obtained. The calculated proportions between photon interaction coefficients for the K, L and M shells are shown in **Table 2. 4** for Ar, Kr and Xe.

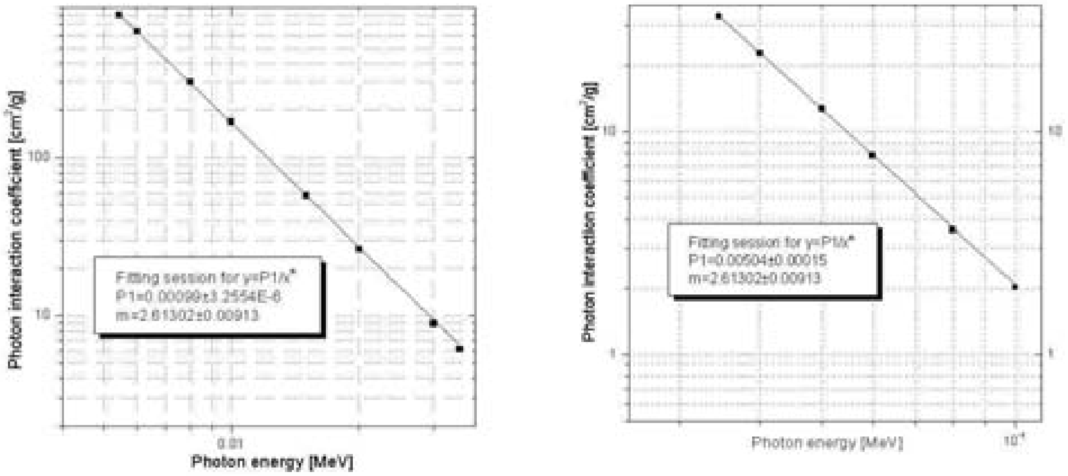

Figure 2. 6 Photon interaction coefficient of Xenon for two ranges of x-ray energies (data obtained from [NIST2003]). In the left figure, the x-rays can produce photoelectric effect with electrons from all the shells but the K. In the right figure, the x-rays can ionize electrons from all the shells. The proportion between the photon interaction coefficient of K and the other shells is (0.00504-0.00099)/0.00504=0.8.

Element	K shell	L shell	M and other shells
Ar	0.89	0.11	0.00
Kr	0.85	0.13	0.02
Xe	0.80	0.16	0.04

Table 2. 4 Photoionization coefficient proportion between shells for Ar, Kr, and Xe.

Similarly, the author computes the photoionization cross section proportions between the different L subshells for Kr and Xe (see **Table 2. 5**). It is not possible for Ar since the energies are out of the energy range of the data.

Element	L_1	L_2	L_3
Kr	10%	28%	62%
Xe	14%	28%	58/

Table 2. 5 L subshell photoionization proportion for Kr and Xe at x-ray energies close to the L binding energy.

2.1.2. Photoelectron characteristics

After a photoelectric effect, a photoelectron is released. We describe in this chapter its characteristics: energy; emission angle; and, range. These characteristics determine the primary electron cloud size after the photoelectric effect. It will be seen that this magnitude conditions the spatial resolution of the detector.

Photoelectron energy

The *final kinetic energy* (Energy_e) of the photoelectron is

$$Energy_e = Energy_\gamma - Energy_b \tag{2.4}$$

Photoelectron direction

The angular distribution of the emitted photoelectrons is ruled by the conservation of energy and momentum. Therefore, it depends on the Energy_γ. The distribution of the *angle formed between the directions of the incident x-ray and the photoelectron* (φ) is proportional to

$$\frac{d\sigma}{d\Omega} \propto \frac{\sin^2\varphi}{(1-\beta\cdot\cos\varphi)^4} \tag{2.5}$$

where β is the ratio between the velocity of the released photoelectron and the speed of light.

The author computes the distribution of φ for different x-ray energies with Ar (see **Figure 2.7**).

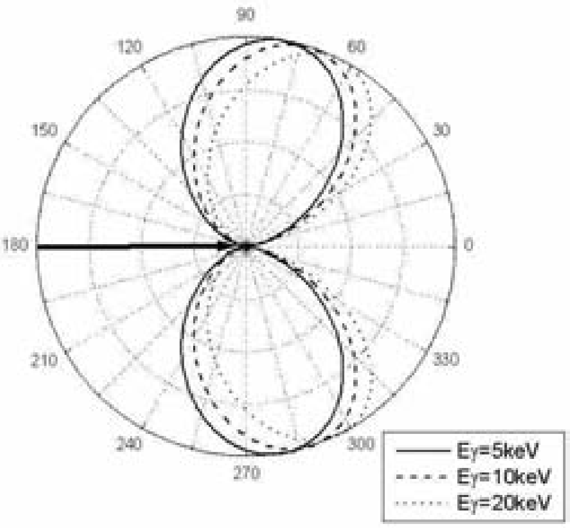

Figure 2.7 Angular distribution of the photoelectrons for different incident x-ray energies. The target is an Argon atom. The angles of maximum probability are φ_{max}=80º(280º), 72º(288º), and 63º(297º) for $Energy_{\gamma}$=5keV, 10keV, and 20keV respectively.

Electron range

An electron that is released with a given kinetic energy travels along the gas ionizing and exiting the gas atoms. The *electron range* R_e is the distance between the starting position of the electron and its final position; where it is completely thermalized. The path of the electrons is chaotic due to the multiple scattering. Therefore, R_e is two or three times shorter than the length of the electron path.

Different approximations of R_e based on experimental data can be found in the literature [KATZ1952; BATEMAN1980; WEBER1964]. Among all the fits, the one provided by Weber (see **Equation 2.6, Figure 2.8** and **Table 2. 6**) covers the range of energies we are interested in 5-20 keV.

$$R_e = 0.5371 \cdot E_e \left(1 - \frac{0.9815}{1 + 3.123 \cdot Energy_e} \right) \tag{2.6}$$

where $Energy_e$ is the electron kinetic energy expressed in MeV and R_e is given in g/cm^2.

The author computes the electron ranges for electrons with kinetic energy from 0.3keV to 12keV in pure Ar, Kr, and Xe gases (see **Figure 2.8** and **Table 2. 6**).

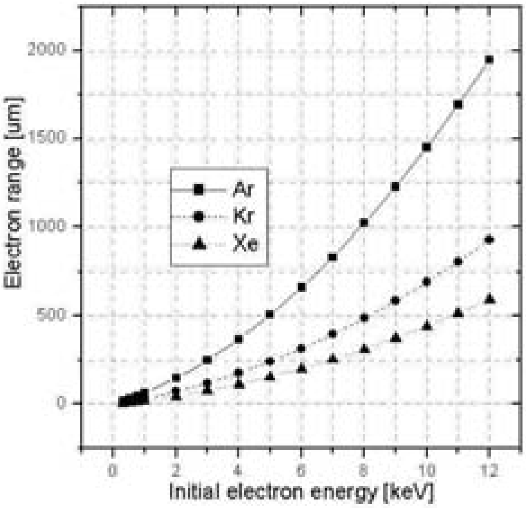

Figure 2.8 Electron range for different gases at normal conditions (1 atm; 290ºK) as a function of the initial electron kinetic energy ($Energy_e$).

$Energy_e$ (keV)	Range in Ar (µm)	Range in Kr (µm)	Range in Xe (µm)
0.3	18	8	5
0.5	30	14	9
0.75	47	22	14
1	65	31	20
2	148	71	45
3	249	119	76
4	368	176	112
5	505	241	154
6	660	315	201
7	832	397	253
8	1021	487	311
9	1227	586	374
10	1450	692	442
11	1691	807	515
12	1947	930	593

Table 2. 6 Electron ranges in different gases at normal conditions (1atm and 290ºK).

2.1.3. Ion de-excitation processes

The photoelectric effect leaves the atom with an empty place on its shells. This excess of energy can be released through three different processes: the *fluorescence,* the emission of an *Auger electron,* or the *Croster-Kronig effect.*

In the first process, the empty place is filled quickly (<10^{-14}s) with an electron of an outer shell of the atom, what generates a characteristic x-ray; the fluoresence. The energy of this x-ray is equal to the difference of binding energies of the two shells. For Argon, the fluorescence emission lines have energies of 2957.70eV, 2955.63eV and 3190.5eV for $K\alpha_1$, $K\alpha_2$ and $K_{\beta,}$ respectively [THOMPSON2001]. $K\alpha_,$ refers to the energy difference between shells L_3 and K_1, $K\alpha_2$ refers to the energy difference between shells L_2 and $K_{1,}$ and $K_{\beta,}$ refers to the energy difference between shells M_3 and K_1. A scheme of these transitions is shown in **Figure 2.9**. In **Table 2. 7** the energies of the Ar, Kr and Xe x-ray emission lines are presented.

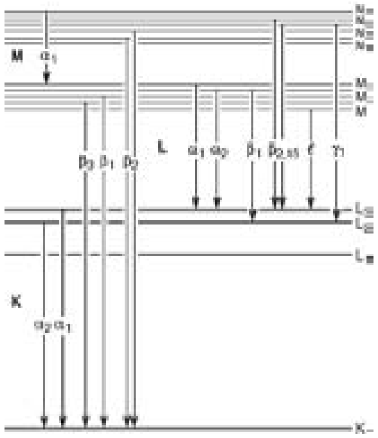

Figure 2.9 Fluorescence transitions scheme [THOMPSON2001].

Element	$k\alpha_,$ (eV)	$k\alpha_2$ (eV)	$k\beta_{113}$ (eV)	$L\alpha_{12}$ (eV)	$L\beta_,$ (eV)
Ar	2957.70 (100)	2955.63 (50)	3190.5 (10)		
Kr	12649 (100)	12598 (52)	14112 (14)	1586.0 (111)	1636.6 (57)
Xe	29779 (100)	29458 (54)	33624 (27)	4109.9 (100)	

Table 2. 7 x-ray emission energies for Ar, Kr and Xe. The relative line intensity is shown between brackets [THOMPSON2001].

In the second process, the shell vacancy is filled through a rearrangement of several electrons from higher shells ending up with the emission of an Auger electron. The energy of the Auger electron is approximately equal to the difference of binding energies of the initial and final shell vacancies minus the binding energy of the Auger electron. In **Figure 2.10** we show the principal Auger electron energies [THOMPSON2001] and [AKSELA1984].

Finally, the Coster-Kronig transition involves the rapid transition of an electron between two adjacent levels within the same shell with the excess of energy being removed through emission of another electron, from a higher energy state. It is similar to the Auger emission, but the initial and final vacancy belongs to the same shell. This process is usually not considered as "de-excitation" since it does not fill the shell vacancy.

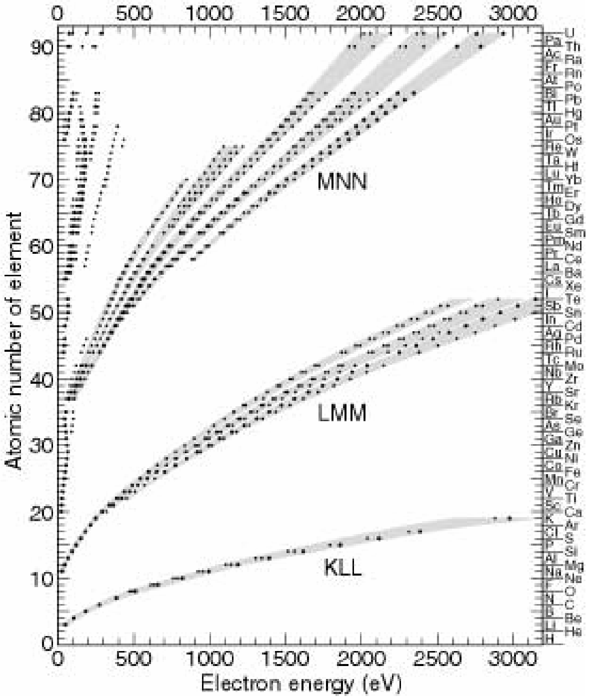

Figure 2.10 Principal Auger electron energies. The different families are denoted by labels of form WXY, where W is the shell from in which the original vacancy occurs, X is the shell from which the W vacancy is filled, and Y is the shell from which the Auger electron is ejected [THOMPSON2001].

Fluorescence, Auger and Coster-Kronig yields

The lifetime τ of a de-excitation is related to the natural width Γ of that level by the uncertainty principle

$$\Gamma \cdot \tau = \hbar \qquad (2.7)$$

Γ is the sum of the partial de-excitation processes; fluorescence, Auger and Coster-Kronig.

$$\Gamma = \Gamma_r + \Gamma_a + \Gamma_c \qquad (2.8)$$

Yields for the various processes are defined as follows

$$w_i = \Gamma_r / \Gamma$$ (2.9) Radiative/fluorescence yield

$$a_i = \Gamma_a / \Gamma$$ (2.10) Auger yield

$$f_{i,j} = \Gamma_c / \Gamma$$ (2.11) Coster-Kronig yield

where i refers to the initial vacancy shell (K, L1, L2 or L3). In the Coster-Kronig yield, j=213 refers to the final vacancy shell (L2 or L3). For simplicity we only consider de-excitations from the K and L shells. This simplification is justified since the probability of photoelectric effect for the other shells is very low (<3% see **Table 2. 4**). In **Table 2. 8** we show the different yields for Ar, Kr and Xe are shown.

Element	w_k	a_k	w_1	a_1	f_{12}	f_{113}	w_2	a_2	f_{213}	w_3	a_3
Ar	0.118	0.882	0.00018	0.066	0.31	0.62	0.00022	1	-	0.00022	1
Kr	0.643	0.357	0.0041	0.199	0.27	0.52	0.02	0.88	0.1	0.022	0.978
Xe	0.891	0.109	0.046	0.488	0.19	0.28	0.083	0.736	0.154	0.085	0.915

Table 2. 8 Fluorescence, Auger and Coster-Kronig yields for the K and L shells for Ar, Kr and Xe [KRAUSE1979; SLIVINSKY1972; BAMBYNEK1972].

A scheme of the possible ways the energy can be deposited in a photoelectric effect is shown.

An x-ray enters into a volume filled with pure Ar gas (1atm and 290ºK). λ=0.1137cm^{-1}. Through photoelectric effect they ionize:

- 89% the K shell. A photoelectron is ejected: Energy$_e$=10000eV-Energy$_b$=6794.1eV; φ_{max}=100º or 260º; and, R$_e$=796µm. The K shell vacancy is filled through:
    - 88% Auger electron. An Auger electron is emitted. Energy$_e$=2660.5eV. R$_e$=217µm. The L$_{2,3}$ shell vacancy is filled.
    - 12% fluorescence from subshells:
        - 63% Kα_1. Characteristic x-ray: Energy$_\gamma$=2957.70eV and λ=0.305cm^{-1}. The L$_3$ shell vacancy is filled. The characteristic x-ray ionizes the L shell ($\simeq$100%) of another atom. Therefore a photoelectron is ejected: Energy$_e$=2957.70eV-E$_b$ and R$_e$=244µm. The L shell vacancy is filled.
        - 31% Kα_2. Characteristic x-ray: Energy$_\gamma$=2955.63eV and λ=0.305cm^{-1}. The L$_2$ shell vacancy is filled. The characteristic x-ray ionizes the L shell ($\simeq$100%) of another atom. Therefore a photoelectron is ejected: Energy$_e$=2955.63eV-E$_b$ amd R$_e$=244µm.
        - 6% K$\beta_{1,3}$. Characteristic x-ray: Energy$_\gamma$=3190.5eV and λ=0.255cm^{-1}. The M$_{213}$ shells vacancy is filled. The characteristic x-ray ionizes the L shell ($\simeq$100%) of another atom. Therefore a photoelectron is ejected: Energy$_e$=3190.5-Energy$_b$ eV and R$_e$=270µm.
- 11% the L shell. A photoelectron is ejected: Energy$_e$=10000eV-Energy$_b$$\simeq$9750eV; φ_{max}=110º or 250º.; and, R$_e$=1393µm. The process starts again with initial x-ray energy equal to 9750eV.

In this example, the L shell vacancies are effectively filled $\simeq$100% through Auger electrons. Even though the probability of Coster-Kronig effect is higher for the L$_,$ de-excitation, they end up in Auger electrons in L$_2$ or L$_3$. The probability of a L shell de-excitation through the emission of a characteristic x-ray is ≤0.02%.

2.2. Transport of charged particles in gases

A charged particle under the effect of an electric field is accelerated along the field lines. In this section the drift velocity of electrons and ions and the diffusion of electrons are described. The mechanisms of recombination and attachment of primary electrons are also described.

2.2.1. Drift velocity

A charged particle that is moving under the effect of an electric field impacts the gas molecules. The particle has an average velocity called *drift velocity* (u).

The electron drift velocity depends on both, the electric field (see **Figure 2.11**) and the gas mixture characteristics. The drift velocity is, in many gas mixtures, 5cm/µs for electric field intensities from few hundreds V/cm to thousands V/cm.

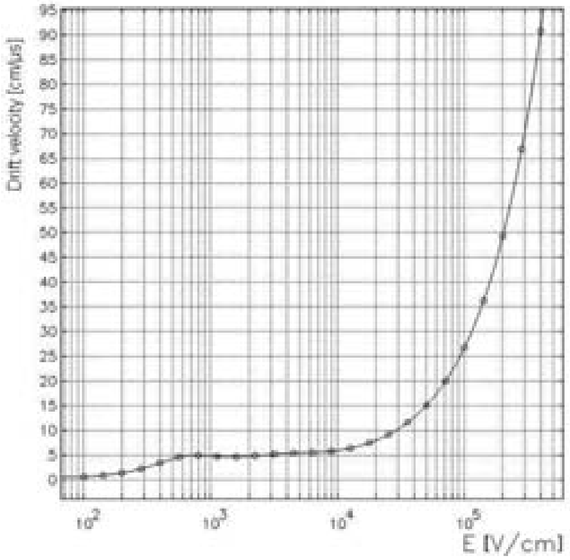

Figure 2.11 Simulated drift velocity of electrons as a function of the electric field. Gas mixture characteristics: Ar 90% + CO_2 10%; T=300ºK; and, 1atm. The author has made the simulations with Garfield and Magboltz.

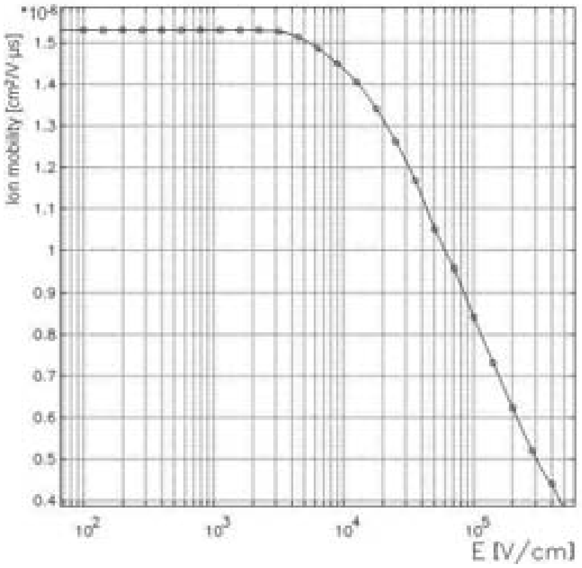

Figure 2.12 Simulated **i**on mobility as a function of the electric field. Gas mixture characteristics: Ar 90% + CO_2 10%; T=300ºK; and, 1atm. The author has made the simulations with Garfield and Magboltz.

The drift velocity of the ions is orders of magnitude lower than the drift velocity of the electrons, in the same conditions. For the major part of the gases used in proportional chambers and E/p values lower than few thousand V·cm^{-1}atm^{-1}, u/E is found to be constant (see **Figure 2.12**).

At this point it is useful to define the *mobility* (μ)

$$\mu = \frac{u}{E} \qquad (2.12)$$

2.2.2. Diffusion

In a gaseous environment and absence of electric field, free electrons diffuse uniformly from their original position. The rms longitudinal spread σ(x) is

$$\sigma(x) = \sqrt{2 \cdot D_x \cdot t} \qquad (2.13)$$

where D_x is the *diffusion coefficient* in the x coordinate and t is the time. The diffusion coefficient can be computed using the kinetic theory

$$D_x = {}^{u \cdot \xi}\!/_{3} \qquad (2.14)$$

where ξ is the *mean free path* of the particle.

Under the effect of an electric field, a traveling electron cloud is diffused

$$\sigma(x) = \sqrt{2 D_x l / u} = \sqrt{2l} \cdot \sqrt{D_x / u} \qquad (2.15)$$

where l is the *distance traveled by the particle* and u the drift velocity. For convenience we define the longitudinal and transverse diffusion coefficients; D_L and D_T.

$$D_{T,L} = \sqrt{2 \cdot D_x / u} \qquad (2.\ 16)$$

The reduced diffusion coefficients have units of μm/cm$^{1/2}$ as they are expressed as rms [μm] for square root of traveled unit length [cm$^{1/2}$]. For example, a group of electrons under an electric field of 10^4V/cm drifts in an "Ar 90% + CO_2 10%, T=300ºK and 1atm" environment. The transverse reduced diffusion coefficient is 293μm/cm$^{1/2}$ (see **Figure 2.13**). After having traveled 2cm, the electron cloud presents a Gaussian distribution with

$$\sigma_{transverse} = 293 \cdot \sqrt{2} = 415 \mu m \qquad (2.\ 17)$$

Roughly speaking, the higher the electric field is, the lower the mean free path is; and therefore, the lower the value of D is. However, in **Figure 2.13** some peaks can be observed. They are produced by the resonances in the cross section of the electron multiple scattering.

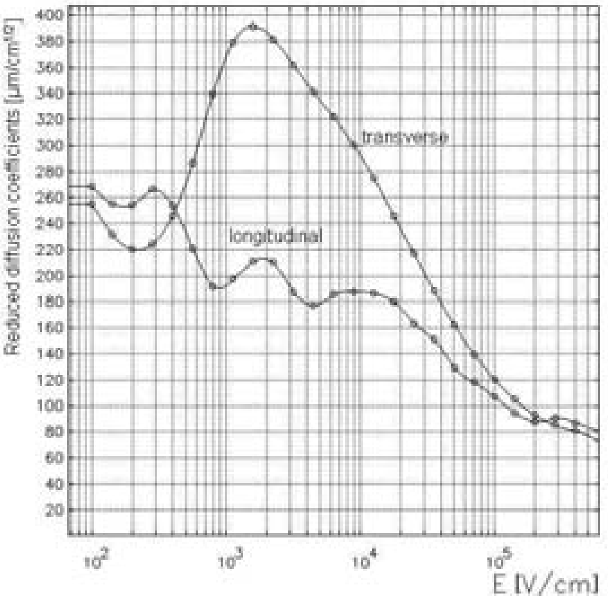

Figure 2.13 Simulated reduced diffusion coefficients as a function of the electric field. Gas mixture characteristics: Ar 90% + CO_2 10%; T=300ºK; and, 1atm.The author has made the simulations with Garfield and Magboltz.

2.2.3. Recombination and Attachment

It is important to have a high *number of primary electrons* (n) because the energy resolution and the amplitude of the detected signal are proportional to it. During the transport of the electrons two main processes decrease the number of primary electrons: the *recombination* and the *attachment*.

The recombination is the capture of a free electron by a positive ion followed by a photon emission. The recombination rate is proportional to the ions and electrons densities

$$\frac{dn_e}{dt} = -\psi \cdot n_e(t) \cdot n_i(t) \qquad (2.\ 18)$$

where n_e and n_i are the electron and ion densities, and ψ is the recombination coefficient.
The electron attachment is the capture of a free electron by an electronegative atom followed by a photon emission. This process is characterized by the *attachment coefficient* that is the average number of attachments per traveled unit length and electron (see **Figure 2.14**). The most common electronegative gases are: O_2, H_2O and CO_2. Noble gases present zero electronegativity.

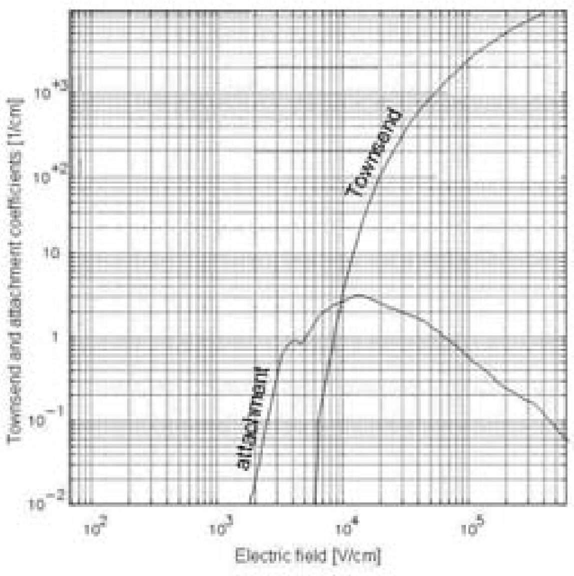

Figure 2.14 Simulated Townsend and attachment coefficients as a function of the electric field. In the next section we introduce the Townsend coefficient. Gas mixture characteristics: Ar 90% + CO_2 10%; T=300ºK; and, 1atm. The author has made the simulations with Garfield and Magboltz

2.3. Electron multiplication

In many cases, the signal generated by the primary electrons is not intense enough to be detected by the readout electronics. Consequently, the charge of the primary electron cloud must be augmented. This is done through the so called *avalanche* process. In this section the basics of this process are firstly described. Later four different aspects related to this process are described: the space charge; the “avalanche to streamer to spark” process; the gain vs. incoming rate; and, the resistive layer effects.

The primary electrons can ionize the gas, if the electric field is intense enough. Under these conditions, the number of electrons grows rapidly as every new electron ionizes again the gas and therefore an avalanche is formed (see **Figure 2.15**).

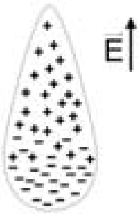

Figure 2.15 Avalanche drawing. The electrons and the ions drift in opposite directions

If the electric field is constant along the electrons path

$$n = N \cdot e^{\frac{x}{\xi}} \qquad (2.\,19)$$

where n is the number of electrons collected by the anode, N is the *number of electrons that reach the anode region*, and ξ is the *mean free path*.

At this point is useful to define the *Townsend coefficient* (α). α is the number of electron-ion pairs generated by one electron for a traveled unit length. It depends on the electric field (see **Figure 2.14**), the *temperature* (T), pressure, and the composition of the gas mixture.

$$\alpha = \xi^{-1} \qquad (2.\,20)$$

The *gain* (A) is

$$A = \frac{n}{N} \qquad (2.\,21)$$

A has a variance σ(A). For a constant electric field, the probability of having a gain A is ruled by the Fury distribution [KNOLL2000].

$$P(A) = \frac{\left(1 - \bar{A}^{-1}\right)^{A-1}}{\bar{A}} \qquad (2.\,22)$$

When the avalanche takes place, the electric field is distorted by the electric field that the electrons and mostly the ions generate. The electric field around each electron is different because it is affected by a different charge distribution. This effect is the so called *space charge* (see subsection 2.3.1). Consequently, α varies as the avalanche growths. Under these conditions, the *Polya distribution* [BYRNE1969] rules the gain

$$P(A) = \left(\frac{A(1-\theta)}{\bar{A}}\right)^{\theta} \cdot \exp\left(\frac{-A \cdot (1+\theta)}{\bar{A}}\right) \qquad (2.\,23)$$

where θ is a parameter in the range 0< θ <1. The variance of the Polya distribution is

$$\left(\frac{\sigma(A)}{\bar{A}}\right) = \bar{A}^{-1} + (1+\theta)^{-1} \qquad (2.\,24)$$

2.3.1. Space charge

The space charge effect is the reduction of the electric field in the multiplication region due to the presence of the electrons and ions. The space charge effects can be classified into voltage or rate induced [IVANIOUCHENKOV1998].

The voltage induced space charge effects refer to the effect that the avalanche ions produce to their avalanche. When an electron-ion pair is produced in an avalanche, the electron joins the avalanche head that moves in the opposite direction of the electric field. The ion drifts in the same direction of the electric field. The ion velocity is orders of magnitude lower than the electron velocity. It implies that the ion cloud is extended forming an *ion tail*, while the electron cloud travels and growths in a compact shape (see **Figure 2.16**). The ion tail reduces the electric field at the avalanche zone. As a result, the space charge limits the avalanche charge. Under these circumstances, the proportionality between the initial number of ion-electron pairs and the detected charge is lost [PESKOV2001].

The rate induced space charge effects are related to the electric field reduction generated by the ions of all the avalanches. This effect can be reduced, without decreasing the incoming particle rate, decreasing the ion drift time.

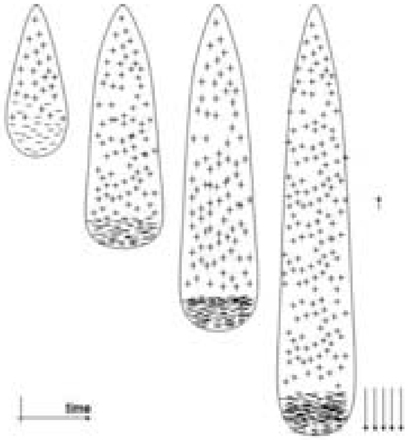

Figure 2.16 From left to right, four moments of the avalanche development.

When simulating an avalanche, two assumptions are made to simplify the calculation of the voltage induced space charge effects [LIPPMANN2001]. The first approximation only takes into account the electric field that the ions generate. The electron cloud has a uniform ball shape. The electrons in the front part of the ball are more accelerated downwards but the ones in the rear part are less accelerated and therefore, the overall effect is neutralized.

The second approximation consists on considering that the ions are fixed in their original position. This is justified since the ion velocity is two or three orders of magnitude lower than the electron velocity. Consequently, during the avalanche it is considered that the ions do not move.

2.3.2. "Avalanche to streamer to spark" process

It is experimentally well demonstrated that the avalanche growth is stopped at $n \simeq 10^8$ electrons; the so called *Raether limit* [RAETHER1964]. When the avalanche have reached the Raether limit, the electric field at the head and tail of the avalanche induces the fast growth of secondary avalanches (see **Figure 2.17**). At this point, a long, filament-like forward and backward charge propagation named *streamer* appears [BERG2000b; BRESSAN1999a]. In a uniform, strong electric field, the streamer propagates all the way trough the gap. The outcome of the process is the creation of a densely ionized channel between the anode and the cathode called *spark*. The dielectric breakdowns are a critical problem in MPGD as they are characterized by small structures with high electric fields that extend over a gap between the anodes and cathodes.

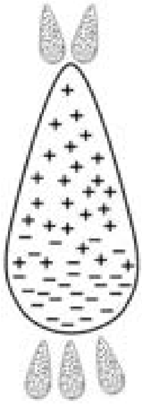

Figure 2.17 Drawing of an avalanche-to-streamer process.

The streamer can be self-quenched if the electric field in the head/tail is decreased enough. This self-quenching effect is typical for proportional counters, where the electric field is very intense only near the anode wire.

2.3.3. Gain vs. Incoming rate

In absence of incoming particles, the *spontaneous field emissions* limit the maximum voltage the detector can reach [BRESSAN1999a; IVANIOUCHENKOV1998]. If the incoming rate is increased, the discharges become more frequent; forcing a drop of the gain.

At low incoming rates, the sparks appear due to gain fluctuations and dielectric imperfections. The presence of dielectric material is critical for the discharges because the electric field is increased between the head of the avalanche and the dielectric material due to electric polarization. This excess of electric field can end up in a streamer that can promote a dielectric breakdown [FONTE1997].

In subsection 2.3.1 it has been seen that at high incoming rates, the gain is limited because the electric field generated by the ions reduces the multiplication field to the point that subsequent avalanches can not take place. This effect is reduced on the MPGD detectors since their ion drift times are reduced. The discharge mechanisms at high rates are under discussion. The author have tried to select the most supported theories [PESKOV2001; FONTE1997; FONTE11999b; BRESSAN11999a; IVANIOUCHENKOV1998; IVANIOUCHENKOV1999]. They can be classified in two groups: generation of secondary avalanches, and the emission of *jets* and *bursts*.

The total charge that the detector can afford without discharging is limited. Therefore, the generation of secondary avalanches decreases the charge of the primary avalanches. Secondary avalanches can be generated by both, UV photons emitted from primary avalanches, or by electrons ejected from the cathode through *photon/ion feedbacks*. The photon/ion feedbacks are mechanisms that consist on the extraction of electrons of the cathode by photons/ions which come from primary avalanches. The photon feedback effect is significant if low quenching gases are used and if the avalanche-cathode distance is short; as it is in MPGD.

The jets and bursts consist on violent electron emission from a metallic surface that has thin dielectric deposits on it. Positive ions from the avalanche are deposited in the thin films on the cathode surface generating an extremely high electric field; the so called *Malter effect*. These fields cause electrons from the metal to start to penetrate the dielectric films. After some accumulation time, an “explosive” process occurs, and the electrons are ejected from the films in the form of jets or bursts (see **Figure 2.18**). This process occurs when the ion incoming rate on the cathode is higher than the ion removing rate. Therefore, this mechanism sets a limit on the product between the gain and the incoming rate. The avalanches generated by the jets and bursts are likely to create photon feedback since this avalanches start close to the cathode.

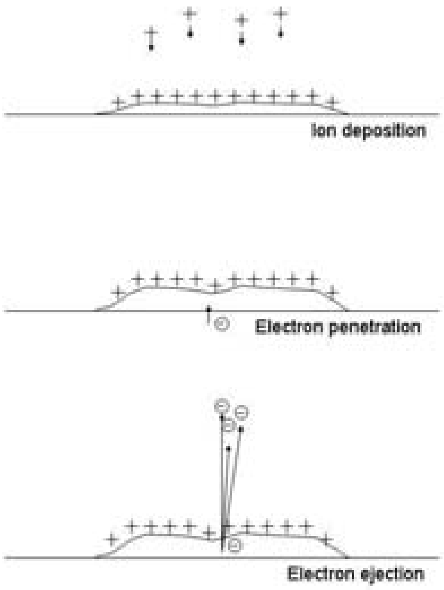

Figure 2.18 Jets/bursts generation through the Malter effect.

The rate and size of the rate induced dielectric breakdowns are reduced using resistive layers [FONTE1999a]. This solution is presented in the next subsection.

2.3.4. Resistive layer effects

The frequency and intensity of the dielectric breakdowns can be reduced applying resistive layers at the multiplication region. When a steamer appears, the induced intensities on the resistive layer generate an electric potential that decrease the electric field. As a consequence, the discharges are quenched at an early stage.

The voltage reduction depends on the charge of the avalanches, the resistivity of the layer, and the incoming rate. The intensity that a single avalanche induces does not reduce the multiplication filed significantly. Therefore, the gain of a single avalanche is only significantly affected by this effect if a very large resistivity is used. Nevertheless, the voltage reduction can be a significant drawback for high rate applications (large induced intensities) are desired. Different works of low resistivity materials have found a compromise between protectiveness and high *local count rate* (LCR) [FONTE1999a; CROTTY2003] (see **Figure 2.19**). LCR of 10^5Hz/mm^2 can be achieved with gains up to 10^5, maintaining a very low discharge rate.

A resistive layer can be also used to solve the event position using the *charge dispersion* in a resistive material grounded at their extremes [DIXIT2004].

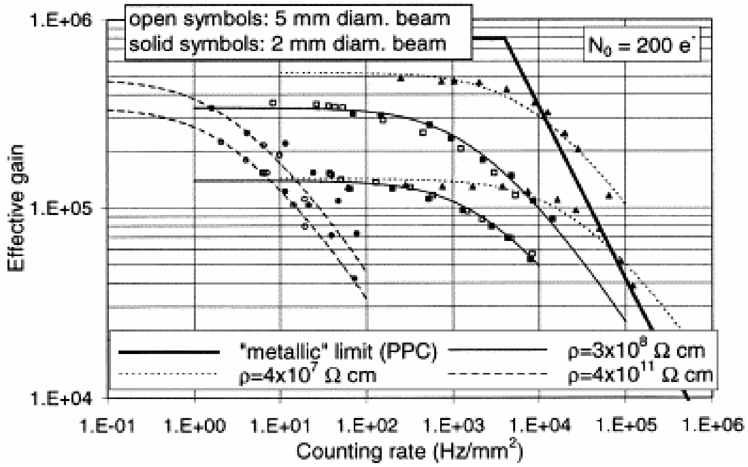

Figure 2.19 Gain-rate characteristics of a detector for several values of the anode plate resistivity and beam diameters of 2 and 5 mm [FONTE1999a].

2.4. Gas mixture

The gas mixture is very important for the detector behavior since it influences important features such as: the x-ray absorption; W; the attachment and recombination; the electron drift velocity; the longitudinal and transverse diffusion; the gain; or, the ion drift time. We briefly comment the relevance of these features.

The x-ray absorption is an important characteristic of the detector as the quality of the results depend on it. This is because the more x-rays interact with the gas; the more efficiency the detector performs and the shorter the drift distances can be. Therefore, the detector can perform a better spatial resolution (see section 4.1). Consequently, heavy gases are preferred (see **Equation 2.3**).

The value of W determines the initial number of electron-ion pairs. A low value of W implies a high number of primary electrons (N). This increases the final charge of an event, allowing the decrease of the gain through a reduction of the electric field. As we have seen, the lower the electric field is; the lower the discharges rate in the chamber is. The gas mixtures with lowest values of W are the noble gases.

High values of the recombination and attachment coefficients force the use of a high gains (high electric fields) in order to maintain the required charge to detect the event. This increases the probability of sparks. Again, gas mixtures based on noble gases are the best option due to their absence of electronic affinity. Moreover, their low energy losses for rotation and vibration decreases the value of W.

The longitudinal and transverse diffusion coefficients are ruled by the gas mixture. The electron drift velocity influences the time spread of the primary electron cloud. These characteristics of the electron transport can have important implications on the detector performance, such as the spatial resolution or the signal intensity (see subsections 4.1.4 and 4.2.3).

The gain is conditioned by the gas through the Townsend coefficient. Gas mixtures with high values of the Townsend coefficient are desired because they can perform higher gains at moderate multiplication fields reducing the rate and intensity of the dielectric breakdowns.

The ion drift time is conditioned by the ion mobility. Therefore, the election of the gas mixture conditions the local count rate (see subsection 4.2.4).

2.4.1. Quench gas

Excited atoms formed in the avalanche are de-excited giving rise to high energy photons capable of ionizing the cathode and causing further avalanches. This problem can be solved adding a little concentration of a proper polyatomic gas; the *quenching gas*. These molecules act as quenchers by absorbing the radiated photons and then dissipating this energy through dissociation or elastic collisions.

2.4.2. Aging

The aging is the deterioration of the detector after a long usage. It is a very complex physical and chemical process that decreases the gain and promotes sparks [VRA2003]. The classical explanation of the aging starts at the avalanches, where free radicals are generated. These free radicals are chemically active and form new cross-linked molecules until they become large enough so that the condensation occurs. Once the dielectric material is deposited on the electrode surface, it distorts the electric field until the point that the streamer becomes a spark. Recent studies show that the Malter effect is the most important mechanism generating discharges [HOHLMANN2002].

It is accepted that the most aging-resistant mixtures are Ar or Xe, plus CO_2. Stable operation up to ~1C/cm^2 and ~5C/cm^2 has been reported for Ar/CO_2 and Xe/CO_2, in that order [ALTUNBAS2003; KANE2003; BONDARENKO1991]. Recent works have shown that the presence of CO_2 can revert or cure Malter breakdown in the presence of high current density [BOYALSKI2003]. Therefore, the use of CO_2 as quencher gas is found to be the most appropriate at high rate applications because it is the most aging-resistant. Nevertheless, some organic gases have a better quenching power.

On the other hand, gradual decomposition of CO_2 can also occur and the resulting pure carbon can be deposited on the cathodes. Moreover, the Ar/CO_2 mixture has a lower photon interaction coefficient than many gas mixtures. It implies that the avalanche fluorescence photons can reach easily the electrodes surface promoting photon feedbacks. This effect is enhanced with the short distances existing in MPGD.

2.5. The signal

The pulse signal on the electrodes of ionization devices is formed by induction due to the movement of charged particles towards the cathode and anode, rather than the charge collection in those electrodes.

The Shockley-Ramo theorem, used to compute the induced signals, is introduced in the first subsection. In subsection 2.5.2 the origin of the intrinsic detector noise is studied. The crosstalk, a common source of noise if narrow electrodes and fast signals are used, is introduced in the last subsection.

2.5.1. Shockley-Ramo theorem

A complete derivation of the induced signals in a parallel chamber [KNOLL2000] and in a cylindrical proportional counter [LEO1994] can be found in the literature. For more complex structures, the *Shockley-Ramo theorem* [SHOCKLEY1938; RAMO1929] is used, as it gives a solution to compute the induced signal on a given electrode by a given charge in a given detector. The theorem states that the *instantaneous current induced on the electrode* (i) is

$$i = q \cdot \vec{u} \cdot \vec{E}_w \qquad (2.\ 25)$$

where q is the *moving charge*, $\vec{u}$ its velocity, and $\vec{E}_w$ the *weighting field*. It follows that the *total induced charge on the electrode* (Q) is

$$Q = q \cdot \Delta\varphi_w \qquad (2.\ 26)$$

where $\Delta\varphi_w$ is the weighting potential difference between the beginning and the end of the charge path. The weighting potential can be computed solving the Laplace equation setting the voltage of the electrode under study equal to unity and the other electrodes to zero.

Resistive layer corrections

The design of the detection structure proposed in this thesis includes a resistive layer. The signal induction calculation must be modified taking into account the resistive material effects. C. Lippmann and W. Riegler have published detailed simulation works in *resistive plate chambers* (RPC) [RIEGLER2002; RIEGLER2003; LIPPMANN2003; LIPPMANN2004a; RIEGLER2004a; LIPPMANN2004b; RIEGLER2004b]. The RPC consists of two, or more, parallel metallic plates separated by a gas and a resistive layer (see **Figure 2.20**). When a particle crosses the RPC leaving part of its energy as ion-electron pairs, they are attracted to the electrodes which detect the signal. The resistive layer protects the detector.

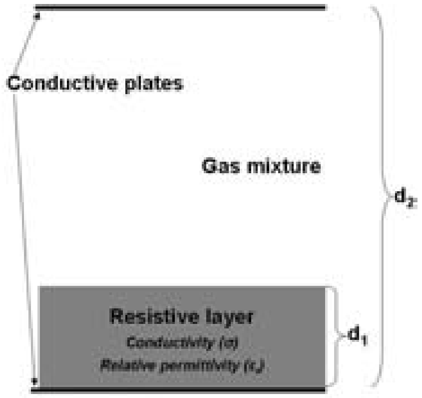

Figure 2.20 Scheme of a RPC.

The Shockley-Ramo theorem must be modified for resistive electrodes. A moving charge (q) with velocity (u) in a *resistive plate chamber* (RPC) with resistive layer thickness (d_1), resistive layer conductivity (σ), relative permittivity (ε_r) and a separation between planes (d_2) (see **Figure 2.20**) induces a current

$$i = \frac{q \cdot |\vec{u}| \cdot \varepsilon_r}{d_1 + \varepsilon_r \cdot d_2} \cdot \left[1 + \frac{d_1}{d_2 \cdot \varepsilon_r} \left(1 - e^{-t/\tau} \right) \right] \tag{2. 27}$$

where

$$\tau = \frac{\varepsilon_0}{\sigma} \cdot \left(\frac{d_1 + d_2 \cdot \varepsilon_r}{d_2} \right) \tag{2. 28}$$

The resistive layer introduces a time delay/dispersion on the signal with decay constant τ. After a long time, but before the avalanche has reached the anode, i is the same that for a parallel chamber without resistive layers.

$$\underset{t \to \infty}{i} = \frac{q \cdot |\vec{u}| \cdot \varepsilon_r}{d_1 + \varepsilon_r \cdot d_2} \cdot \left[1 + \frac{d_1}{d_2 \cdot \varepsilon_r} \right] = \ldots = q \cdot |\vec{u}| \cdot \frac{1}{d_2} = q \cdot |\vec{u}| \cdot \vec{E}_w \tag{2. 29}$$

2.5.2. Equivalent Noise Charge

The signal noise can be an important parameter regarding on the detector spatial resolution (see section 4.1). It is typically expressed as the noise standard deviation; the so called *equivalent noise charge* (ENC) [RADEKA1988].

The origins of the noise are both, the fluctuations of the *leakage current* (I_{det}), and the movement of charge carriers due to the *temperature* (T). The ENC is found to be proportional to

$$ENC = A_1 \cdot T \cdot C_d^2 + A_2 \cdot I_{\mathrm{det}} \tag{2. 30}$$

where A_1 and A_2 are constants and C_d is the *detector capacitance*. The temperature produces random fluctuations on the electrons movement. These intensity fluctuations have a Poisson distribution on time. Nevertheless, it is the detector capacitance what transforms these perturbations into noise (see **Figure 2.21**). The detector capacitance and the leakage current have to be reduced in order to optimize the ENC [RADEKA1988; GERONIMO2001].

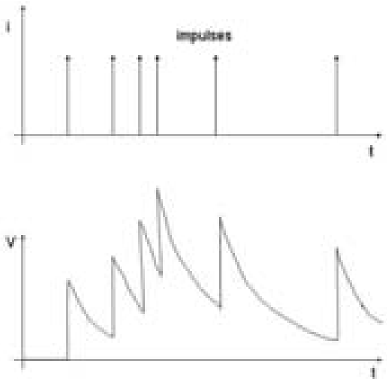

Figure 2.21 Noise formation. In the upper graph, the impulses distribution is represented. In the lower graph, the *output voltage* (V) is plotted.

2.5.3. Crosstalk

In section 3.1 the detector proposed in this thesis is described. It will be seen that the cathode is formed by narrow strips. The position is solved through the signal of these strips.

When a signal is transmitted through one strip, another signal is induced at the neighboring strips. This effect is called *crosstalk* and it is generated by the capacitance between strips (see **Figure 2.22**). It is an extra contribution to the signal noise. In the case of a detector that solves the arriving position of the particle with different readout electrodes, this effect worsens the spatial resolution.

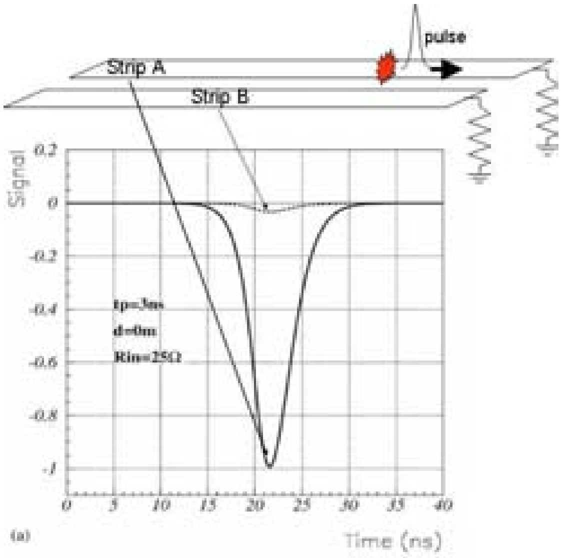

Figure 2.22 Example of crosstalk: A signal generated in strip “A” induces a signal in channel “B” [RIEGLER2002a].

The crosstalk can only be simulated if simple geometries are considered in certain cases [RIEGLER2002a]. For complex symmetries, very specialized finite element methods (FEM) programs must be used (see subsection 4.3.2).

2.6. From MWPC to MPGD

We describe in this section the different 2D photon counting proportional counters and their characteristics as well as the state of the art on this field. We start with the well established Multi Wire Proportional Counter (MWPC) and we continue with its natural evolution to detectors with short distances between electrodes: the Micro Pattern Gas Detectors (MPGD).

2.6.1. Multi Wire Proportional Counter

The MWPC is described in the literature [KNOLL2000; LEO11994] and deeply studied in a previous work of the author [FERNANDEZ2004]. The standard MWPC consists of a plane of equally spaced anode wires centered between two cathode planes also formed by wires (see **Figure 2.23**). These planes are enclosed in a box filled with a gas mixture. One side of the box consists on a thin film, the *window*, through which the particles come into the detector. The zone between the window and the wire planes is called *drift region*. The inner part of the window has a positive applied voltage with respect to the cathodes that generates the *drift field*.

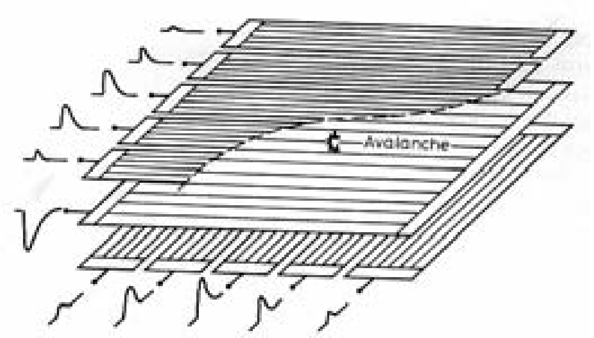

Figure 2.23 Scheme of a MWPC. The anode is the plane formed by wires placed between the other planes; the cathodes. The window is not drawn [LEWIS1994].

An x-ray that has come in the detector through the window interacts with the gas ionizing it. The primary electrons released during the interaction drift to the cathodes driven by the drift field. Close to the cathode plane, the primary electrons are attracted to the anode wires where the electric field is so high that, an avalanche takes place. The gain has a strong dependence on the anode wires radius because the close the avalanche can get to the anode wire center; the high the electric field is ($E \propto r^{-1}$). The signal is induced on the cathode wires that can solve the arriving position of the event as the wires of the two cathode planes are oriented orthogonally.

The MWPC simplicity regarding on the geometry, working principle and operation, together with its versatility, has made it one of the most used detector in many different fields from synchrotron experiments to high energy physics.

MWPC difficulties

The MWPC is not free of problems, being the construction and its weakness under discharges the most significant troubles.

In order to enhance the gain, the anode wires are very thin (~10µm) and therefore they are weak under perturbations. These perturbations are usually sparks promoted by distortions on the electric field. These distortions can be produced by aging (Malter effect, polymerization…), dielectric particles (bad cleanliness), or miss-positioning of the anode wires.

The positioning and soldering of the wires are very difficult and time consuming issues. In order to overcome bad positioning and tensioning of the wires, as well as increase the construction velocity, our group has developed an automatic method to align and solder the wires semi-automatically on their supports: the *frames* [RAMOS2003; MARTINEZ2005].

The method consists on wrap the wire around the frame, deposit the soldering material on the wires at the solder region, and finally, solder by irradiation. The wires are positioned through a large screw placed at the edge of the frame (see **Figure 2.24**). The tension is guaranteed by a hanging weight.

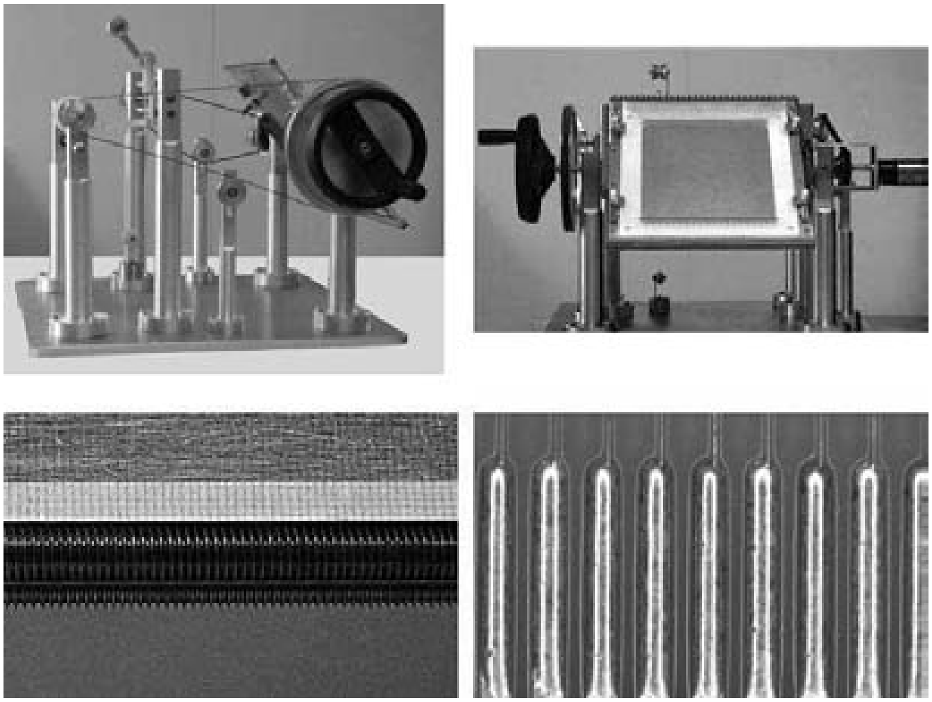

Figure 2.24 Different pictures of the semi-automatic positioning and soldering method. From left to right and up to down: 1) Lateral view of the machine 2) Front view of the machine 3) Detail of the positioning screw 4) Finished solders.

MWPC limitations

The principal limitations of the standard MWPC have their origin on the distances between wires of the same plane and also between wires of the anode-cathode planes. These distances are usually few mm.

The avalanches take place on the anode wires surfaces and therefore, the avalanches are concentrated along “lines” on the anode plane. It concludes that the anode-anode wires distance increases the space charge effects because it conditions the density of ions near the anode wires, increasing the space charge effects. The primary electrons cloud drifts to the anode wires where it is spited along lines. The anode-anode wires distance determines the splitting distance. For this reason, the anode-anode wires distance conditions the spatial resolution.

The distance between neighboring cathode wires of the same plane conditions the precision on determining where an avalanche has taken place and therefore, it also conditions the spatial resolution of the detection system.

The time the ions take to leave the avalanche region limits the local count rate. This is due to the space charge that the ions produce. This time is proportional to the distance between anode-cathode planes.

Summing up, the shorter the distances between wires are; the better the MWPC performance is. Nevertheless, major electro-mechanical problems arise for narrow gap MWPC [PETRUS2002]. Also, the instability introduced by the uncertainty in the position of the wires is higher for narrow gap MWPC.

wire MicroGap det

From the point of view of x-ray diffraction dynamic experiments, a variation of the MWPC called wire MicroGap detector performs the best detector features [LEWIS1997]. With distance between anode wires of 0.75mm and an anode-cathode distance of 0.3mm, the RAPID detector performs a local count rate higher than 10^5photons/s·mm^2 with an active area of 200x200mm^2 and a spatial resolution of ~300µm [LEWIS2000].

2.6.2. Micro Pattern Gaseous Detector

Triggered by the evolving printed circuit technology, a new generation of gaseous detectors with very small amplification cells emerged at the end of 1980s: the Micro Pattern Gas Detectors [SHEKHTMAN2002; HOCH2004; SAULI1999; SAULI2002; OED2001]. Aiming at a high position resolution and a high rate capability, their micro-structures can perform much better than classic wire chambers.

Despite their promising performance, two major problems have arisen: rare but damaging discharges and, slow but continuous deterioration (aging) during sustained irradiation. Nowadays, none of the MPGD can be used routinely for SAXS experiments in the sub-millisecond time scale.

In this section we describe the most relevant MPGD amplifying structures. Similarly to the MWPC, the complete detection system consists on: a box, a filling gas mixture, a window, a drift region and a amplifying/readout structure.

Micro Strip Gas Chamber

The *Micro Strip Gas Chamber* (MSGC) [OED1998] is a position-sensitive proportional counter mounted on a substrate, with similar operation principle that the MWPC. It consists of thin parallel metal strips alternatively connected as anodes and cathodes, deposited on an insulating support (see **Figure 2.25**). Accurate photolithography can achieve a distance between electrodes of 100µm, improving the electrodes density by an order of compared to wire chambers.

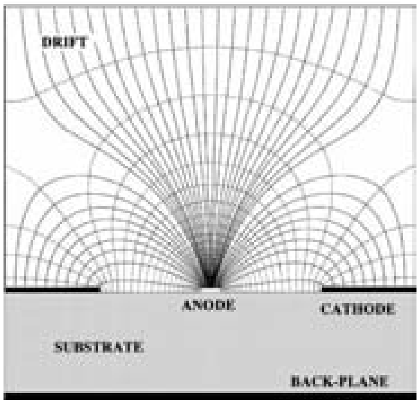

Figure 2.25 Scheme of a MSGC with equipotential and field lines [SAULI11999].

The primary electrons are attracted to the anode strips where the avalanche takes place. A signal is induced at the cathode strips. The avalanche spread is broader than the anode width and therefore, a large fraction of ions are generated at the sides of the anode strip. They drift to the cathode strips instead of drifting in the vertical direction. This effect reduces the space charge providing higher rate capability than classic devices. Local count rates of 10^5 Hz/mm^2 [BOUCLIER1995] and spatial resolutions of 30-40µm have been achieved with MSGC.

Nevertheless, this device is not free of problems. Five main operating instabilities are observed. Firstly, the tiny structure of alternating electrodes creating high-fields makes the damage due to sparks frequent. Secondly, the photon feedback is usual when operating a MSGC because the cathode electrodes are close to the anode. Fluorescence x-rays produced at the avalanche reach easily the cathode surface. Thirdly, the ion feedback is also usual. This problem arises because the ions impact zone (the cathode strips surface) is close to the anode strips and it is under a high electric field. Fourthly, the substrate charges up with ions. Finally, time-dependent gain shifts are observed. These are attributed to substrate polarization and charge accumulation.

Micro Gap gas Chamber

The possibility of patterning electrodes and also insulating layers drove to the development of the *Micro-Gap Chamber* (MGC) [ANGLELINI1993]. The MGC structure is based on a conductive backplane, used as a cathode, with anode strips placed on insulating pads (see **Figure 2.26**).

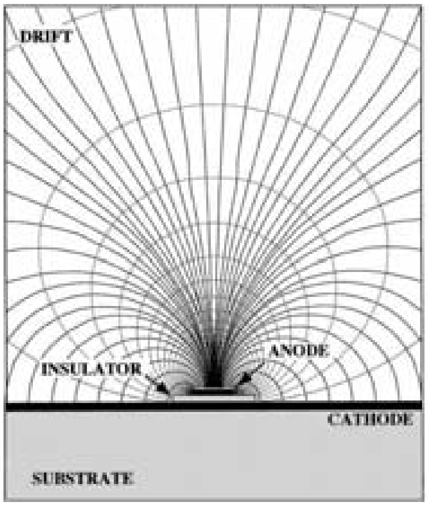

Figure 2.26 Scheme of a MGC with equipotential and field lines [SAULI11999].

The substrate, being completely covered by the cathode, is not any more charged by the positive ions; as it is in the MSGC. If a 2D readout is desired, the cathode plane is segmented into strips (perpendicularly printed to the anode strips). Depending on the dielectric constant of the substrate, the cathode-cathode and cathode-ground capacitances can produce important electric noise and/or crosstalk.

Compared to the MSGD, the electric fields between the anode and the cathode can be higher due to the presence of the insulator pads. Therefore, the gains obtained ($>10^4$) exceed those of the MSGC. Nevertheless, the MGC geometry causes the ion charging up of the insulator placed between the anodes and cathodes, ending up in continuous discharges.

Another disadvantage of this detector, compared to the MSGC, is that the printed anodes are flat but not thin. It produces a big variation on the electric field between the edges of the anode strips and the middle inducing big gain variations.

Micro-Gap Wire Chamber

In order to solve the gain variation present in the MGC, the *Micro-Gap Wire Chamber* (MGWC) was proposed [CHRISTOPHEL1997]. Its layout is similar to the MGC but the anode strips are substituted by wires with a diameter of 5µm or 10µm. They held at a distance of 15µm above the cathode plane (see **Figure 2.27**). Experimental tests have not shown a improvement of the detector behavior if anode wires are used instead of anode strips [SAULI2002].

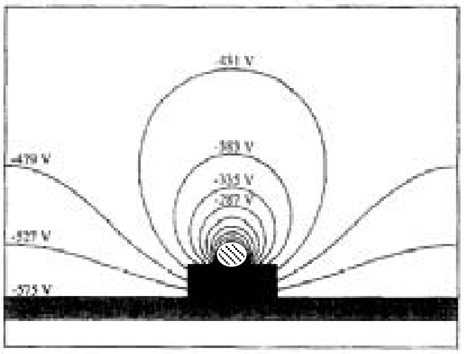

Figure 2.27 Scheme of a MGWC with equipotential and field lines. The circle filled with lines is the section of an anode wire [CHRISTOPHEL1997].

Micro Dot gas Chamber

Manufactured with metal-oxide semiconductor technology, the *Micro Dot Gas Chamber* (MDGC) [BIAGI1995] consists of a dense pattern of individual proportional counters made up of anode dots surrounded by annular cathodes (see **Figure 2.28**). For convenience of readout, the dots can be interconnected by a metal layer buried under the oxide. Field defining rings reduce the field distortion induced by the interconnections and prevent the onset of discharges. The MDGC is ideal for applications that require the detection of *multihits* (simultaneous events on the amplifying structure) because it has a pixel structure with a fast response.

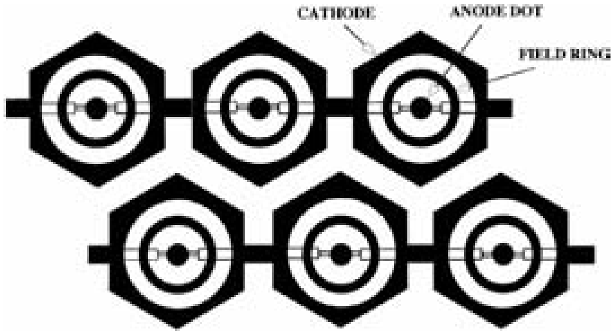

Figure 2.28 Scheme of a MDGC (top view) [SAULI1999].

Micromegas

The *MICRO MEsh GAseous Structure* (MICROMEGAS) [GIOMATARIS1996] consists of a thin metal mesh, stretched above an anode readout electrode (at a distance of 50-100µm). Regularly spaced (~1mm separation) supports consisting of insulating pillars guarantee the uniformity of the gap. A high electric field ($3\text{-}5\cdot10^5$ V/cm) is applied across the multiplying gap, where the primary electrons are collected and multiplied (see **Figure 2.29**).

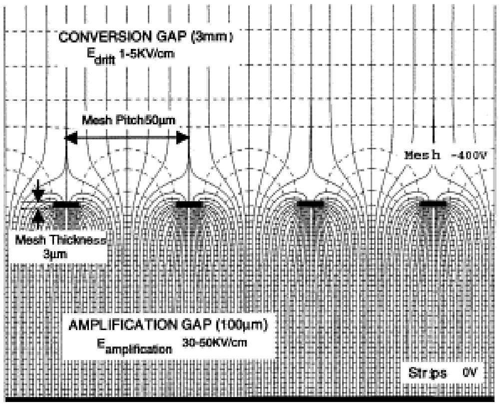

Figure 2.29 Lateral view of a MICROMEGAS [BAROUCH11999]. The electric equipotent lines (dashed) and the electric field lines can be seen. The mesh (in the middle) separates the drift region (above the mesh) and the multiplication region (below the mesh).

The MICROMEGAS exploits the saturating characteristics of the Townsend coefficient at a very high field to reduce the dependence of gain on the gap variations, thus improving the uniformity and stability of response over a large area. Thanks to the small gap and high field, the positive ions released on the avalanches move very quickly. This induces very fast signals with very small ion tail. Besides, most of the ions are collected to the top surface of the mesh preventing ion feedback.

The use of the pillars introduces two main drawbacks. Firstly, due to the electric field, the mesh tends to blend to the anode plane. At these regions the amplification gap is shorter and the electric field is higher. It implies that the gain is not perfectly uniform along the detector surface. Secondly, the pillars radius is larger than the mesh cell size, what generates areas where the particles are not detected (see **Figure 2.30).**

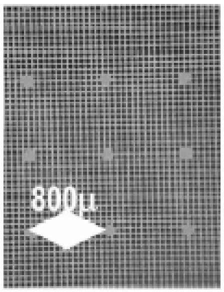

Figure 2.30 MICROMEGAS mesh (view from above) [HOCH2004].

The MICROMEGAS has been used in many experiments during the last decade and its structure is also used as a preamplification stage for other devices [ANDRIAMONJE2004].

Compteur à Trous and Well detectors

We have seen that it is difficult to obtain a uniform gain over the whole detector area if a parallel-plate structure is used. This is because the strong dependence of the gain on the gap thickness and the electric field. The *Compteur à Trous* (CAT) was introduced to solve this problem. It consists on a “metal-dielectric-metal” sandwich drilled with holes. The dielectric material guarantees the gain uniformity. The CAT concentrates the field lines converging from the drift volume into a region of high field, where charge multiplication occurs (see **Figure 2.31**).

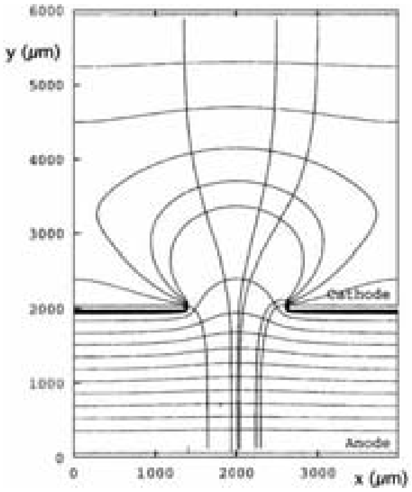

Figure 2.31 View of the section of a CAT hole with electric field and potential lines [SAULI1999].

Renamed as *WELL detector* [BELLAZZINI1999], a group from Pisa introduced the idea of manufacturing the CAT detector with anode pads instead of an anode plane making the 2D readout easier (see **Figure 2.33**).

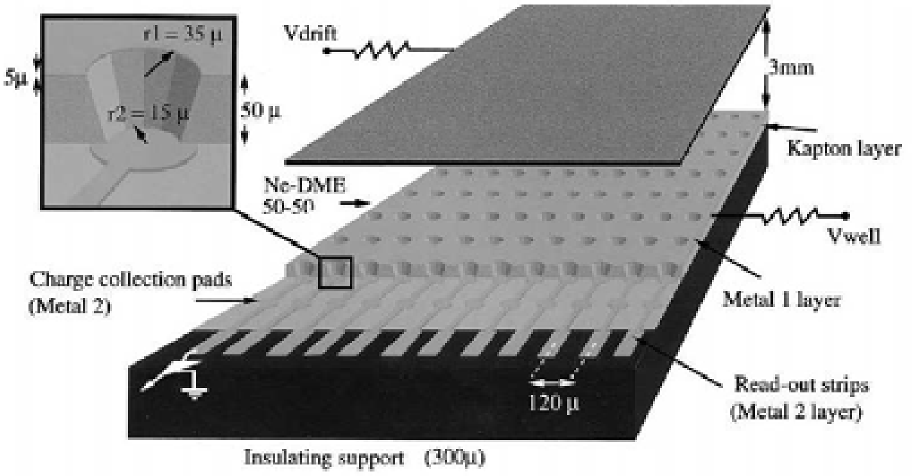

Figure 2.32 The WELL detector [BELLAZZINI1999].

This device is not free of problems. The dielectric material of the holes is usually removed through standard *Printed Circuit Board* (PCB) techniques. Therefore, the walls of the holes are not vertical, being the hole radius smaller at the lower part. The ions generated at the hole are sometimes attached to the walls. This process ends up in discharges. The hole radius have been optimized [PITTS2000] and a laser have been used to drill the holes more [PITTS1999].

This detector has been used successfully for time-resolved x-ray experiments [SARVESTANI1999; SARVESTANI2001].

Micro-CAT with redundant electrodes

High rate x-ray detection introduces the problem of multihits when 2D position determination is demanded. The *Micro-CAT with redundant electrodes* (CATER) [BERG2000a] detector was designed to solve simultaneous events. It consists of a conventional CAT detector with three readout electrodes having different angle between them (see **Figure 2.33**).

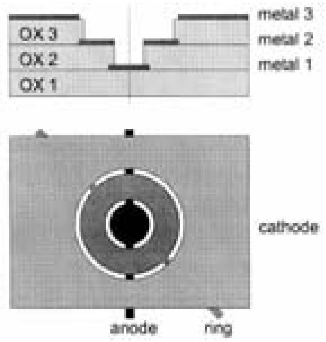

Figure 2.33 CATER detector. View of the section of a hole (up) and view of a hole from above (down) [BERG2000a].

Gas Electron Multiplier

The *Gas Electron Multiplier* (GEM) [SAULI1997] consists on a dielectric foil (usually Kapton) metalized on both sides and perforated by a matrix of holes (holes radii~70µm and separation between holes ~140µm). Applying a voltage between the two conductive plates, a strong electric field is generated inside the holes (see **Figure 2.34**). A readout plane is placed below the GEM amplification structure (see **Figure 2.35**). Primary electrons released on the drift region drifts into the holes, where they are multiplied. A signal is induced on the readout plane. The region between the amplification structure and the readout plane is called, *transfer gap*.

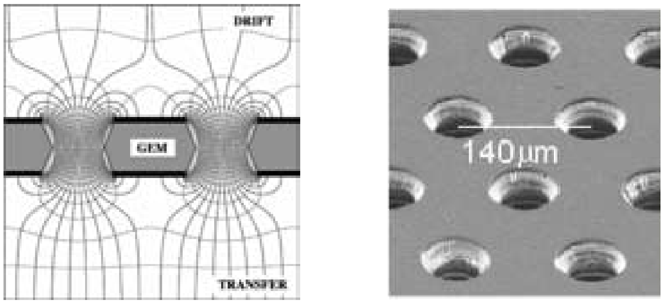

Figure 2.34 Section of a GEM amplification structure with electric field and potential lines (left) [SAULI1999]. Picture of a GEM amplification structure (right) [HOCH2004].

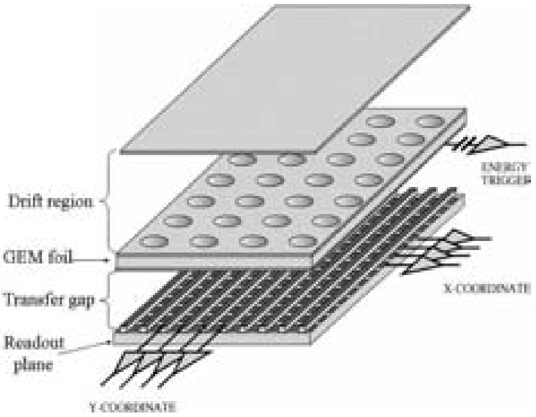

Figure 2.35 View of a whole GEM detection system.

GEM foils can be multi-staged allowing a distribution of the amplification over several foils and achieving safe detector operation (see **Figure 2.36**). Under this configuration, the Raether limit can be exceed [PESKOV2001].

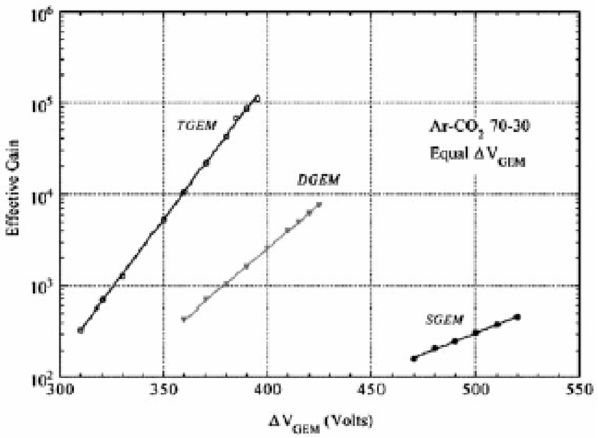

Figure 2.36 Gain as a function of the GEM applied voltage for a single, double and triple GEM. Each gain curve is plotted until the sparks limit. It can be seen how; the gain depends exponentially on the voltage. Every amplification stage can raise the gain more than one order of magnitude [HOCH2004].

The main GEM drawbacks are the aging and the charging up. Another disadvantage is the primary electron transmission from the drift region to the transfer gap. Depending on the geometry and operating voltage, the primary electron cloud can be reduced when crossing the amplification structure. In this case, the applied voltage on the plates has to be increased in order to increase the gain.

The holes geometry and disposition along the plane is studied in a simulation work in order to optimize the primary electron transmission as well as the gain [BOUIANOV2001]. An interesting variation of the GEM is the *Gas photomultiplier with GEM structure.* It consists on a GEM with a photocathode on the amplification layer, on the face opposite to the readout side. It offers single detection for UV light. However the photocathode offers a poor conversion efficiency.

Micro-Hole and Strip Plate

The *Micro-Hole and Strip Plate* (MHSP) [VELOSO2004] combines the amplification of the GEM and the MSGC. It consists on a GEM detector with a segmented backplane. At the backplane, the holes are aligned within cathode strips, while the anode strips run between them. Two electric voltages are applied, corresponding to the two amplification stages: one between the two sides of the holes (similarly to the GEM) and another between the cathode and anode strips at the backplane (similarly to the MSGC) (see **Figure 2.37**).

Gains up to $5 \cdot 10^4$ have been reached detecting 5.9keV x-rays using a 95% Ar + 5% Xe gas mixture at atmospheric pressure.

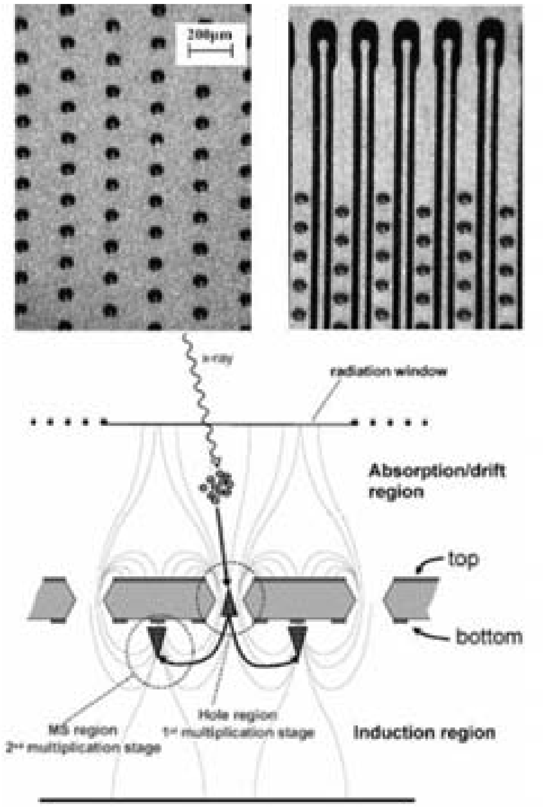

Figure 2.37 The MHSP: picture of the top plane (up-left); picture of the backplane (up-right); and, section of the detector with electric field lines and an event description (down) [VELOSO2004].

Ion Trap Micro-Strip

The electric field generated by the ions moving to the cathodes is called *ion backflow*. This electric field distorts the drift field, bending the primary electron trajectories; what worsens the spatial resolution (see **Figure 2.38**). This is a major problem when using a *Time Projection Chambers* (TPC). These detectors use the primary electron drift time to determine the third dimension of the interaction position. The ion backflow also distorts the primary electron drift time; what worsens the spatial resolution of the vertical coordinate. Moreover, primary electrons can be recombined by the backflow ions. This effect is proportional to the ion density and therefore, it is rate dependent.

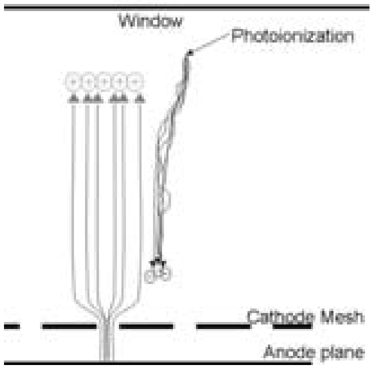

Figure 2.38 Ion backflow.

In order to reduce the ion backflow at the multiplication region, the *ion trap* technique is proposed [BOUIANOV2004]. Ion trap detectors have their electrodes implemented as non-planar structures with more than one active surface. The cathode structures are placed symmetrically with respect to the surfaces of the anode (see **Figure 2.39**). The primary electrons drift to the anode, through a random path, where the avalanche takes place. The ions leaves the avalanche region drifting to the cathodes, and only a small fraction of them escape the avalanche region moving to the drift region. The *Ion Trap Micro-Strip* (ITMS) was the first MPGD that used the ion trap concept.

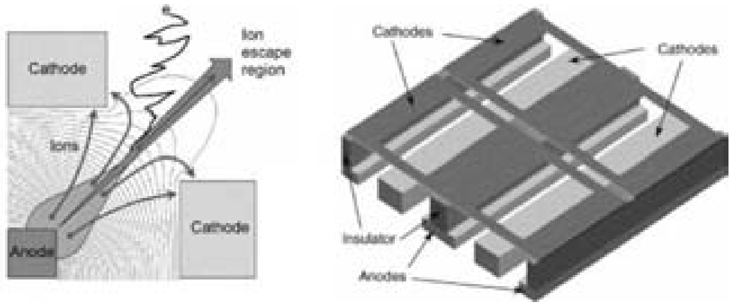

Figure 2.39 The ITMS [BOUIANOV2004].

The *inclined MicroChannel Plate* (IMCP) has attempted to reduce the ion backflow (see **Figure 2.38**) at the drift region. It consists on a plane with a series of inclined tunnels in the presence of a magnetic field. The inclination is such that it coincides with the electrons Lorentz angle but not with the ions one (see **Figure 2.40**). In this way the electrons can drift through it but the ions get attached. This device has been tested with a MICROMEGAS amplification structure [VRA2005].

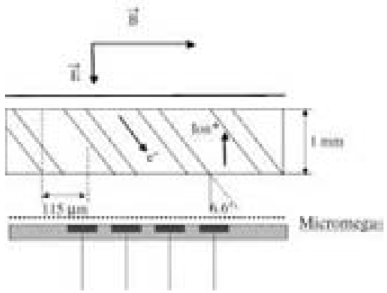

Figure 2.40 Inclined MCP+MICROMEGAS [VRA2005].

3.The new detector

This chapter contains the description of the MRMC. We describe first the proposed detection structure, its working principle and the advantages of its design with respect to its competitors.

The second section is dedicated to the detector construction process describing the techniques used for the building up of the different parts of the detector, as well as the layout of the prototype. The manufacture limitations have been pointed out because they introduce constrains on the optimization process.

In the third section the readout electronic system is presented. The delay line readout system is first described. After that, the different devices involved in the readout are studied; including simulations and experimental tests. Finally, two future improvements of the readout system are described: an upgrade of the delay line based readout system and a parallel readout system.

3.1. Overview of the MRMC

The MRMC and its principle of operation are presented in this chapter.

Our group has a grant of the Ministerio de Educación y Ciéncia (Grant No. FPA2003-05050) to develop detection systems to perform 2D time resolved experiments in the sub-millisecond time scale for small angle x-rays scattering (SAXS) experiments. This project includes the construction of a MWPC and the test of new structures for future developments. The construction of the MRMC is included in this last objective.

The main objective of the construction of this detector is the improvement of the spatial resolution, the local count rate and the discharge hardness of the present detection system. In order to enhance the spatial resolution and the local count rate, the MPGD approach has been chosen. It consists on building a high electrodes density detector with a high density of electrodes: short distance between cathodes (spatial resolution) and short anode-cathode distance (local count rate). The sparks hardness is worked out, among other characteristics, with a resistive layer on the anode surface.

The device is described in the next subsection. The parameters of the final design (see **Table 5.1**) are given after the simulation and optimization study.

3.1.1. Description of the device

The MRMC is a one amplification stage MPGD. It consists on an enclosure filled with gas. In it, two different regions are distinguished: the *drift region* and the *amplification region*. They are separated by the cathodes mesh (see **Figure 3. 1** and **Figure 3.2**); which is grounded.

In the drift region, the opposite face of the cathodes mesh is the so-called *window*. It consists on a thin layer (100μm) with a conductive layer (15μm). Applying an electric potential difference between the window (-1000V) and the cathodes mesh (0V), an electric field is generated in the drift region. It is the so-called *drift field* (~10^3V/cm).

In the multiplication region, the opposite face of the cathodes mesh is the *anode*. It consists on a conductive plane with a resistive layer. On the resistive layer, a set of small pillars separates the anode from the cathodes mesh. An electric field is generated in the multiplication region by the electric potential difference between the anode (2000V) and the cathodes mesh (0V). It is the *multiplication field* (~10^5V/cm).

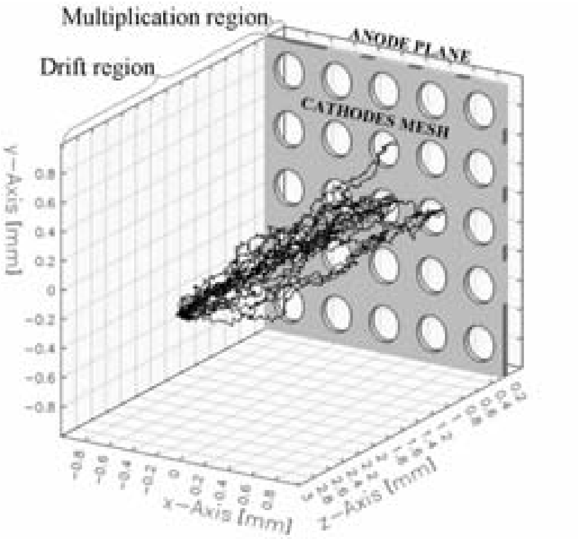

Figure 3. 1 3D view of the chamber. It can be seen the drift and multiplication regions, the cathodes mesh and the anode plane. The path of some primary electrons going from the x-ray interaction point to the anode plane can also be seen.

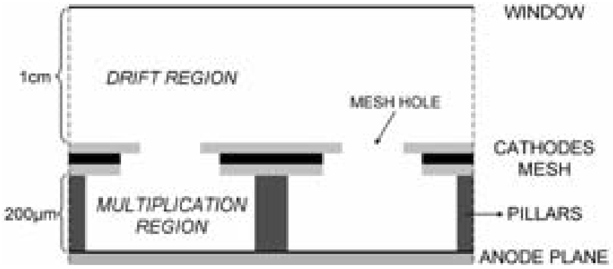

Figure 3. 2 Lateral view of the different parts of the MRMC (not in scale). The cathodes mesh is formed by two layers of cathode strips (light grey) separated by a kapton layer (black). The anode plane has a layer of resistive material on it**.**

The cathodes mesh consists on two conductive layers formed by Cu strips. The two planes are separated by a dielectric layer. The cathode strips of the plane which is facing the drift region are called: *upper cathode strips* (see **Figure 3. 3**). The upper cathode strips have holes on their center along the strip. The cathode strips of the face which is facing the multiplication region are the *lower cathode strips* (see **Figure 3. 4**). They have a particular shape which forms holes at their edge. These holes have a larger radius compared to the upper cathode strips holes, and are aligned to the upper cathode strips holes.

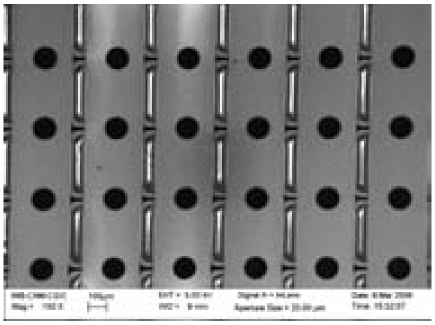

Figure 3. 3 View of the cathode mesh from the drift region. The upper cathode strips and their holes are observed. The kapton material and the lower cathode strips can be observed between strips

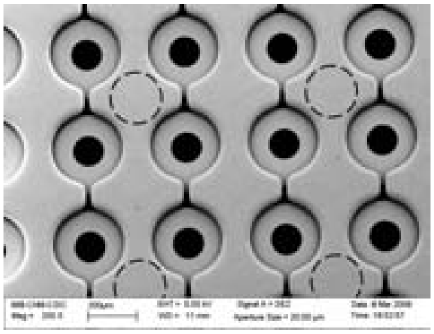

Figure 3. 4 View of the cathodes mesh from the multiplication region. The lower cathode strips and their holes are observed. The upper cathode strips can be observed between strips. The dashed circles mark the positions of the pillars; that separates the mesh from the anode.

3.1.2. Principle of operation

An x-ray that enters into the chamber through the window can interact with the gas through the photoelectric effect. If so, few hundreds of primary electrons are released in the drift region. The drift field drives the electron cloud first to the cathodes mesh (see **Figure 3. 1**), and then into the multiplication region. There, the electric field is very intense and therefore, the avalanche takes place. A signal is induced on the anode and on the neighboring upper and lower cathode strips. Using the anode signal as a trigger, the position of the event is solved with the signals of the upper (X) and lower (Y) cathode strips. Finally, the ions released during the avalanche, leave the multiplication zone through the holes and to the window.

3.1.3. Advantages

Experience with MPGD has raised two major problems [SHEKHTMAN2002]: damaging discharges and, aging during continuous irradiation. Also counting non-uniformity has been seen in many MPGD. It is usually due to a non-homogeneous gain over the whole area of the detector. In this subsection the advantages of the MRMC design are reported.

Pick up the signal at the mesh

In order to decrease the probability of dielectric breakdown, the anode applied voltage must be reduced. This can be done, without decreasing the efficiency of the detector, increasing the signal sensitivity of the cathodes.

In other MPGD designs the cathode strips are placed on a readout plane below the anode [BRESSAN1999b]. The MRMC cathode strips are placed at the mesh. Consequently, the signal sensitivity of the MRMC pick up strips is higher, compared to conventional MPGD. This design allows a decrease on the multiplication field without loosing detection efficiency. This reduces the probability of arising of sparks; either voltage-induced or rate-induced.

Resistive anode

Studies of Resistive Plate Chambers (RPC) have shown that highly resistive electrodes quench the discharges at an early stage. In these designs, the sparks affect the detector only locally, without damaging the readout electronics. This technology is already been used in some MPGD showing local count rates above 10^5Hz/mm^2 with gains of 10^5 [IVANIOUCHENKOV1998]; [FONTE1999].

A resistive layer is attached on the anode plane of the MRMC. It reduces the formation of sparks and diminishes the damage they could make to the detector. Its resistivity and thickness have been optimized to allow local count rates $>10^5$Hz/mm^2.

Thick strips

It has been seen experimentally that the damaging effects of discharges can be irreversible if thin strips are used [BRESSAN1999a].

Thick cathode strips (25μm) are set in the MRMC design enhancing the detector strength under discharges and preventing the mesh to be bent. This helps the multiplication distance to be constant over the detection area; improving the gain uniformity.

Number of pillars

The multiplication distance is set by the pillars height. Depending on the distance between pillars, the multiplication distance can vary along the active area.

In order to guarantee that the multiplication distance is the same for every hole, the pillars are set with a period of two cell sizes, in the middle point between four holes (see **Figure 3. 4**). Consequently, the gain uniformity over the whole area of detection is improved.

Mesh geometry

Close to the amplification zone, the presence of dielectric material leads to gain instabilities due to the charging up [SHEKHTMAN2002]. To avoid this effect, a minimum dielectric material has to be used in the detector [KANE2003]; especially near the avalanche zone. The radii and thicknesses of the cathodes and dielectric material of the mesh have been chosen in order to reduce the charging up. Firstly, these parameters have been chosen to optimize the collimation of the avalanche ions when crossing the mesh. Secondly, the dielectric material near the avalanche region is removed during the etching (see **Figure 3. 15** in subsection 3.2.2).

In addition, the MRMC parameters have been optimized to avoid the avalanche ions to end their paths on a cathode surface which is facing the avalanche region. This solution aims to diminish the ion feedback.

Gas mixture

A xenon based mixture is used; $0.9 \cdot Xe + 0.1 \cdot CO_2$. It has been demonstrated that the choice of this gas reduces the aging (see subsection 2.4.2). The xenon is used instead of argon as a noble gas since the x-rays in xenon have a higher photoelectric cross section. Moreover, the photoelectron range is shorter, what enhances the spatial resolution (see subsection 4.1.2).

3.2. Building up processes

In this section the construction processes of the different parts, as well as the prototype layout, are described. The most critical part to build is the cathodes mesh. Its complicated shape and the requirements for the dielectric disposition and the smoothness of the edges make its construction difficult. The manufacture of the pillars structure and its alignment to the cathode structure are also challenging.

For the construction of the detector, two different options where considered: the Centro Nacional de Microelectrónica (CNM), or the PCB workshop at Centre Européen pour la Recherche Nucléaire (CERN). Both have advantages and drawbacks.

The CNM is placed near the synchrotron site allowing a good control on the construction processes. The technique that would be used to build the cathodes mesh is based in microelectronics lithography processes that have a very good precision. However, this technique does not allow the construction of the structures in large areas ($>5x5cm^2$) and presents lots of difficulties in constructing thick structures (>100μm). In other words, it is a good technique to construct small structures with a high precision but with difficulties to build large structures. Besides, they do not have experience in constructing similar detectors, or even similar structures.

The CERN PCB workshop is placed near Genéve. This makes difficult to control the construction. Nevertheless, the construction of the detector at CERN has several advantages. Firstly, the technique that would be used to build the cathodes mesh is the ChemicalVia [CERN2002], a new method to make microvias in high interconnect PCBs. This technique has demonstrated to have a good precision (<1-10μm) with a large variety of materials. Secondly, they have a very large experience in constructing MPGD with similar structures [SAULI1997; BELLAZZINI1999; BELLAZZINI12000; LABBE1999]. They develop and test their own MPGDs [DICK2004]. Thirdly, the structure can be built in large areas ($10x10cm^2$) and they are planning to construct structures with areas of $20x20cm^2$. Fourthly, not only the cathodes mesh structure would be constructed there, but the whole detector. Finally, its price is much lower, compared to the construction at the CNM.

It was decided to build the detector at the PCB workshop at CERN.

Prototype layout

The prototype layout is shown here determining the different structures that have to be built. The parameters of the final design (see **Table 5.1**) are given after the simulation and optimization study.

This layout is based in four different layers.

The first layer is the “support + anode + resistive layer + pillars”; that is called *anode layer*. It consists on a ceramic layer with a Cu anode plane and a resistive layer that have the pillars on it. The ceramic layer has a little hole to apply the anode voltage to the anode plane. The pillars structure consists on the pillars, that cover the active area, and a frame that surrounds it (see **Figure 3. 5**). It has four holes at the corners that are used for alignment purposes.

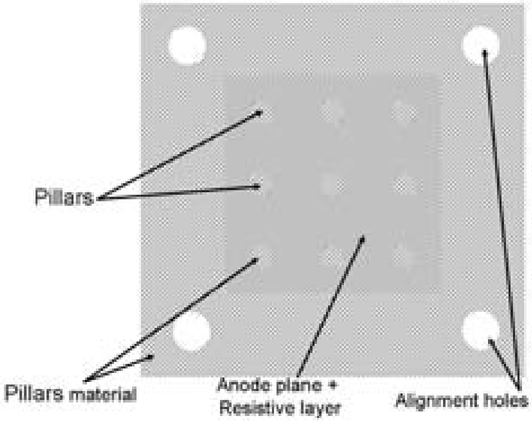

Figure 3. 5 Top view of the anode layer. The four white circles in white represent the alignment holes. The zones represented in grey lines represent the pillars material. The zone in grey represents the resistive layer; which is placed between the anode and the pillars.

The second structure is the cathodes mesh layer. It consists on two cupper foils separated by a dielectric layer (see **Figure 3. 6**). The cupper layer that is facing the drift region (the upper cathode) has the upper cathode strips pattern. This includes the strips (ending at one edge) and the mesh holes. The cupper layer which is facing the multiplication region (the lower cathode) has the lower cathode strips pattern. This includes the strips (ending at one edge) and the mesh holes that have a smaller radius compared to the upper cathode pattern. The dielectric layer has the mesh holes with the same radius as the lower cathode holes. Both cathode foils and the dielectric layer have four holes at the corners that are used for alignment purposes.

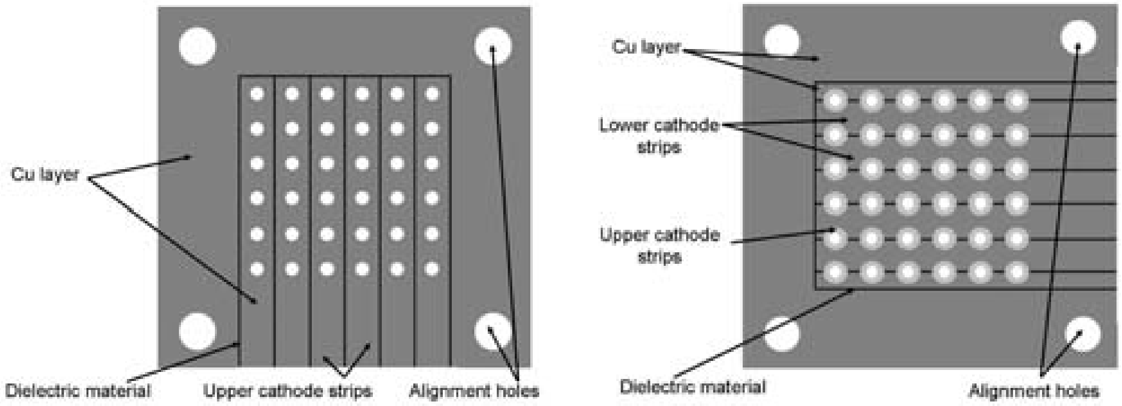

Figure 3. 6 View from the drift region (left) and from the multiplication region (right) of the cathodes mesh structure. The four large white circles in white represent the alignment holes. The small circles in white represent the cathode strips holes. The black lines are dielectric material; which can be seen between cathode strips. In the

right figure, the zones in light grey represent the parts of the upper cathode strips that can be seen from the multiplication region.

Placing the cathodes mesh layer on the anode layer, the multiplication region is defined. This can only be accessed through the holes because the lower cupper layer is laying on the pillars material frame outside the active zone (see **Figure 3. 7**).

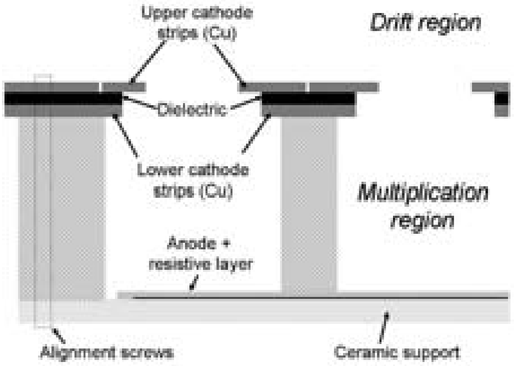

Figure 3. 7 Lateral view at the edge of the anode layer + the cathodes mesh. The view is not in scale. The vertical cut of the two first holes at one edge of the active area can be seen, as well as the alignment screw of that corner.

The third layer is the drift frame. It consists on a square frame with four vertical alignment holes at the corners. It also has a gas valve at one side, to connect the inner part of the detector with the gas bottle. The height of the frame is equal to the drift distance and the inner area is equal to the active zone (see **Figure 3. 8**).

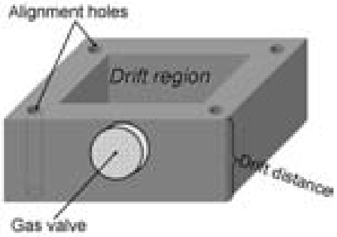

Figure 3. 8 Drift frame.

The fourth layer is the window. It consists on a thin kapton foil (100μm) with a thin aluminum pattern on it (15μm). The Al pattern has a square shape and it covers the active area. It has one connection to the edge of the window layer (see **Figure 3. 9**).

In **Figure 3. 10** the prototype design layout is shown. The drift frame, the cathodes mesh and the window confine the drift region.

This prototype design has two main objectives. The first one is to have a high degree of flexibility that allows the replace of the different parts. The second objective is to have access to all the connections. Depending on the test, the cathode strips can be all grounded, some of them connected to a preamplifier or connected to a delay line. Besides, the absence of a box makes the layout cheap.

This prototype design has two main drawbacks related to the absence of a metallic box. The first one is that the prototype is not sealed. It implies that, in order to maintain the required cleanliness, the gas must be in continuous flow; going in through the valve, and going out thorough the small holes between cathode strips and the possible leaks. The second drawback is the electromagnetic shielding. The absence of a close grounded box allows the electromagnetic noise to enter into the box increasing the noise.

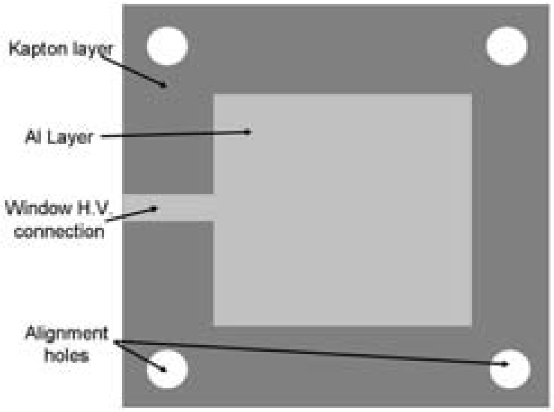

Figure 3. 9 Window layer.

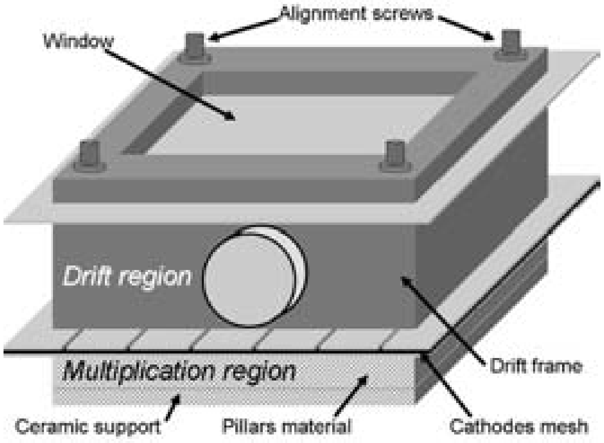

Figure 3. 10 Prototype layout.

3.2.1. Anode layer

In this subsection the building process of the anode layer is described. The procedure starts with a ceramic support layer that has a small hole. This is used for the anode connection. First, a copper layer with area equal to the active area is deposited on the ceramic support (see **Figure 3. 11 (a)**). It is the anode. Then, the anode is painted with a resistive material and it is dried in the oven (see **Figure 3. 11 (b)**). The resistivity and thickness is controlled very precisely. Once the resistive material is fixed, the pillars material is deposited on the structure, covering the whole area of the ceramic support (see **Figure 3. 11 (c)**). The height of this layer is the multiplication distance. The pillars material is then irradiated, covering the pillars pattern (pillars + and surrounding frame) (see **Figure 3. 11 (d)**). This process changes the chemical structure of the pillars material in the desired zones. Finally, the structure is attacked with a chemical product that removes the not-irradiated pillars material (see **Figure 3. 11 (e)**).

This process has one limitation related to the pillars height. The depth that the irradiation can penetrate into the pillars material is limited. Therefore, when irradiating the pillars material, the lower parts are not irradiated. Consequently, these zones are chemically attacked (see **Figure 3. 12**). The building capabilities allow a maximum pillars height of 200µm for the MRMC. It assumes a little error at the lower part which is not critical if the radius is 125µm.

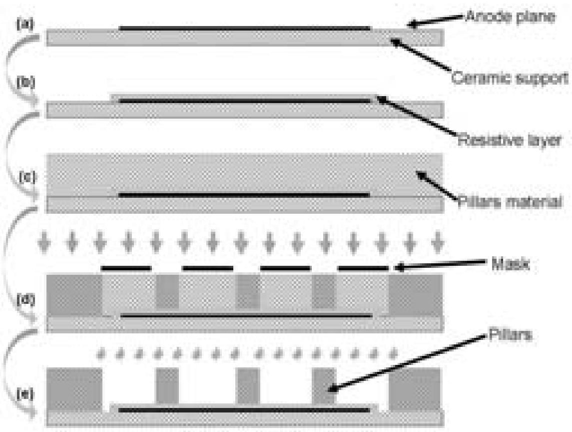

Figure 3. 11 Building process of the anode layer.

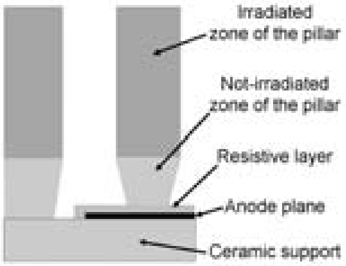

Figure 3. 12 Pillars slope error at their lower part.

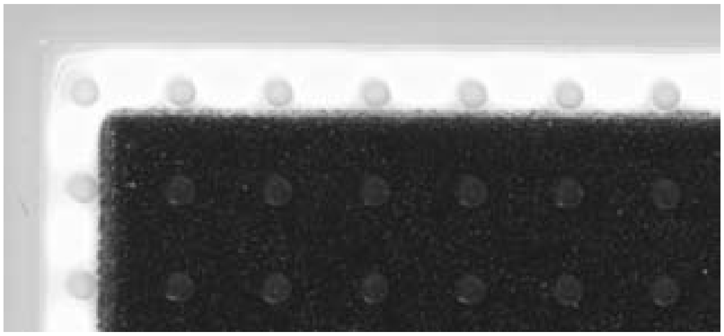

Figure 3. 13 Picture of the corner of the anode layer. The pillars material (pillars + surrounding frame) is quasi-transparent (light grey) and therefore, the pillars on the resistive material (black) seem darker. The ceramic support (white) can be seen between the active zone (black) and the surrounding frame (light grey). The resistive painting is slightly transparent and therefore, the anode Cu foil can be distinguished below the resistive painting, at the edges.

3.2.2. Cathodes mesh layer

The building process of the cathodes mesh layer is described in this subsection. The process is divided in three main steps: upper cathode patterning; lower cathode patterning; and, dielectric patterning.

The first process is sketched in **Figure 3. 14**. It is started with a dielectric (Kapton) layer with one cupper layer attacked at each side. The upper cathode layer has a photoresist film on it (**Figure 3. 14 (a)**). Then, a mask, which has the desired pattern, is placed on the photoresist film. U.V. light is applied. The photoresist film is partially irradiated, changing the chemical properties of the material (**Figure 3. 14 (b)**). The third step is to submerge the whole structure in a chemical product that attacks the irradiated zones (**Figure 3. 14 (c)**). Finally, the structure is submerged in a chemical product that attacks the cupper material that is not protected by the photoresist. The desired pattern is obtained (**Figure 3. 14 (d)**).

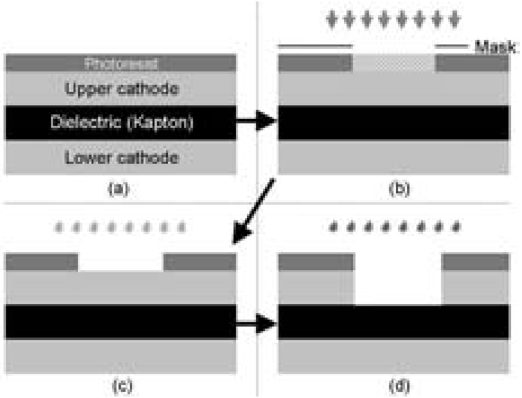

Figure 3. 14 Process of fabrication of the upper cathode patterning.

The photoresist is patterned with vertical walls because the U.V. light has arrived vertically. However, when attacking the cupper, all the material can be removed. The chemical product attacks the surface uniformly. This leads to spherical walls. In order to make the structure with vertical walls, the under-etching technique must be employed. It consists on making the mask with smaller dimensions than the desired pattern and attack the cupper controlling the exposure time (see **Figure 3. 15**).

For the thicknesses and materials of the MRMC, the under-etch is 50μm and the minimum hole radius that can be drawn in the mask is 25μm. Thus, the minimum hole radius that can be built is 75μm.

The second step to build the cathodes mesh is the patterning of the lower cathodes. It is the same as the upper cathode patterning.

The third step is the patterning of the dielectric material; which is placed between the cathode planes. The desired pattern of this layer is the same as the lower cathode plane. However, it is desired that the dielectric area is smaller than the area covered by the lower cathode in order to reduce the charging up. This process is done attacking the structure from the lower cathode face with a chemical product that only dissolves the dielectric material. Controlling the time, the amount of removed material is controlled (see **Figure 3. 16**). In **Figure 3. 17** two pictures of the prototype cathodes mesh taken with the Scanning Electron Microscope (SEM) are shown.

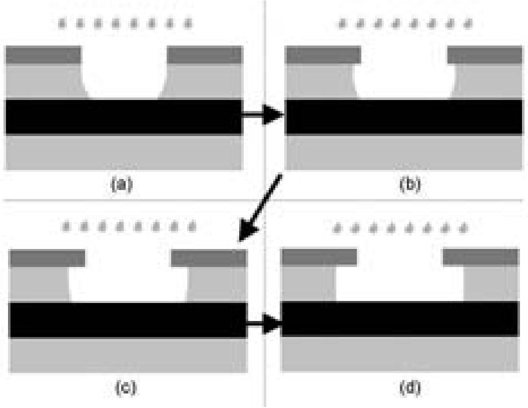

Figure 3. 15 Under-etching process. The desired hole radius is larger than the radius of the mask.

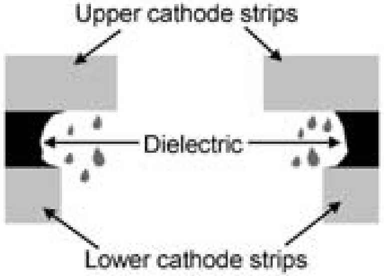

Figure 3. 16 Dielectric pattern process. It can be seen that no dielectric material remains close to the paths of the ions; which have been released during the avalanche. They go from the avalanche to the window, crossing the mesh from down to up.

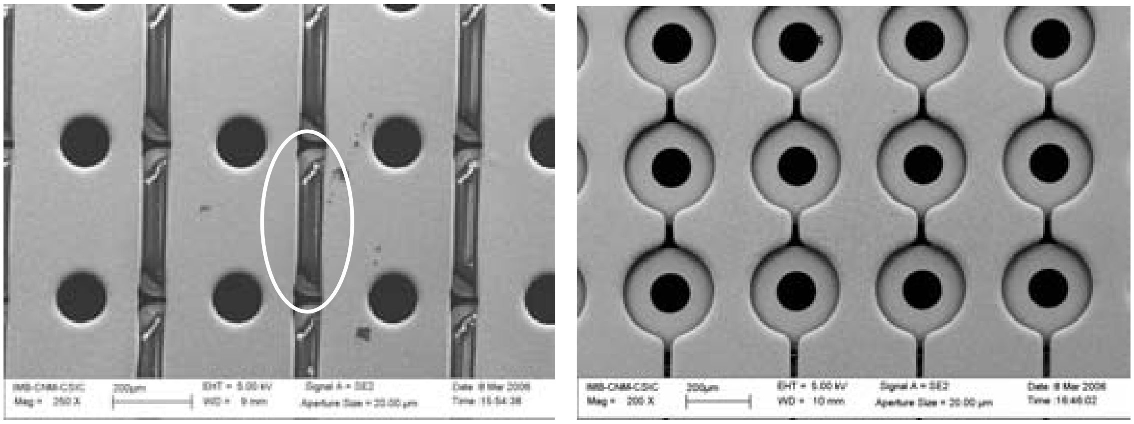

Figure 3. 17 Pictures of the prototype cathodes mesh taken with the SEM; from the drift region (left) and from the multiplication region (right). In the right image, the dielectric material is not observed. In the left image the dielectric material can be observed in the white circle. In it, it can be seen that the dielectric material covers less area than the lower cathode strips.

3.2.3. Drift frame

The drift frame is fabricated with Macor. This material is chosen because it is resistant, it can be easily machined, it is radiation hard and it does not outgas. The easily machining is needed to obtain the required flatness over the whole area and the required precision at the alignment holes.

3.2.4. Window

The window consists on a Kapton layer (100µm) with an aluminum foil (15µm); which is deposited with the desired pattern.

3.3. Readout, electronics and DAQ

The readout system is described and characterized in this section. The MRMC readout system is based on a delay line. This readout system is well known by our group since it is being used for the MWPC that is going to be installed in the SAXS station of BM16 beamline at the ESRF.

A description of the delay line based readout system is given first. Afterward, the different components and devices included in this readout system are studied. Finally, the future perspectives of the readout system are described.

3.3.1. Delay line based readout system

Delay line based readout electronics for x-ray area detectors used to carry out dynamic measurements with synchrotron radiation are used mostly due to its relative simplicity and low cost [EPSTEIN1998].

In the delay line based readout system, the cathode electrodes (wires, strips,…) of each coordinate (X,Y) are connected to a delay line (see **Figure 3. 19**). A delay line is a transfer line which delays the signals that are transmitted through it. A signal that is introduced in a given position of the delay line is transmitted to both ends of the delay line with a time delay which is proportional to the distance that the signal has traveled in the delay line.

The localization of the event starts with the capture of the anode signal. Then, the four cathode signals are received; two cathode signals coming from each delay line (X,Y). The cathode signals arrive at times that are directly proportional to the X and Y coordinates of the event (see **Figure 3. 18**). The position of the event in one coordinate is then solved from the time difference of the two pulses of the delay line of that coordinate.

The whole readout system consists on: two delay lines (one for the upper cathode and one for the lower cathode); five preamplifiers (one at each side of each delay line and another one for the anode); a Constant Fraction discriminator (CFD); a Time to Digital Converter (TDC); and, a histogramming system.

When an avalanche takes place, a signal is induced at the neighboring cathode strips (upper and lower) and at the anode plane. The cathode strips of one plane are transmitted to the delay line. There, the signal is divided and transmitted to the delay line extremes with a time delay proportional to the length traveled in the delay line. At the extreme of the delay line, a pulse is transmitted to a preamplifier, where the signal is amplified. The amplified signal is then transmitted to the CFD, which determines the arriving time of the pulse and generates a digital signal. The four digital signals of the cathodes (2 extremes of 2 delay lines) and the one of the anode are transmitted to the TDC, which determines the position of the event from the time difference between pulses. Finally, the position is stored in the histogramming card.

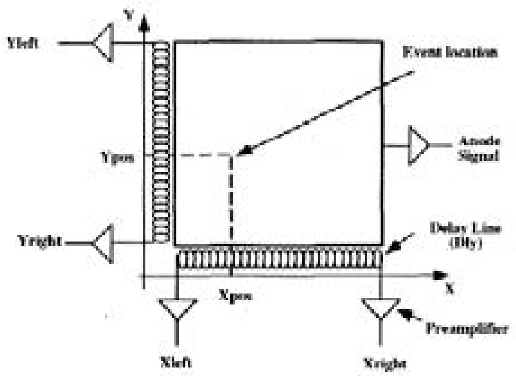

Figure 3. 18 Delay line position localization principle.

3.3.2. Discrete delay line

A delay line is a transfer line that delays in time the traveling signal. There are two types of delay lines: continuous and discrete. The discrete delay lines consist on: an array of condensers (C) and inductances (L) that connect the cathode wires between their extreme (see **Figure 3. 19**).

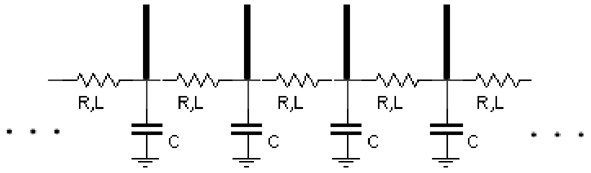

Figure 3. 19 Section of a discrete delay line. The blaze symbols represent the inductances (L); which has an associated resistance (R). The thick lines represent the cathode electrodes.

Time delay

When an event takes place, a signal is induced at a group of cathode electrodes. This charge, that is integrated in the delay line, leaves the cathode through the delay line in the two directions (see **Figure 3. 20**).

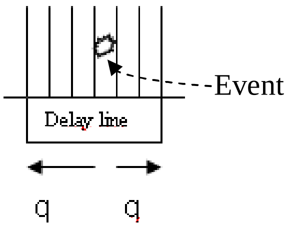

Figure 3. 20 Signal division in a delay line.

When a signal crosses one cell of the delay line (one L + one C), it is delayed a time (t_{cell})

$$t_{cell} = \sqrt{L \cdot C} \qquad (3.\ 1)$$

The total delay time (T_{total}) a pulse takes to go from one extreme of the delay line to the other is $T_{total}=N \cdot t_{cell}$; where N is the number of delay line cells. Comparing the arriving time of the pulse at both sides of the delay line, the position of the event can be solved.

Characteristic impedance

From the point of view of the transmission line, the discrete delay line has a characteristic impedance (Z_0)

$$Z_0 = \sqrt{\frac{jLw + R}{jCw + G}} \qquad (3.\ 2)$$

where R is the resistance and G the conductance. This expression can be approximated to **Equation 3.3** if the conductance is very low and R is low compared to L/C

$$Z_0 \cong \sqrt{L/C} \qquad (3.\ 3)$$

If the value of Z_0 is not similar to the preamplifier impedance (50Ω), the signal is reflected. In this case, when a pulse is arriving at one side of the delay line, part of the signal is not transmitted to the preamplifier but reflected. The reflected pulse travels along delay line in the opposite sense adding noise to the signal at the other side. This distortion can be large enough to impede the detection. Consequently, Z_0 must be similar to the input impedance of the preamplifier.

Attenuation

The pulse amplitude is reduced in the delay line due to the *delay line series resistance* (R_{tot}) (the conductance is very low) and to the low pass filter introduced by the LC circuit.

The series resistance of the delay line is the addition of the resistance of the pads connecting the inductances (R_p) and the inductances series resistance (R_L). Thus, $R_{tot}=R_p+N \cdot R_L$. Depending on the pads design, R_p is not negligible. The transmission of a signal at a frequency equal to 0Hz through a real delay line is

$$transmission\Big|_{f=0} = EXP\left(\frac{-R_{tot}}{2 \cdot Z_0}\right) \qquad (3.\ 4)$$

The delay line is also a first order low pass filter. For an imaginary delay line with $R_{tot}=0\Omega$ the *cutoff frequency* (f_c) is

$$f_c = \frac{1}{2 \cdot \pi \cdot \sqrt{L \cdot C}} \qquad (3.\ 5)$$

The cutoff frequency is used in this subsection for the calculation of the rise time (see later). The attenuation is 20dB/dec for frequencies higher than f_c.

Attenuation characterization

Our group has been working with two different designs of the pads where the components of the discrete delay lines are soldered (A and B designs). The frequency response of both designs is tested in order to choose the most adequate for the prototype. Both designs have the same components (C=22pF; L=54nH; R_L=35mΩ) of the delay line that is proposed for the MRMC prototype. Their series resistances are first studied.

Both pads design of the delay lines consist on two layers of 18μm thickness; Sn and Cu. However, the number of cells in the delay lines A and B are 98 and 198, in that order. Due to space restrictions on the PCB surface, the total tracks length (L) in delay line A and B are 278mm and 1073mm, in that order. The width of the tracks in delay line A and B, are 350μm and 200μm, in that order. The resistance of the tracks connecting the inductances is the parallel resistance of the Cu part and the Sn part.

$$R_p = \frac{R_{p,Sn} \cdot R_{p,Cu}}{R_{p,Sn} + R_{p,Cu}} = \frac{\rho_{Sn} \cdot \rho_{Cu}}{\rho_{Sn} + \rho_{Cu}} \cdot \frac{L}{S} \qquad (3.\ 6)$$

where S is the section of each layer of the pad, ρ_{Sn} is the Sn resistivity (0.12 Ω·mm^2/m) and ρ_{Cu} is the Cu resistivity (0.018 Ω·mm^2/m). For delay lines A and B, R_p is 0.70Ω and 6.54Ω. Thus, R_{tot} is 3.9Ω and 11.35Ω. From **Equation 3.4**, the attenuation in DC is 4% and 11% (-0.35dB and -1.01dB), respectively.

The series resistance of both delay lines is measured. R_{totExp}=3.9Ω and 11.2Ω. It agrees with the theoretical value. Therefore, the calculation of the track resistance is correct.

The frequency response of both delay lines is tested with a spectrum analyzer Agilent CSA N1996A [AGILENT2006] and with a network analyzer Agilent ENA E5071B [AGILENT2005]. In this test, a sinusoidal input signal of a variable frequency is introduced in one extreme of the delay line. The amplitude of the output signal at the other extreme is stored as a function of the input frequency (see **Figure 3. 21**). The frequency response in db is negative because the delay line attenuates the signal.

The theoretical values of the attenuation (-0.35dB and -1.01dB) in DC mode agrees with the measurements (see zoom window in **Figure 3. 21**). The difference between the two curves is due to the series resistance of the delay lines. Therefore, it is very important to use low resistivity inductances and proper pads design, in order to prevent the signal to be diminished by the delay line. The A design is chosen for the prototype.

Prototype delay line

The delay line that is proposed for the MRMC prototype has the same configuration as the MWPC that is going to be installed in the SAXS station of BM16 at the ESRF (C=22pF; L=54nH; R_L=35mΩ). The use of this inductance is highly recommended due to its low series resistance; what reduces the pulse amplitude attenuation at the delay line. The A design of delay line is chosen due to its better performance.

The prototype has 128 cells. Its delay line has the following characteristics: t_{cell}=1.2ns; T_{total}=155ns; Z_0=49.5Ω; R_{tot}=4.4Ω; f_c=145MHz; and, t_r=2.4ns. The frequency response will be very similar to the A design of the delay line (see **Figure 3.21**).

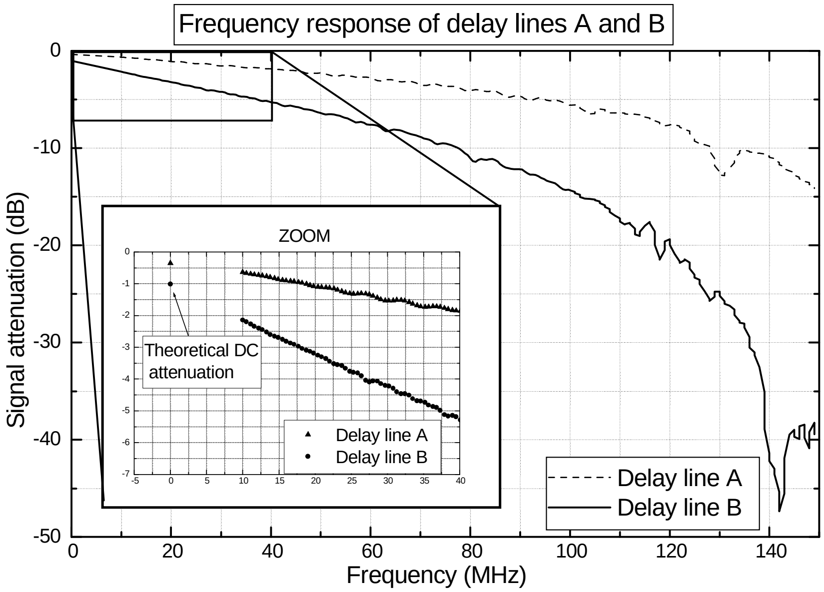

Figure 3. 21 Frequency response of delay lines A and B. A zoom of the frequency range 0-40MHz is shown.

3.3.3. Preamplifiers

The signals of the anode and cathodes need to be amplified. This is because they are too small for to be treated by the CFD. The amplification is done with five transimpedance preamplifiers (2 per delay line x 2 delay lines + 1 anode). These devices amplify the input current and generate an output pulse; whose amplitude is proportional to the input current. This is true if the input pulse width is longer than the preamplifier response time [KNOLL2000].

The requirements for these devices are a large amplification, in a large bandwidth, and a low noise. In other words, they require a large signal to noise ratio. They have also to match the delay line Z_0. Moreover, they are must be stable and discharges hard.

A commercial preamplifier (Femto HCA-40M-100K-C) with a gain of 10^5V/A and a bandwidth of 40MHz [FEMTO2005] is used for the MRMC tests. This preamplifier is chosen because it has been already used by the detectors group showing good spark hardness. This is important since the response of the prototype is not known.

Frequency response

The frequency response of the preamplifier is tested with a spectrum analyzer Agilent CSA N1996A and with a network analyzer Agilent ENA E5071B (see **Figure 3. 22**). The values of the frequency response (expressed in dB) are positive because the preamplifiers amplify the signal.

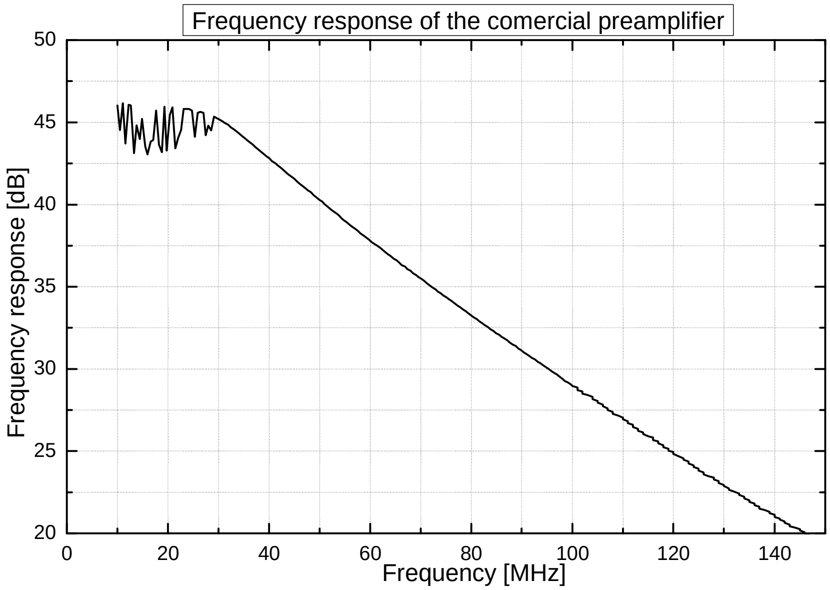

Figure 3. 22 Frequency response of the preamplifier.

Studying the pulse at the output of the preamplifier and using the frequency responses of the delay line and the preamplifier (see **Figure 3.21** and **Figure 3.22**), the frequency structure of the pulses generated at the detector can be deduced.

Signal-to-noise

One of the figures of merit of the gas proportional chambers is that they are single photon counters. With the appropriate DAQ and the absence of noise, this would lead to an infinite dynamic range. This is the detector goal for some experiments which need to differentiate between diffraction spots an intensity difference of some orders of magnitude.

The signals received by the DAQ are the addition of event pulses and noise. Both have an amplitude distribution. The noise of the input signal at the CFD is the addition of the detector noise (amplified by the preamplifier) and the preamplifier noise itself.

The signal amplitude, or the noise amplitude, is not a single value but a distribution. In order to suppress the noise, a threshold is set by the CFD. For this purpose, it is needed that the distribution of signals amplitude of the event pulses does not overlap with the distribution of noise amplitude. It is said that the system is working properly is the two distributions, events and noise, are completely separated.

3.3.4. Constant Fraction Discriminator (CFD)

The CFD determines the arriving time of each pulse, and it generates a digital pulse at that time. Every pulse has a different amplitude, rise time and noise. When determining the arriving time of the pulse, two effects can introduce uncertainties: the noise and the differences in amplitude and rise time. These variations are reduced employing an algorithm called *Constant Fraction Timing*. Its working principle is described. Firstly it inverts and multiplies the signal by a given factor. Then, it adds this new pulse to the original one. Finally, it determines the arriving time as the time the final pulse crosses the 0V.

A Philips Scientific CFTD 715 with 75ps time resolution is used. The preamplifier cathodes total length is L=50mm and the total delay of the delay line is T=155ns. The correspondence space/time is 161.3µm/ns. Thus, the corresponding maximum spatial resolution this CFD can perform with this system is (0.075ns)*(161.3µm/ns) =12.1µm. It fulfills our spatial resolution requirements.

3.3.5. Time to Digital Converser

The TDC solves the position of the event from the five digital signals generated by the CFD. When it receives a signal from the anode channel of the CFD, it opens a *time window* larger than the delay time (T). If, during this period, it receives one signal from each cathode channel of the CFD, it determines the event position in coordinates x and y.

$$x = \frac{(t_{X1} - t_{X2}) + T}{2 \cdot T} \cdot L \qquad (3.\ 7)$$

where x is the event position; t_{x1} and t_{x2} are the arriving times of the pulses at each side of the delay line; and, L is the cathode length. Finally, it sends the (x,y) position to the histogramming card. A TDC developed at the ESRF is used: the N110 [HERVE2004b].

The TDC opens a time window when an anode pulse arrives. During this period, the TDC expects one pulse from each cathode channel. However, at high count rates, other pulses can arrive to the TDC during the time window. In this case, the TDC rejects both events because it can not distinguish which pulses come from which event. This introduces a limit regarding to the count rate. The count rate is also limited by the *recovery time* (RT). This is the time the TDC needs to determine the event position and send the information to the histogramming card.

The count rate capabilities of the TDC-N110 are studied in order to determine if it can fulfil the detector requirements or not.

Count rate tests of the N110

The count rate limits of the TDC are studied. The signals from the CFD are simulated with a pulse generator. The TDC time window is set to 200ns and the output count rate is stored as a function of the input pulse rate (see **Figure 3. 23**). The time between pulses is uniform.

Three regimes are observed. The first one is the *acceptation* regime which covers the input rates from 0 to ${}^{1}\!/_{(T+RT)}$. It can be observed that, in this regime, the output count rate is the same as the input rate. This is because after one event, the next pulse arrives after the time window and the recovery time of the first event; and thus, all the events are stored (see **Figure 3. 24**).

The second regime is the *partial rejection* regime which covers the input rates from ${}^{1}\!/_{(T+RT)}$ to ${}^{1}\!/_{T}$. In this regime, the output count rate is half of the input rate. This is because after one event, the next one arrives during the recovery time. It allows the TDC to solve the position of the first event, but it does not open the time window for the second event (see **Figure 3. 25**).

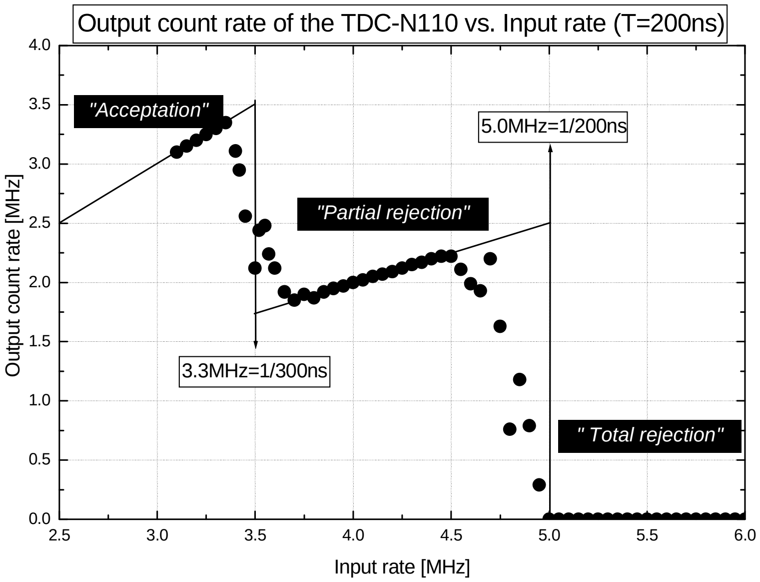

Figure 3. 23 Output count rate of the TDC-N110 as a function of its input rate. The time window is 200ns. A pulse generator is used to simulate the input signals.

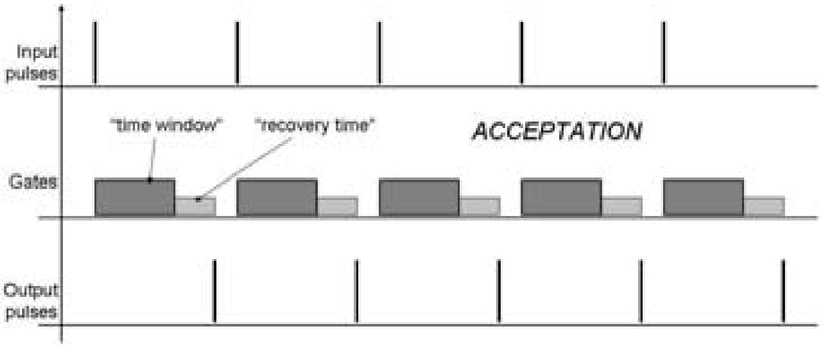

Figure 3. 24 Acceptation regime scheme of the TDC-N110.

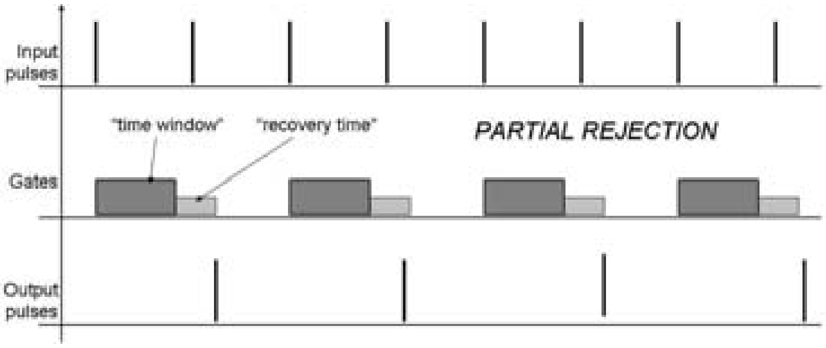

Figure 3. 25 Loosing regime scheme of the TDC-N110.

Finally, the third regime is the *total rejection* regime which covers input rates from $1/T$ to higher values. In this regime, the count rate is zero. This is because after one pulse, the next one arrives in the time window of the first one, rejecting both events (see **Figure 3. 26**).

Figure 3. 26 Rejection regime scheme of the TDC-N110.

From **Figure 3. 23**, $3.33MHz = 1/(T + RT)$ and $3MHz = 1/T$. As the total delay is T=200ns, the recovery time is RT=100ns.

Simulation of the N110 count rate capabilities

The count rate capabilities of the TDC-N110 are estimated here. The time distribution of the events detected by the detector is first discussed.

The electron bunches in the storage ring have a pulsed time structure. The time between bunches is ~2ns [MUÑOZ2006]. Consequently, the distribution of time between photoionizations has also a pulsed time structure. However, the photoionizations are produced along the drift space and the electrons drift time is much larger than the time between bunches. Therefore, the pulsed structure is lost. As a result the time between avalanches in the detector follows a Poisson distribution.

A code that simulates the TDC has been developed. The incoming rate has a Poisson distribution. In **Figure 3. 27** the simulated output count rate of the TDC-N110 is shown as a function of the incoming rate. The TDC-N110 count rate limit (1.11MHz) is much lower than the detector count rate capabilities (see section 4.3).

This TDC does not fulfil the detector requirements in terms of global count rate. However, with the information of **Figure 3.27** this TDC can be used for the determination of the detector count rate. It can also be used to acquire 2D images and therefore study the spatial resolution and the gain uniformity of the prototype.

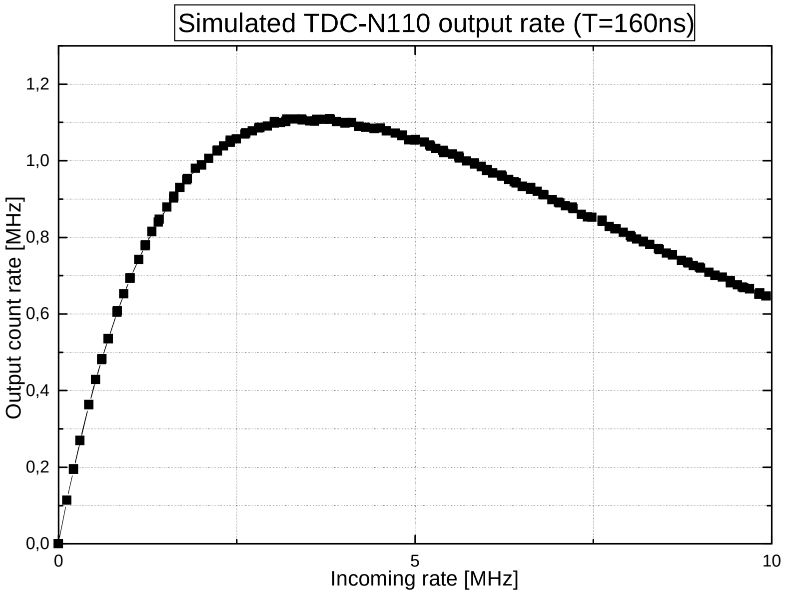

Figure 3. 27 Simulated TDC-N110 output rate as a function of the input rate (Poisson). The time window is set to 160ns. The maximum output count rate is 1.11MHz; which is achieved at a Poisson input rate of 3.62MHz.

3.3.6. Histogramming card

The last device of the data acquisition system is the histogramming card. This device stores the events in a 2D histogram.

The DAQ system must generate histograms from the digital input coming asynchronously from the TDC. The acquisition time is split into frames, each consisting of a live time and a dead time. A histogram is built for each frame during the live time. A set of up to 1024 frames, each identified by a frame number, form a cycle. A configurable number of cycles form a run. Histogram data are accumulated for each frame number across all cycles and thus the histogramming memory contains a maximum of 1024 histograms regardless of the number of cycles in the run. Live and dead times for each frame in the cycle must be programmable. Depending on the type of experiment, histogram sizes range from 64x64 up to 8192x8192 points, with a pixel depth of 8, 16 or 32 bit. A buffering space of 256 MByte is required to acquire a large number (up to 1024) images. The system must allow the selection of a region of interest (ROI) and accept either 1-D or 2-D images. Additionally, at the same time the card is producing a histogram, the DAQ system must count events on eight scaler inputs and output a data pattern on eight TTL outputs used for experiment control (increasing or decreasing the temperature of the sample) and synchronization (opening and closing the shutter).

A new PCI card for the Data Acquisition system (DAQ) has been built (see **Figure 3. 28**)in collaboration with the Electronic Engineering Department of the University of Valencia [TOLEDO2004]. The board combines a large on-board 256-MByte histogramming memory with a maximum 10-MHz count rate in continuous operation and integrates the time frame generation, histogram building and buffering functionalities in a single PCI board, resulting in a fast, compact and cost-effective data acquisition solution.

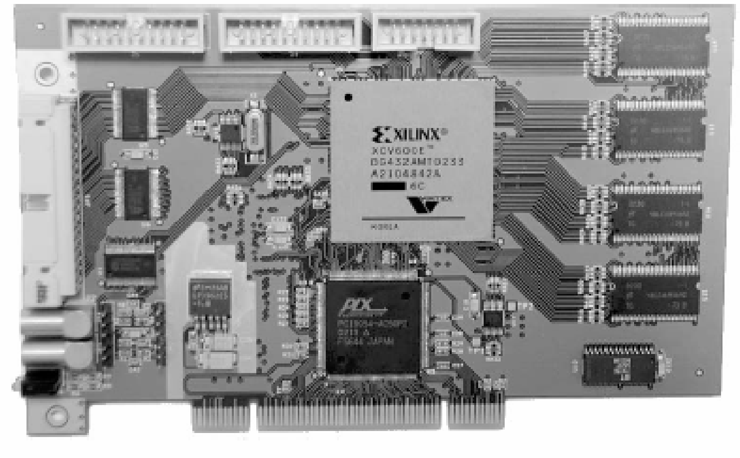

Figure 3. 28 In-house DAQ histogramming board.

3.3.7. Future perspectives of the readout system

The N110 TDC does not fulfil the count rates requirements of the detector system because it can only performs a count rate equal of few MHz (see subsection 3.3.5). The TDC also limits the count rate capabilities of our delay line based readout system because it can not solve different events that have arrived with a time difference shorter than T. An upgrade of the delay line based readout system is being designed in order to enhance the count rate capabilities of the readout system.

Improvements of the delay line based readout system

Theoretically, the position of different events arriving in the time window can be solved. It has been seen that the position of one event is solved making the subtraction of the arriving times of the two sides of one cathode (t_{x1} and t_{x2}). If different pulses arrive at each side of the delay line, the correspondence between pulses can be found checking the addition of times

$$T = t_{X1} + t_{X2} + \Delta t_{ress} \tag{3. 8}$$

where Δt_{ress} is the time acceptance (the time resolution). This time resolution defines the margin of agreement of correlation between two pulses (of each side of the delay line). In this case, the limit of the TDC would not the time window, but the pulses time resolution and the velocity of the TDC.

A new DAQ based on a TDC which can handles different events at the same time is under study. This system could perform a mean count rate of 40MHz (TOLEDO2006).

Parallel readout system

During the design of the MRMC, a parallel readout was planned to be implemented: the BLADE [HERVE2004a]. Its development was done in collaboration with the ESRF. A summary of its detector boundary conditions is shown in **Table 3. 1**.

The MRMC was designed to be compatible with this system. Therefore, some of these boundary conditions were constrains for the MRMC during its design phase

Characteristic	Value
Local count rate	10^6 cps/mm^2 typ.
Strip charge generated	50000 e- (~8 fC) typ.
Strip (or grid) charge time collection	20 ns typ.
Strip to strip skew	4 ns max.
Strip + cabling capacitance	20 pF max.
Single event to number of strips fired	3 typ.
Grid charge generated	90000 e- (~14 fC) min.
Grid + cabling capacitance	50 pF max.
Radiation hardness	By detector mechanical design

Table 3. 1 Boundary conditions between the BLADE parallel readout system and the detector**.**

4.Simulations

In this chapter we describe the simulation work; that characterizes the dependences between the detector features and the detector building and operating parameters. This knowledge is required to optimize the detector response when choosing the detector parameters (see next chapter).

In the first section the spatial resolution of the detector is simulated, as well as the detection efficiency. A Monte-Carlo based program has been developed to simulate the spatial resolution as a function of the x-ray energy; the parallax; the gas mixture; the drift field; the drift distance; the mesh cell size; and, the pixel size. It also computes the x-ray absorption efficiency as a function of the x-rays energy; the window materials and thicknesses; the gas mixture; and, the drift distance.

In section 4.2 the simulations of the three detection characteristics which require the 3D simulation of the movement of charged particles are presented. Firstly, the *mesh transparency* is estimated. It is the ratio between the primary electrons that crosses the mesh and the electrons that reach the mesh. Secondly, the gain and the induced signals at the different electrodes are simulated with a specific code that we have developed. Thirdly, two characteristics of the avalanche ions drift are simulated: the ion drift paths and the ion drift time.

In section 4.3, two different parameters are simulated: the strip to anode capacitance and the crosstalk between cathode strips. Both play an important role on the readout noise. The electronics engineering department of the Universitat Autònoma de Barcelona has collaborated with us to develop these simulations.

4.1. Spatial resolution

The spatial resolution of a detection system is the minimum distance between two different parallel and extremely thin beams that can be distinguished on the acquired image. The spatial resolution is limited by the *point spread function* (PSF). The PSF is the acquired image of an extremely thin dispersion free x-ray beam, and it usually follows a Gaussian distribution at the central part. The spatial resolution is defined as the FWHM of the PSF. In order to enhance the spatial resolution of the detector, the FWHM of the PSF must be reduced. Different factors introduce the dispersion in the PSF. These are the parallax, the detector factors and the readout factors.

Parallax

The parallax occurs when the beam enters into a gas detector with an incident angle. Under these circumstances, the projection of the photoelectric positions on the detection plane is not a point but a line. Consequently, the detected position on the detection plane is extended (see **Figure 4. 1**).

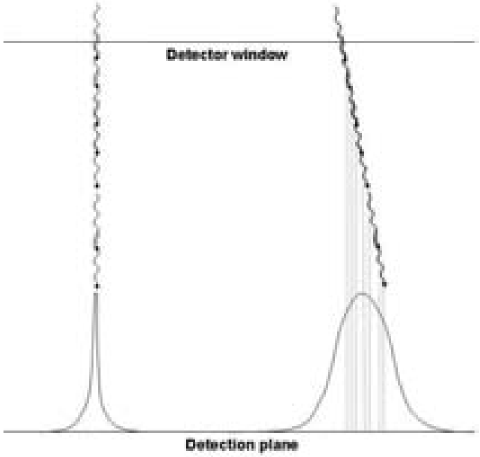

Figure 4. 1 Parallax effect on the PSF. The arrow heads represent the photoelectric effect points. The dotted lines represent the projected positions on the multiplication/readout plane.

Detector factors

The detector factors that worsen the PSF are the photoelectric size, the primary electron drift and the sampling of the primary electrons. When the photoelectric effect occurs, a photoelectron with energy equal to the x-ray energy minus the binding energy is ejected. The photoelectron ionizes the gas atoms along its path until it is thermalized. Thus, the primary electrons are not produced on the photoelectric interaction point, but on the surroundings. Besides, the excited atom releases its energy through an Auger electron or fluorescence. These processes also leave primary electrons away from the photoelectric effect point. The *photoelectric size* is the width of the primary electron distribution (2.35·sigma) after the photoelectric effect and the de-excitation processes. The detector computes the position of the x-ray through the position of the primary electrons. Consequently, the detected position depends on the photoelectron, Auger and/or fluorescence emission angles and ranges. The photoelectric size is one of the largest effects regarding on the worsening of the spatial resolution.

The second factor is the primary electron drift. The error on determining the mean primary electron position is enlarged because the electrons are diffused when drifting to the amplification region. The information of their initial position is diffused worsening the PSF.

The third factor is the "grouping" in discrete positions of the primary electrons when arriving to the amplification/readout plane. In the case of the MRMC, the primary electrons are detected on the holes positions. In the case of a MWPC the electrons are detected along the anode wires. Due to this grouping, some information about the arriving position on the amplification/readout plane is lost and therefore, the spatial resolution is worsened.

Readout factors

They are the electronic noise, the delay line errors and the sampling of the arriving positions. The signal noise of a pulse causes errors when determining its arriving time. It implies an error on the position determination that enlarges the PSF, if delay line readout is used.

The delay line errors are the variations on the delay time in some cells due to variations of the specified values of the components of the delay line. Moreover, the delay line attenuates the different frequencies of the pulses with different attenuations (see **Figure 3.21**). The arriving pulse times are distorted by these errors and, as explained above, the spatial resolution is worsened.

When storing the x-rays arriving positions in a digital image, there are a finite number of possible stored positions. Because part of the arriving position information is lost, the spatial resolution of the system is worsened.

We call the *detector PSF* to the acquired image of a beam with size, dispersion and parallax equal to zero and considering no errors from the readout, sampling or storing.

4.1.1. Detector physics simulator

A program has been written with three main objectives. The first objective is to estimate the position distribution of the primary electrons arriving to the cathode mesh. It allows us to compute the *strip fired number*; the number of strips which detects primary electrons. This magnitude has to be equal or lower than three if parallel readout is used (see subsection 3.3.7). The second objective is to simulate the position distribution of events stored by the detection system. This is necessary to simulate the PSF and the spatial resolution. The third objective is to compute the ratio between the number of x-rays that interact with the gas and the initial number of x-rays; the *detector efficiency*.

The whole simulation involves different processes with different probability distributions. Due to the stochastic nature of the different simulated processes, a Monte-Carlo based simulation program is needed. The program computes first the x-ray interaction point, the photoelectron emission direction and range, the de-excitation mechanism of the excited ion, the fluorescence x-ray interaction point, the Auger emission angle and range… The positions of the primary electrons in the chamber are determined with these calculations. Then, the simulator drifts the primary electrons to the amplification/readout plane and stores their arriving hole position. The event position is stored as the mean primary electron arriving position. This process is repeated a given number of times generating an event position distribution: the detector PSF. The event position distribution is convoluted with a step function with a step size equal to the pixel size. This shows the spatial resolution of the acquired image, assuming zero readout noise. The real spatial resolution is worst than the simulated one because the electronic noise is not taken into account. Besides, the event position is computed as the mean final position of the primary electrons. In other words, a perfect readout system is supposed.

In **Figure 4. 2** a snapshot of the simulator is shown. Above the progress bar (horizontal blue line) the detector and beam parameters which can be changed are shown. They are grouped in different categories. Below the task bar there are the results. Some of the objects of the simulator are described:

- The “Hole/wire pitch” (in the Sampling zone) is the cell size (distance between anode wires at a MWPC).

- The position of an event is the average of the final primary electrons positions of that event (no electronic noise). Then, the “Mean beam position” is defined as the mean position of the events position.
- 2.35*sigma of the primary electrons positions of one event gives an idea of the size of its electron cloud; the event size. The “Mean 2.35*sigma of primary electrons distribution” is the average of the event size for all the events.
- The “beam 2.35*sigma” is the 2.35*sigma of the events position distribution. After the anode split, it is the FWHM of the PSF.
- The “simulated spatial resolution at histogram” is the FWHM of the convolution of the detector PSF with a step function with a step width equal to the pixel size.

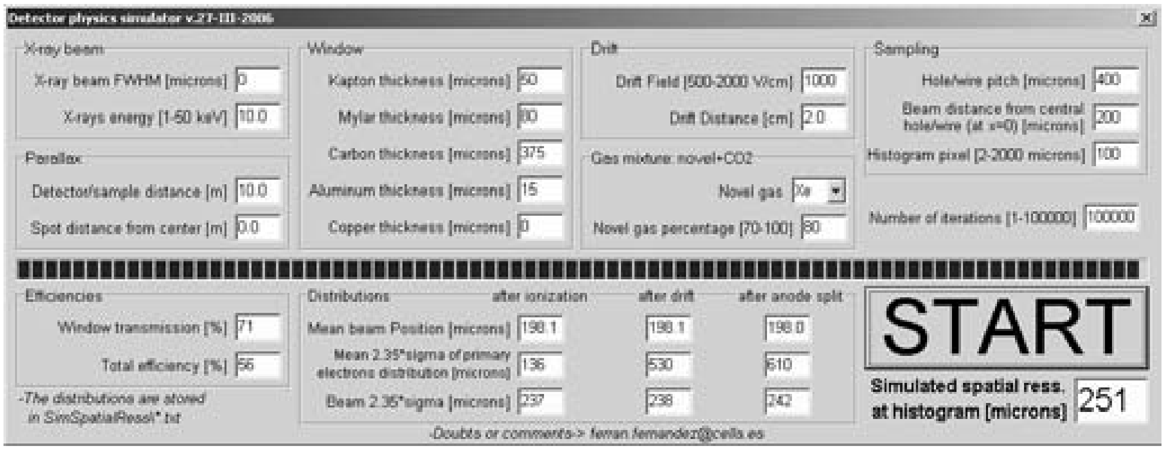

X-ray beam
X-ray beam FWHM [microns] 0
X-rays energy [1-50 keV] 10.0

Parallax
Detector/sample distance [m] 10.0
Spot distance from center [m] 0.0

Window
Kapton thickness [microns] 50
Mylar thickness [microns] 80
Carbon thickness [microns] 375
Aluminum thickness [microns] 15
Copper thickness [microns] 0

Drift
Drift Field [500-2000 V/cm] 1000
Drift Distance [cm] 2.0

Gas mixture: novel+CO2
Novel gas Xe
Novel gas percentage [70-100] 80

Sampling
Hole/wire pitch [microns] 400
Beam distance from central hole/wire (at x=0) [microns] 200
Histogram pixel [2-2000 microns] 100

Number of iterations [1-100000] 100000

Efficiencies
Window transmission [%] 71
Total efficiency [%] 56

-The distributions are stored in SimSpatialResol*.txt

Distributions	after ionization	after drift	after anode split
Mean beam Position [microns]	198.1	198.1	198.0
Mean 2.35*sigma of primary electrons distribution [microns]	136	530	610
Beam 2.35*sigma [microns]	237	238	242

Simulated spatial ress. at histogram [microns] 251

-Doubts or comments-> ferran.fernandez@cells.es

Figure 4. 2 Detector physics simulator snapshot.

4.1.2. X-ray energy dependence

Roughly speaking, the cross section of the photoelectric effect decreases with the x-ray energy in the energy range we are interested. Therefore, higher the x-ray energy is; the higher the window and gas transmission are, increasing the number of x-rays that can interact with the gas.

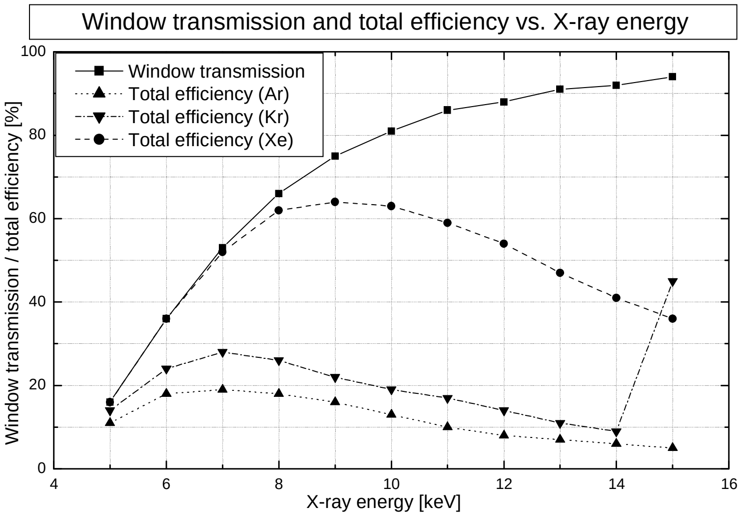

Figure 4. 3 Window transmission and total efficiency as a function of the x-ray energy. The drift distance is 2cm. Each gas mixture is composed by 80% of noble gas plus 20% o CO2. The window consists in 375µm of carbon plus 25µm of Kapton plus 30µm of charged Kapton.

The window transmission and the total efficiency are simulated (see **Figure 4. 3**) for three different gas mixtures. The Krypton based gas mixture has the higher efficiency at 15keV. This is because only for Eγ>14.3keV the photoelectric effect can occur with electrons of the K shell, and therefore the cross section increases drastically.

In many experiments a minimum count rate is needed. Nevertheless, the dose which the sample can support, in terms of radiation damage, is limited and therefore the beam intensity can not be increased freely. As a consequence, a minimum total efficiency exists. This limit is considered to be 50%, for many experiments.

Concerning about the spatial resolution, different effects related to this figure of merit takes place when varying the x-ray energy. The first one is the photoelectric size. The distance needed to thermalize a photoelectron depends on its energy. The higher the x-ray energy is; the higher the photoelectron energy is; and therefore, the larger the photoelectron path is. Therefore, the primary electron distribution after the photoelectric effect is larger for higher x-ray energies, worsening the spatial resolution.

The photoelectric size is simulated as a function of the x-ray energy for different gas mixtures. The results are shown in **Figure 4. 4**. It can be observed that for Kr the photoelectric size for x-rays of 14keV is worst (larger) than for x-rays of 15keV. This is because for energies higher than 14.3keV the photoelectric effect can occur with electrons of the K shell, decreasing the range of the photoelectron.

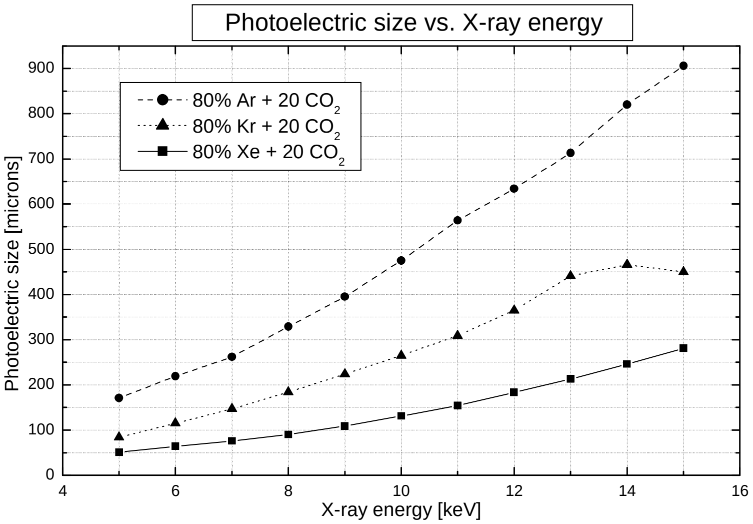

Figure 4. 4 Photoelectric size as a function of the x-ray energy.

The second effect related with the spatial resolution when increasing the x-ray energy is related with the photon interaction coefficient. The shorter the photon interaction is; the larger the mean distance the primary electrons have to drift is; what enlarges the size of the primary electron cloud and therefore, worsens the spatial resolution. This effect is much less important than the photoelectric size dependence.

In order to simulate the spatial resolution of the detector for different x-ray energies, we first simulate the detector PSF (see **Figure 4. 5)**. In **Figure 4. 5** the central peak corresponds to the L shell ionization. The other counts, inside the dashed ellipse, correspond to the photoionizations of the M shell (lower binding energy); which releases a more energetic photoelectron. In **Figure**

4. 5 the M shell counts are 20% of the total counts; which corresponds to the known proportion of photoionization between the M and L shells (see **Table 2.4**).

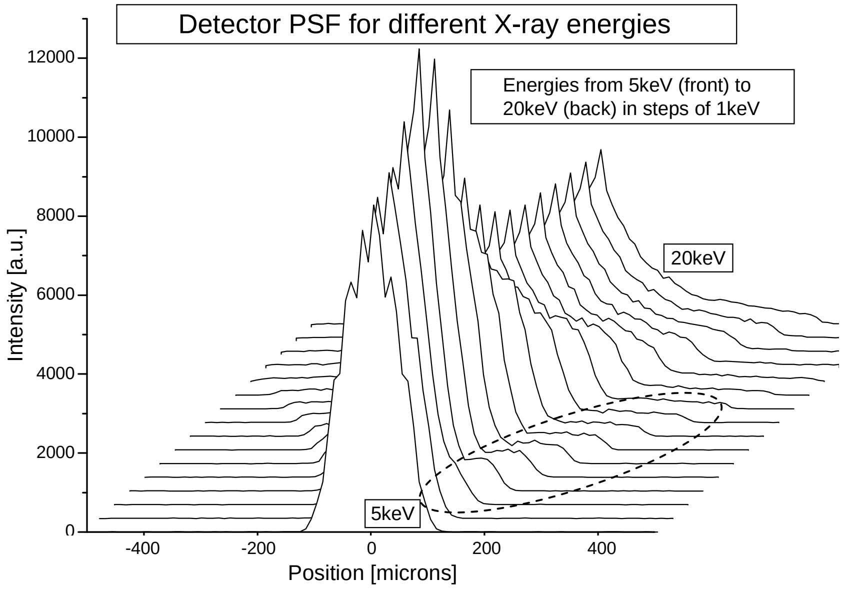

Figure 4. 5 Detector PSF for different x-ray energies. The gas mixture is composed by 80% Xe + 20% CO2, the drift field is 1000V/cm; the drift distance is 2cm; the hole-hole distance is 400µm, the beam is placed at 100µm from the central hole, the pixel size is 100µm, and; the beam parallax and beam size are set to zero. The counts in the dashed ellipse come from the M shell photoionizations.

The spatial resolution of the detector as a function of the x-ray energy is simulated for different gas mixtures (see **Figure 4. 6**).

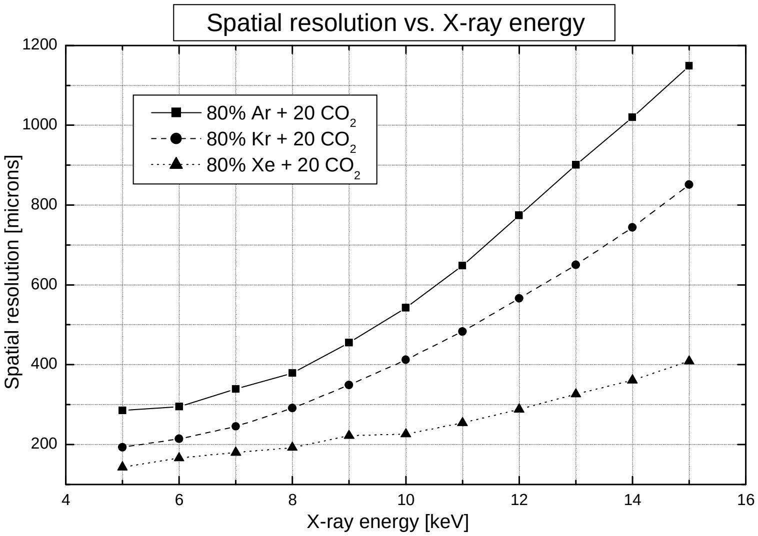

Figure 4. 6 Spatial resolution as a function of the x-ray energy. The parameters are equal than **Figure 4. 5.**

4.1.3. Beam incident angle dependence (parallax)

The parallax changes the PSF. The PSF (see **Figure 4. 7**) and the spatial resolutions (see **Figure 4. 8**) for different beam incident angles are simulated.

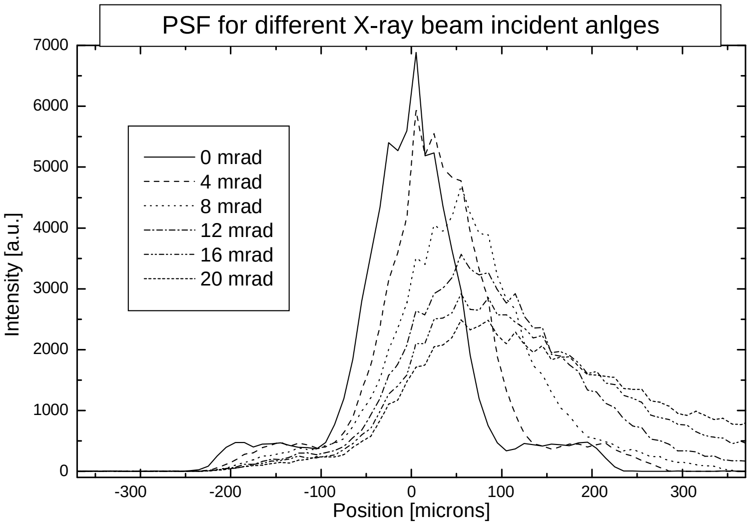

Figure 4. 7 PSF for different beam incident angles. The parameters are equal than **Figure 4. 5** but with fixed x-ray energy (10keV) and a variable incident angle.

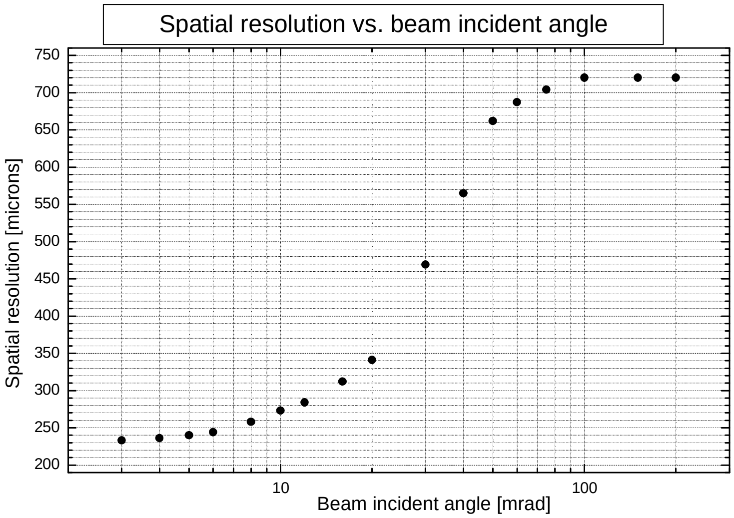

Figure 4. 8 Spatial resolution as a function of the beam incident angle. The parameters are equal than **Figure 4. 5**, but with a fixed x-ray energy (10keV) and a variable incident angle. The angle of 10mrad correspond to a detector distance equal to 10m with a sample-to-detector distance equal to 10cm.

From **Figure 4. 7** it can be deduced that the detected position is not equal to the position of the beam at the window. This is not important since it can be corrected by software a posteriori, having the correlation between the detected position and the position of the beam at the window over all the detection area. This calibration can be easily done irradiating the detector uniformly from the sample position with a mask, consisting of a layer with equally spaced small holes, placed on the window.

It is also observed that the PSF is wider for inclined beams than for the vertical beam. Consequently, the spatial resolution depredates when inclining the x-ray beam. This is observed in Figure 4. 8**.**

4.1.4. Drift distance dependence

Two parameters change when varying the drift distance: the total efficiency and the mean distance the primary electrons have to travel. The variation of the mean primary electron drift distance changes the mean size of the primary electron cloud arriving at the mesh. This implies a variation on the spatial resolution, the strip fired number and the local count rate.

We show in this section the variations of the total efficiency, the spatial resolution and the strip fired number as a function of the drift distance. The local count rate is studied in subsection 4.2.4.

Total efficiency

The total efficiency as a function of the drift distance is simulated (see **Figure 4. 9)**.

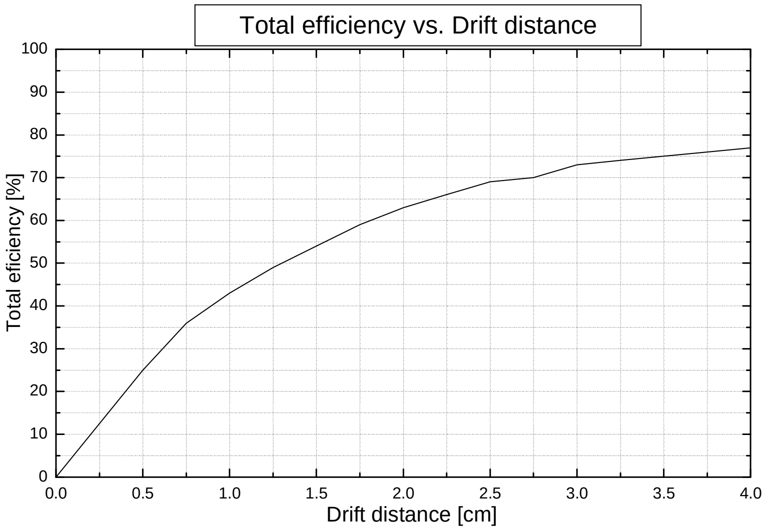

Figure 4. 9 Total efficiency as a function of the drift distance. The x-ray energy is 10keV, the gas mixture is Xe 90% + CO2 10%. The window is formed by 375µm of carbon and 55µm of kapton; which has a transparency of 81%. **I**n order to have a total efficiency>50%, a drift distance>1.3cm is needed

Spatial resolution

Due to the diffusion of the electrons during the drift, the size of the primary electron cloud is larger for larger drift distances. The stored position of each event is the mean position of the primary electrons. Consequently, when the positions of the primary electrons are distorted by the diffusion, the point spread function becomes slightly wider. The simulations of the spatial resolution and the electron cloud size shows the proportionality between both parameters under the variation of the drift distance (see **Figure 4. 10**).

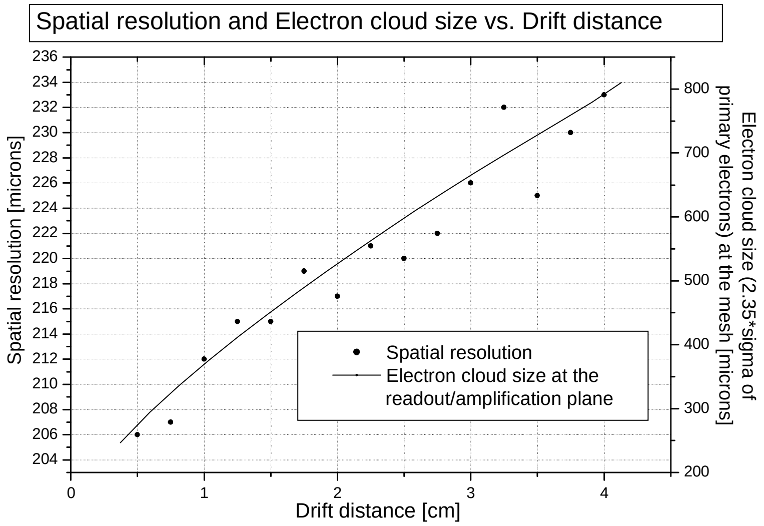

Figure 4. 10 Spatial resolution and electron cloud size at the readout/amplification plane as a function of the drift distance. The detector parameters are equal to the **Figure 4. 9** but the beam distance from the central hole radius is zero.

Another important aspect of the electron cloud size related to the spatial resolution is its value with respect to the cell size. This effect is explained in subsection 4.1.8**.**

Strip fired number

The larger the drift distance is; the larger the electron cloud size at the cathodes mesh is; and therefore, the larger the strip fired number is (see **Figure 4. 11**).

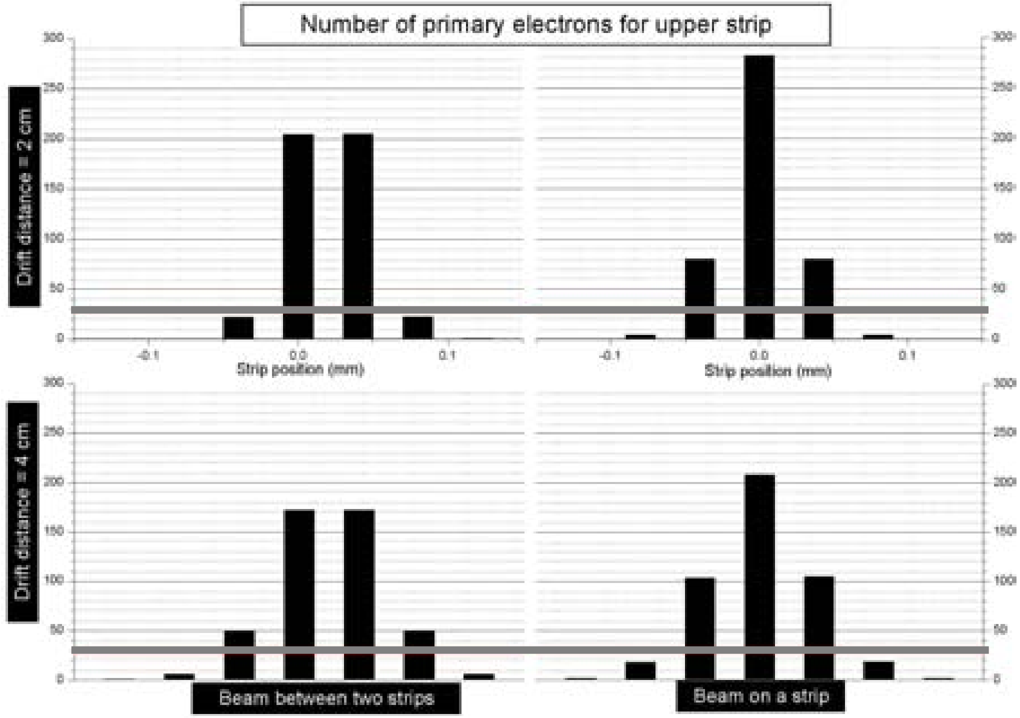

Figure 4. 11 Number of primary electrons detected at each upper cathode strip. The grey lines indicate a possible threshold levels for the electronics. The detector parameters are equal to the **Figure 4. 9**.

4.1.5. Drift field dependence

As it can be seen in **Figure 2.13**, the diffusion coefficients vary as a function of the electric field. Therefore, the size of the primary electron cloud varies when changing the drift field (see **Figure 4. 12**). With the parameters used in **Figure 4. 12**, the primary electron cloud size increases when increasing the drift field; what has the implications explained in the last section.

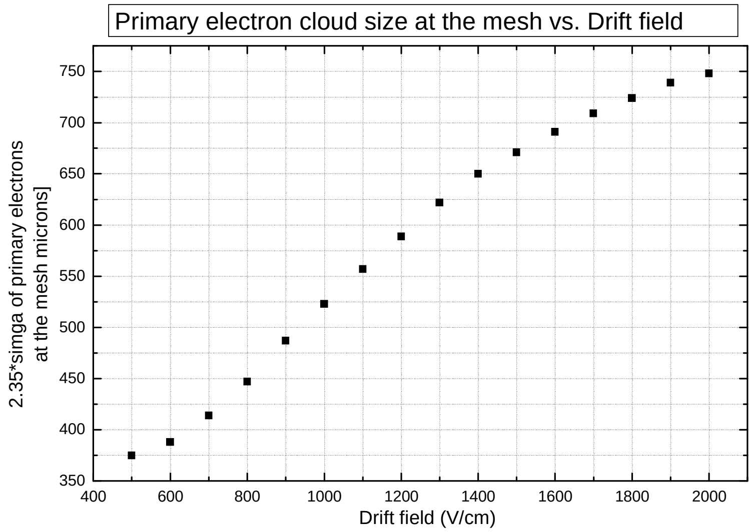

Figure 4. 12 Primary electron cloud size at the cathodes mesh as a function of the drift field. The x-ray energy is 10keV, the gas mixture is Xe 90% + CO_2 10%, the drift distance is 2cm, the hole-hole distance is 400µm, the beam is placed on a hole, the pixel size is 100µm, and; the beam parallax and beam size are set to zero.

4.1.6. Noble gas dependence

In the previous simulations we have taken into account three different noble gases: Ar, Kr and Xe. Their main detection characteristics of these gases are simulated (see **Table 4. 1**).

	Ar			Kr			Xe		
	8keV	10keV	12keV	8keV	10keV	12keV	8keV	10keV	12keV
Minimum drift distance 50% total efficiency (cm)	9	12	16.5	5.7	7	10	1.0	1.3	1.9
Photoelectric size (µm)	310	470	620	185	266	360	93	132	181
Primary electrons cloud size at the mesh (µm) (drift distance =2cm)	1250	1426	1675	1000	1100	1305	367	419	508
Spatial resolution (µm)	368	420	759	287	410	566	206	220	270

Table 4. 1 Different simulated detection characteristics for Ar, Kr, and Xe based gas mixtures. In these simulations, quenching gas is CO_2 20%, the drift field is 1000V/cm, the cell size is 400µm, the pixel size is 100µm and the beam is placed on a hole.

4.1.7. Quenching gas proportion dependence

The proportion of quenching gas affects mainly two characteristics of the gas mixture: the mean Z and the quenching power. The change of the mean Z has the same effect as changing the noble gas (see last section). The best simulated detector features are performed by the lowest quenching gas proportions. However, the detector can not be operated without any quencher because it would detect many events of de-excitations. Consequently, a compromise must be reached. This proportion is set experimentally, as the quench process can not be simulated.

4.1.8. Cell size dependence

The cell size conditions the precision on determining the position of the x-ray. This is because the primary electron cloud is sampled when it crosses the readout mesh through the holes. This effect is negligible if the cell size is smaller than the primary electron cloud size at the mesh. If not, the position determination of the event can suffer large errors (see **Figure 4. 13**).

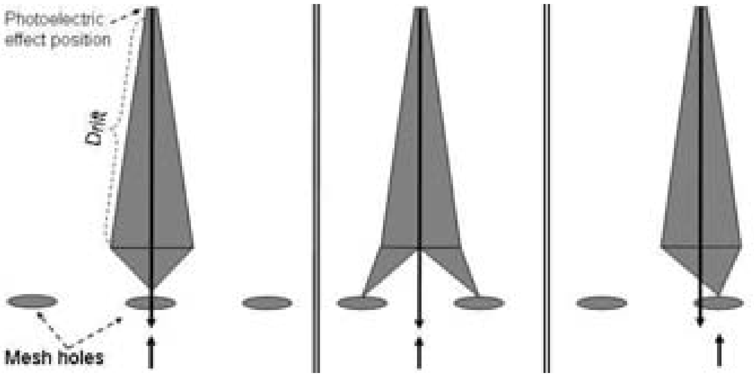

Figure 4. 13 Error on solving the x-ray position. The case at the right shows an error on the position determination.

The error on determining the position of the event due to the cell size is maximum when the x-ray beam is placed a quarter of the cell size from a hole center (see **Figure 4. 14**). The maximum error on determining the position depends also on the primary electron cloud size at the mesh (see **Figure 4. 15).**

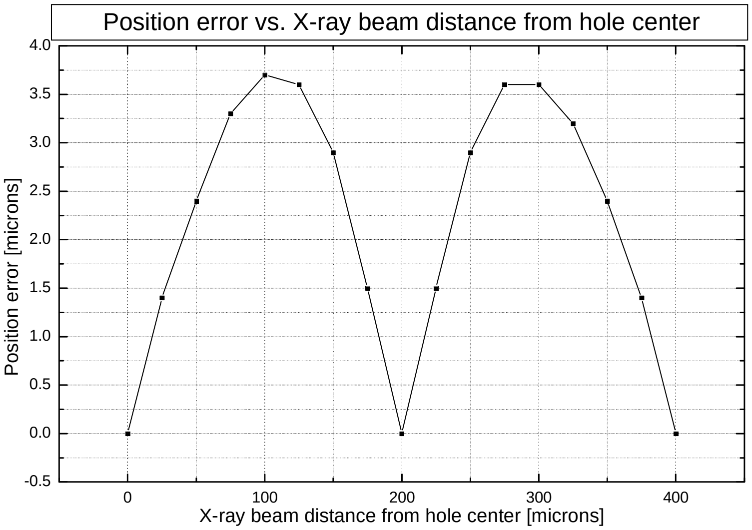

Figure 4. 14 Position error vs. x-ray beam position. The x-ray energy is 10keV, the gas mixture is Xe 90% + CO2 10%, the drift distance is 2cm, the cell size is 400μm and the beam parallax and beam size are set to zero.

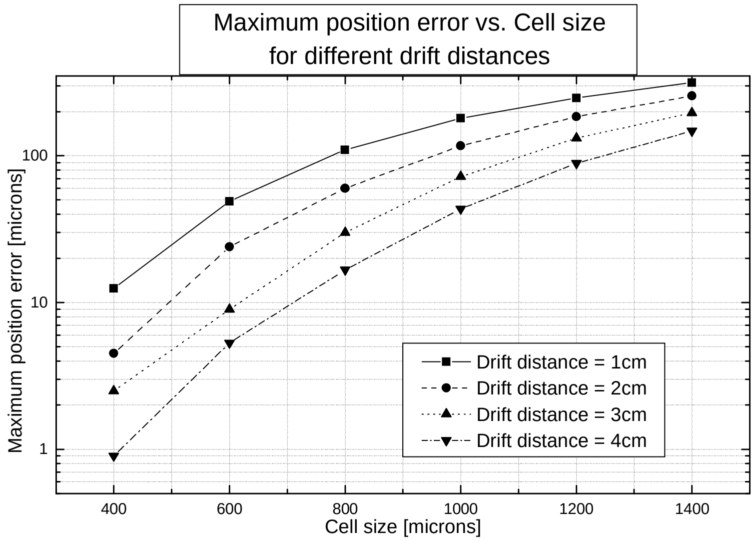

Figure 4. 15 Maximum positioning error vs. Cell size for different drift distances. The x-ray energy is 10keV, the gas mixture is Xe 90% + CO_2 10% and the beam parallax and beam size are set to zero.

The cell size obviously introduces geometrical constrains to the different cathodes mesh parameters. It conditions the maximum radius of the lower cathode holes; what determines the maximum radius of the upper cathode holes and the pillar radius; what determines the maximum pillar height.... These geometric constrains condition the gain, the signal, the local count rate and the mesh transparency; which and are studied in later sections.

4.1.9. Pixel size dependence

The point spread function is the convolution of different effects that distorts the x-ray detection. The sampling of the data, when storing it to a digital image, is one of these effects. The spatial resolution is the FWHM of the convolution of the detector PSF with a step function with a step size equal to the pixel size. This dependence of the spatial resolution on the pixel size can be observed in **Figure 4. 16, Figure 4. 17** and **Figure 4. 18**.

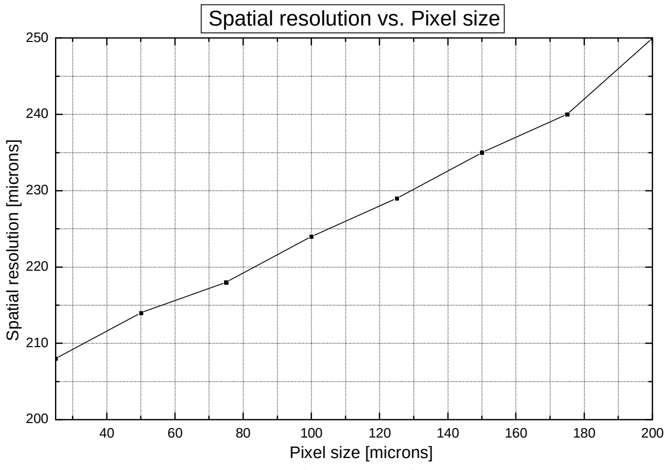

Figure 4. 16 Spatial resolution as a function of the pixel size. The x-ray energy is 10keV, the gas mixture is Xe 90% + CO2 10%, the cell size is 400µm, the drift distance is 2cm, the beam position is 100µm, and the beam parallax and beam size are set to zero

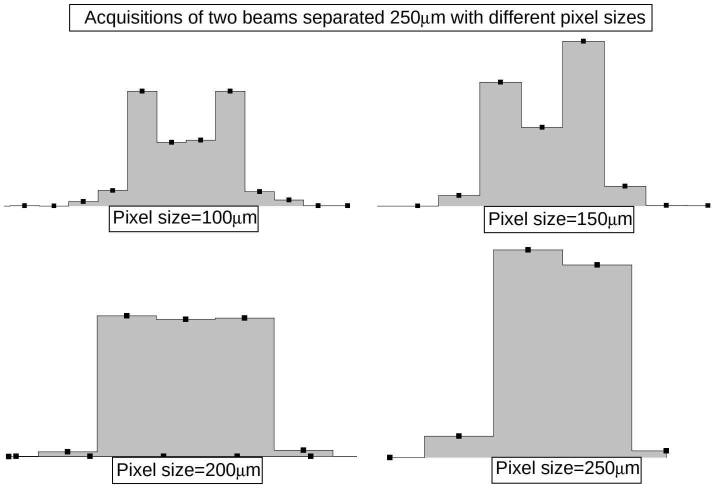

.

Figure 4. 17 Acquisitions of two beams with different separations. The first beam is placed at 100µm from the central hole (at 0µm). The x-ray energy is 10keV, the gas mixture is Xe 90% + CO_2 10%, the drift distance is 2cm, the cell size is 400µm and the beam parallax and beam size are set to zero. The minimum pixel size to distinguish between the two beams is 200µm (see **Figure 4. 16**).

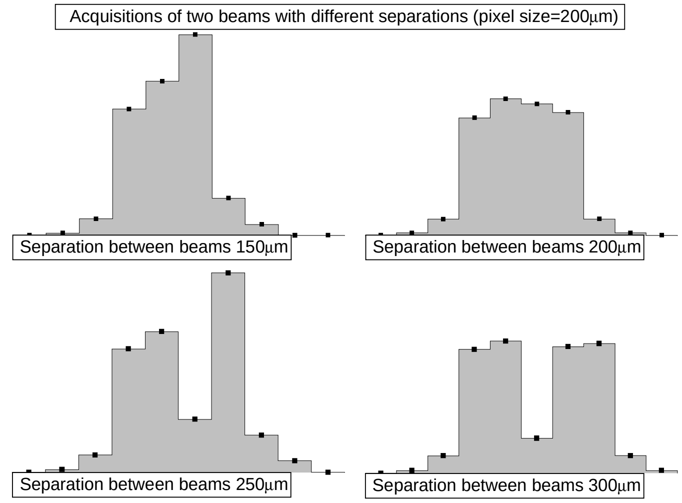

Figure 4. 18 Acquisitions of two beams separated 250µm with different pixel sizes. The first beam is placed at 100µm from the central hole (at 0µm). The x-ray energy is 10keV, the gas mixture is Xe 90% + CO_2 10%, the drift distance is 2cm, the cell size is 400µm and the beam parallax and beam size are set to zero. Under these conditions, a pixel size of 250µm is required to distinguish between the two beams (see **Figure 4. 16**).

4.2. 3D Simulations

In this chapter we show the simulations of the mesh transparency, the avalanche and signal development and the ion drift. These simulations have in common that they need the 3D electric fields to simulate the movement of the charged particles in the chamber. For this purpose it is needed to combine the gas transport properties and the three dimension electric field. The different programs and their associations are described in subsection 4.2.1.

Unless specified, in this section the simulations we show have been done for the optimized MRMC whose parameters are summarized in **Table 5. 1**.

4.2.1. Simulation tools and shell layout

For the simulation of the detector, four different programs have been used: Opera3D [OPERA1997], Magboltz [MAGBOLTZ1995], Heed [HEED1995] and Garfield [VEENHOF2001]. The first one is an electrostatic finite element method simulator. With it, the three dimensional electric fields have been computed for each model of MRMC. Also the weighting fields of the electrodes surrounding the avalanche are also computed with it. The second program solves the Boltzmann transport equations for electrons in gas mixtures under the influence of electric and magnetic fields. The Heed program computes in detail the energy loss of fast charged particles in gases, taking delta electrons and optionally multiple scattering of the incoming particle into account. The program can also simulate the absorption of photons through photo-ionization in gaseous detectors. Finally, Garfield is a gas detector simulator that combines all the data from the other programs to simulate the movement of the charged particles and their multiplication in the detector. This program is nowadays widely used by the scientific community [TIKHONOV2002] and [TSUTOMU2005]. Garfield, that implements Magboltz and Heed, runs under a Linux operative system (in one PC) and Opera3D runs under a Unix operative system (in another PC).

The Opera3D is in fact a package which contains three different programs: the pre-processor, Tosca and the post-processor. The pre-processor (see **Figure 4. 19**) generates the model. It is used to build the structure, set the materials and the boundary conditions (voltages and symmetries) and write the table of node positions. Tosca computes the electric field and potential in all the volume. Finally, the post-processor is used to analyze the results and write the tables of electric fields and potential at the node points. The Garfield program interpolates the electric field and potential in the detector from the files of tables of nodes positions, three electric field components and electric potential.

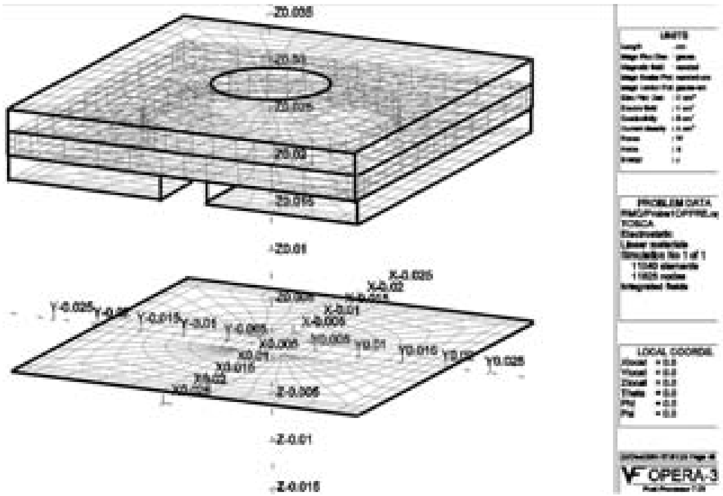

Figure 4. 19 Snapshot of the Opera3D pre-processor. The mesh used to calculate the electric fields and potential can be observed.

Shells layout

Many different models have to be simulated. One script has been written for each computer to automate the process of a model simulation. Their structure is shown in **Figure 4. 20**.

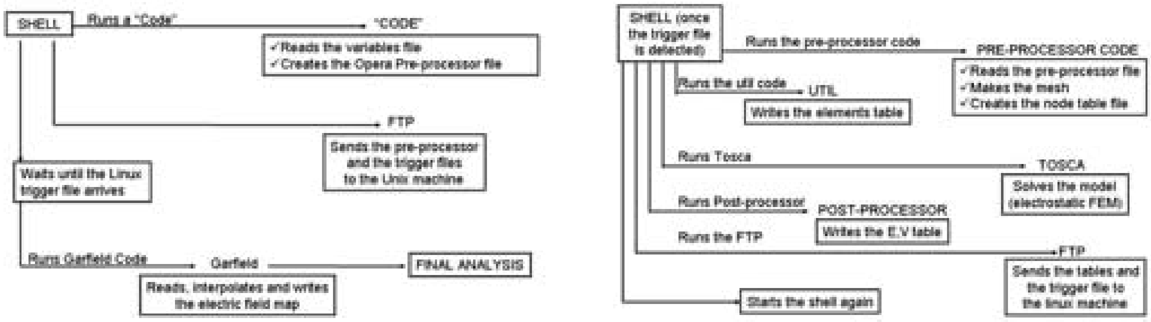

Figure 4. 20 Linux (left) and Unix (right) shells. Once the variables file has been written, the Linux shell is started by the user. The Unix shell is always running, checking every minute if the trigger file exists. When it happens, it starts the steps shown in this scheme.

4.2.2. Mesh transparency

The signal amplitude of the event is proportional to the mesh transparency. In order to estimate the ratio between the number of electrons that have and have not crossed the mesh, a uniform distribution of electrons is left at the drift region separated 600μm from the cathodes mesh. Their drift is simulated and their final position stored.

The simulations show a complex dependence of the mesh transparency on many parameters, such as: the upper and lower cathode hole radius, their ratio, the upper cathode thickness, the drift field, etc. The mesh transparency can vary from 70% to 95% for the models which have been considered.

4.2.3. Avalanche and signal simulator

We have developed an avalanche simulator code which has been implemented into a script that works in Garfield. The resistive layer effects have been taken into account as well as the space charge. The model describes the avalanche in steps of one micron. At the beginning of each step, the variation of the electric field due to the resistive layer and the space charge is computed and subtracted to the electric field simulated in absence of avalanche. Then, the multiplication is calculated. During each step the electric field is considered constant and therefore, the number of electrons at the end of the step (n_i) is

$$n_i = n_{i-1} \cdot \exp(T \cdot 1\mu m) \qquad (4.\ 1)$$

where T is the Townsend coefficient. After that, the electron velocity and the longitudinal coefficient are simulated. The first one is needed to simulate the timing of the avalanche and the induced signal in the electrodes. The longitudinal coefficient is needed to compute the avalanche spread; also needed to simulate the total pulse. Finally, the induced intensity and charge at each surrounding electrode are simulated using the simulated velocity and the weighting fields.

Resistive anode effects

The resistive anode effects are the reduction the gain due to the multiplication field drop caused by the generation of an electric potential in the resistive layer. This electric potential, that is contrary to the applied on at the anode, is generated by the current present in the resistive layer during the avalanche.

The current in the resistive layer has two different origins. The first one is the induction of current due to the movement of the avalanche electrons [RIEGLER,2002b]. The second one is the direct transport of the avalanche electrons from the avalanche region to the anode plane through the resistive layer. The magnitude of the first effect (10^{-10}A) is much smaller than the magnitude of the second effect (10^{-7}A). Therefore, only the direct current is considered for this simulation. This current depends on the rate of the incoming x-ray and the total charge of the events. This rate dependence of the gain due to the resistive layer has been studied elsewhere [FONTE,1999].

Another effect of the resistive layer exists. It is the charge dispersion in a resistive layer. If the anode layer is connected to the high voltage only through the edges of the layer [KHAZINS,2004] the deposited charges leave the anode plane following a large path on the layer surface with a given velocity [DIXIT,2004]. The accumulation of the charges of many events reduces the multiplication field. In this case, the surface resistivity plays the most important role. This effect is not relevant in the MRMC because the resistive layer is connected to the anode over the whole surface.

Space charge effect

The space charge effect is the variation of the electric field in the multiplication region due to the presence of the electrons and ions [LIPPMANN,2001]. The electric field in the different zones of the avalanche is different because it is affected by different charge distributions. In order to simulate the space charge effect, three assumptions are made.

The first one is to consider only the effect of the ions. The electron cloud has a symmetric shape. Due to the electric field that the electrons produce, the electrons in the front part of the avalanche are more accelerated downwards but the ones in the rear part are less accelerated; the overall effect on the gain is approximately zero.

The second approximation is to consider that the ions are fixed on their ionization position. This assumption is already used by other groups [LIPPMANN2004a] and it is justified since the ion drift time is ~10μs and the complete avalanche development takes ~2ns.

The last assumption is to consider that the increment of the avalanche is constant. This is true for the major part of the process because the avalanche grows in saturation (see **Figure 4. 21**).

With the three approximations, the space charge can be described as

$$Space\_Ch\arg e \cong \sum_{step} Eions_{step} \cong \sum_{step} \frac{e^-}{4\pi\varepsilon} \cdot \frac{N_{step}}{\left(r_{step}\right)^2} \qquad (4.\ 2)$$

where $Eions_{step}$ is the electric field produced by the ions generated in one step, N_{step} is the number of ions produced in one step and r_{step} is the distance of the ions of one step to the avalanche. Due to the assumption of a constant growth of the avalanche, N_{step} is constant and thus

$$\sum_{step} \frac{e^-}{4\pi\varepsilon} \cdot \frac{N_{step}}{\left(r_{step}\right)^2} = \frac{N_{step} \cdot e^-}{4\pi\varepsilon} \sum_{step=1}^{step=300} \frac{1}{\left(r_{step}\right)^2} \qquad (4.\ 3)$$

The sum of r^{-2} from 1 to few hundreds, tends to a value 1.6.

$$E_{Avalanche} = \frac{N_{step} \cdot e^{-}}{4\pi\varepsilon} \cdot 1.6 \qquad (4.\ 4)$$

Avalanche of one electron

We first simulate the avalanche produced by one primary electron. The avalanche simulation with and without the resistive layer or the space charge effects is shown in **Figure 4. 21**. It can be seen that the reduction due to the space charge is larger than the one due to the resistive layer. Nevertheless, the resistive layer effect is present during all the process because it is produced mainly by other events; consequently, it is more important at the first steps of the avalanche.

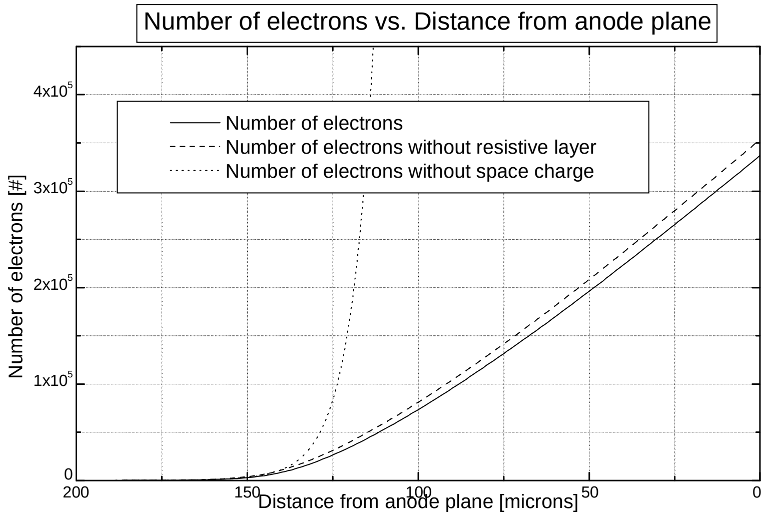

Figure 4. 21 Evolution of the number of electrons during the avalanche. The x-ray energy is 10keV, the gas mixture is Xe 80% + CO_2 20% and the local count rate is 10^5 Hz/mm2.

The resistive layer effect depends on the local count rate and the resistivity of the layer. We show in **Figure 4. 22** the simulated gain as a function of the local count rate using a layer resistivity of $2.25 \cdot 10^5 \Omega \cdot$cm. It is also show experimental data of a similar detector with a resistivity of $4 \cdot 10^7 \Omega \cdot$cm [FONTE1999a] and our simulation of that device. The good agreement between the experimental data and the simulations supports this simulation model.

The multiplication field intensity has a maximum value; which is found experimentally. Higher values produce the arising of sparks. In the literature it can be found that similar detectors can work at multiplication field intensities up to 10^5 V/cm. However, for every single detector this value can only be found experimentally depending on the geometry, cleanliness, purity of the gas… The gain as a function of the applied anode voltage is simulated for two gas mixtures (see **Figure 4. 23**). This simulation is not used to decide the value of the MRMC multiplication field but it is very useful for the operation of the detector.

The induced pulses at the anode, upper and lower cathodes for an avalanche of one primary electron are simulated (see **Figure 4. 24**). Their corresponding induced charge is: 15.3fC anode; 5.8fC upper cathode and 3.9fC lower cathode.

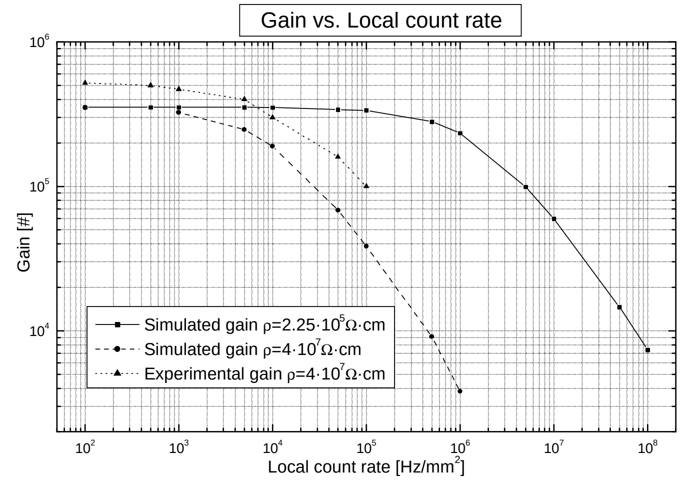

Figure 4. 22 Gain as a function of the local count rate. The x-ray energy is 10keV and the gas mixture is Xe 80% + CO$_2$ 20%.

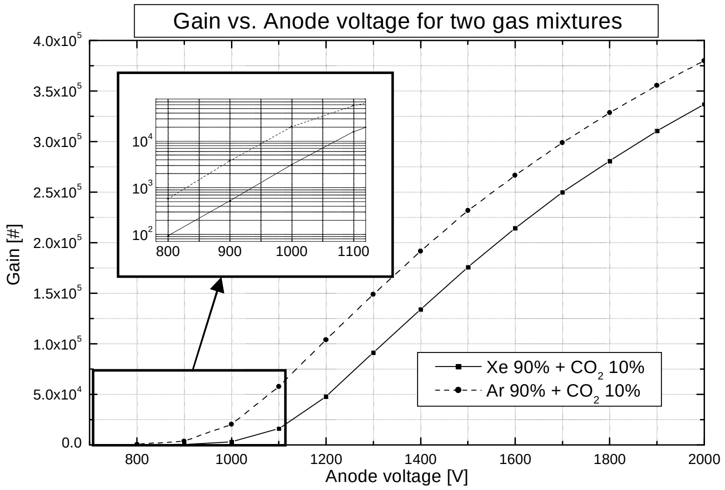

Figure 4. 23 Gain as a function of anode applied voltage for two gas mixtures: Xe 80% + CO2 20% and Ar 80% + CO2 20%. The x-ray energy is 10keV and the local count rate is 105 Hz/mm2.

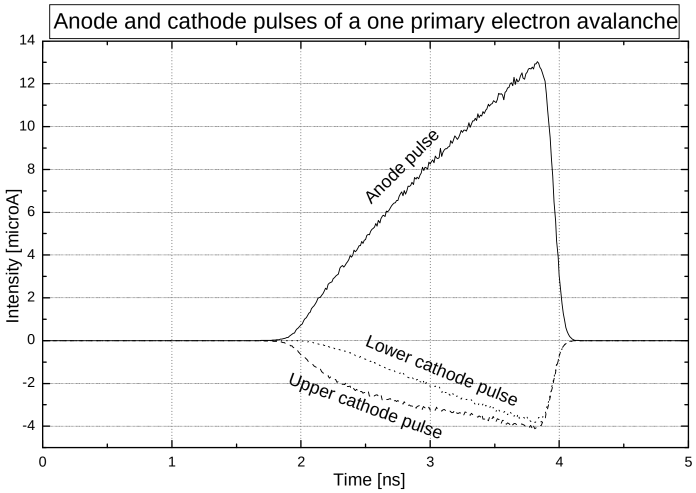

Figure 4. 24 Induced pulse at upper and lower cathode strips close to the avalanche and at the anode. The x-ray energy is 10keV, the gas mixture is Xe 80% + CO2 20% and the local count rate is 10^5 Hz/mm2.

Signal of one event

The objective of this chapter is to simulate the signal induced at the electrodes of the chamber during an x-ray detection. Similarly to the MWPC, the event signal is the addition of signals induced by the avalanches started by that the primary electrons that have reached the anodes region. Using the spatial resolution simulator, the number of primary electrons arriving to each hole is simulated (see **Figure 4. 25**).

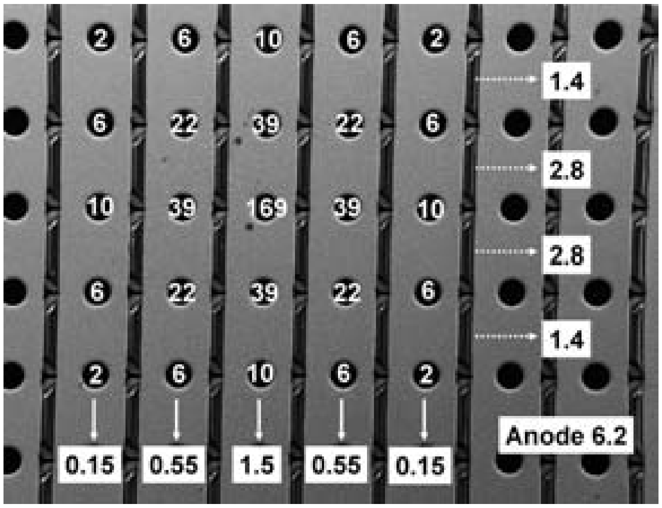

Figure 4. 25 Simulation of the number of electrons arriving at each hole (numbers in white) and induced charge at each strip (numbers in black; [pC]). The induced charge at the anode is also shown. The x-ray beam is on a hole, its energy is 10keV, the gas mixture is Xe 80% + CO_2 20%, the drift distance is 2cm and the local count rate is 10^5 Hz/mm^2.

The intensity signal at each electrode is approximately a Gaussian with a FWHM=20ns and area equal to the charge generated. The charge generated at each strip is much higher than the required by the parallel electronics (~8fC see chapter 3). This indicates the possibility of working at less gain.

4.2.4. Ion drift

In this subsection the trajectories the avalanche ions follow to escape from the multiplication process are simulated, as well as their duration; the ion drift time.

The simulation of the ions paths is related to the ion feedback (see subsection 2.6.2). It has to be guaranteed that the ions do not finish their paths on a cathode surface which faces the multiplication region (see **Figure 4. 26**). The ion paths origin extends along the volume that the avalanche covers during the multiplication process.

The ion drift time is simulated (see **Figure 4. 27**). The ion drift velocity is much higher in the multiplication region than in the drift region because it is proportional to the electric field intensity; which is ~10^5V/cm and ~10^3V/cm in that order. The local count rate of the optimized MRMC is estimated from the ion drift time and the size of the primary electron cloud at the mesh.

$$lcr = \frac{1}{ion\_drift\_time \cdot event\_area} = \frac{1}{2\mu s \cdot 4mm^2} = 1.25 \cdot 10^5\, Hz/mm^2$$

where the ion drift time is 2µs and the event area is $4mm^2$; 5x5 holes.

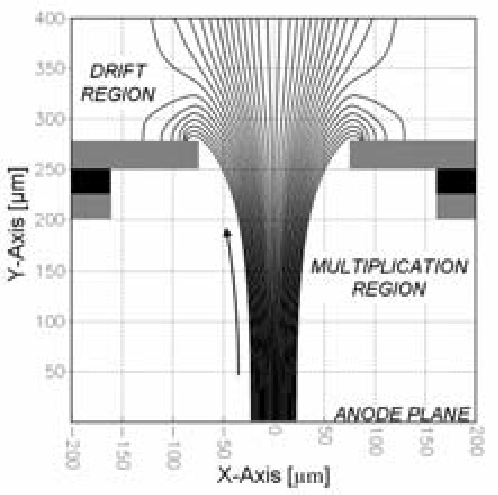

Figure 4. 26 Simulated paths of the avalanche ions drifting to the mesh and to the window. The arrow indicates the ions drift direction.

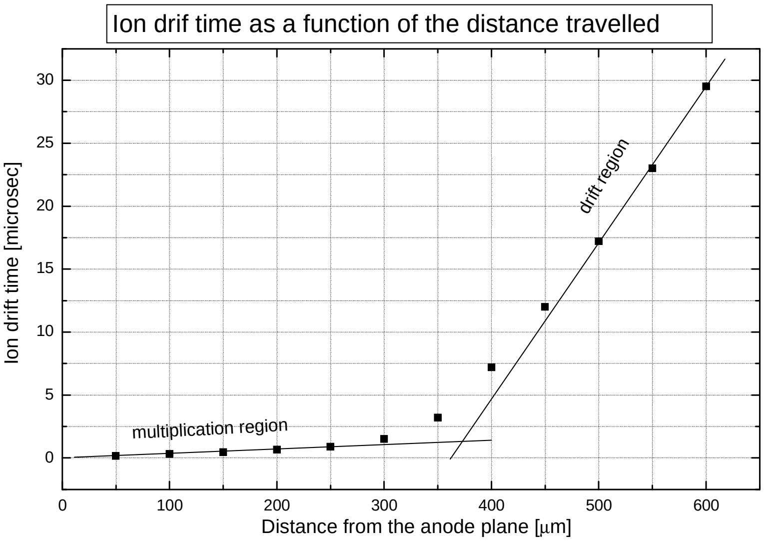

Figure 4. 27 Ion drift time as a function of the distance from the anode plane.

4.3. Capacitances

In this section the simulations of the different capacitances of the detector are shown. They are the strip to anode capacitance, which is related to the signal noise, and the strip to strip capacitance, which is related to the crosstalk. This study had to be done in order to evaluate the magnitude of these effects as a new structure is considered. This work has been done in collaboration with the Electronics Engineer Department of the Universitat Autònoma de Barcelona (UAB).

4.3.1. Strip to anode capacitance

The cathode pulse noise is an important parameter regarding on the spatial resolution and detection efficiency. Low values of the noise of the cathode pulses make the localization of the event more precise and prevent also the pulse signal to be shrouded from the electronics by the noise. These implications are valid for both readout methods: parallel and delay line.

The origin of this noise is mainly due to the detector capacitance and the leakage current [RADEKA1988]. The detector capacitance that induces noise on the cathode pulses is the capacitance between the anode and each cathode strip.

The standard deviation on the charge pulse measurement; the Equivalent Noise Charge (ENC), can not be simulated from the strip to anode capacitance. However, we can introduce some restrictions to the value of the strip to anode capacitance. Typical values of this capacitance in MPGD vary from 100fF to tens of pF having an ENC from ~50 e rms to 10^3 e rms [GERONIMO2001]. The parallel readout requires a strip to anode capacitance lower than 20pF [HERVE2004a]. As a consequence we impose a maximum of 20pF for the value of the strip to anode capacitance.

The Agilent Momentum software [AGILENT2004] has been used for these simulations. Due to the limitations of the program, the computation of the capacitances has been done without taking into account the dielectric material between the cathode planes. This approximation is justified since the region where the capacitance takes place is mainly in the multiplication region and also in the hole region; both without dielectric material.

The simulation of the whole detector is impossible due to the very time consuming calculations it involves. The capacitor transmission as a function of the frequency is simulated. In the simulations of a low number of cells, the capacitor transmission adjusts to a model of a pure condenser (see **Figure 4. 28**). However, when higher frequencies or large number of cells are considered, the pure response capacitor is distorted by inductive effects. The pure condenser behavior is valid at our frequencies domain <1GHz.

The capacitances per unit cell between an upper cathode strip and the anode ($C_{upp/cell}$) and between a lower cathode strip and the anode ($C_{low/cell}$) have been computed (see **Figure 4. 29)**. These simulations have been done for different detector sizes in order to extrapolate $C_{upp/cell}$ and $C_{low/cell}$ for the complete detector.

$C_{upp/cell}$=2.5fF and $C_{low/cell}$=1.32+0.0345·(nº of cells). Therefore, for a detector with 128x128 cells, C_{upp}=320fF and C_{low}=734fF. A detector with 500x500 cells (20x20 cm^2), C_{upp}=1.25pF and C_{low}=9.28pF; what suits the parallel readout condition C<20pF. Consequently, a ENC<10^3 rms e in the upper and the lower cathode strips is expected.

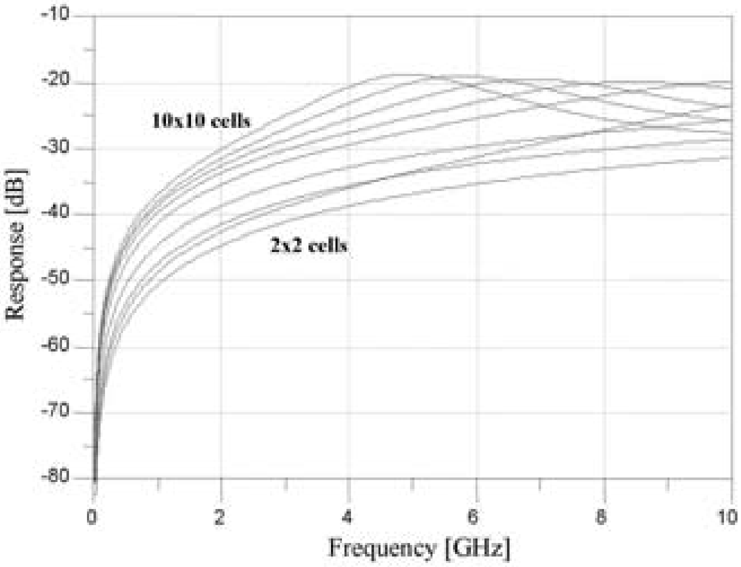

Figure 4. 28 Frequency response of the lower strips. The simulations from 2x2 cells to 10x10 cells are shown. The other strips and the anode are grounded through a 50Ω resistor.

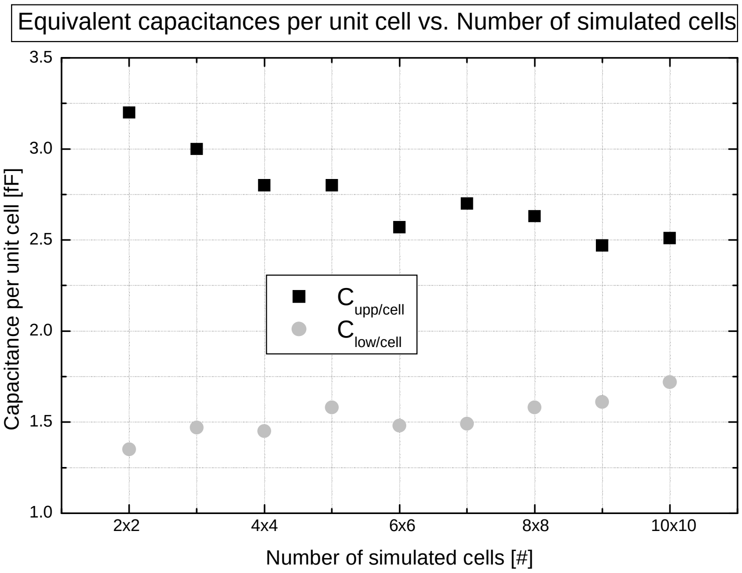

Figure 4. 29 Equivalent capacitances per unit cell as a function of the number of cells simulated.

4.3.2. Strip to strip capacitance: crosstalk

The crosstalk is generated by the strip to strip capacitance and it can worsen the spatial resolution of the detector. We study in this section the induced pulse at neighboring strips when a signal in the time regime of the event pulses is transmitted through one strip.

The effect of applying a squared pulse (amplitude=1V and rise time=10ns) to a strip extreme is simulated (see **Figure 4. 30**). The pulse amplitude of the induced signal at the neighbouring strips has been measured in the simulations (see **Figure 4. 31**).

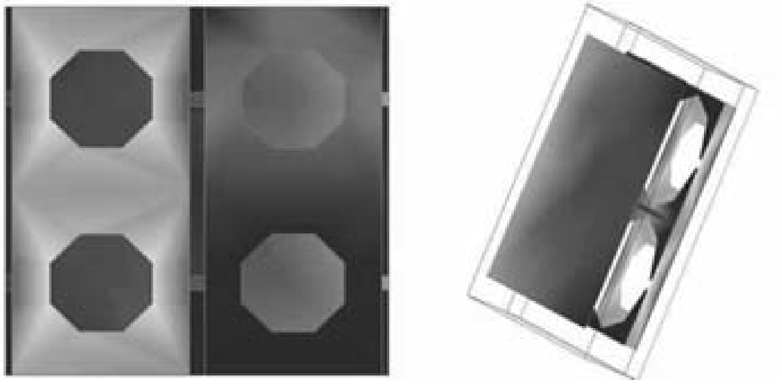

Figure 4. 30 Map of electric potential on the electrodes surface. The bright zones represent the higher electric potential. The upper cathode strips can be seen in the left figure; where the square signal is applied at the left strip. The induced potential at the right strip can be observed. A view from below can be seen in the right figure; where the anode plane and the upper and lower cathode strips can be seen.

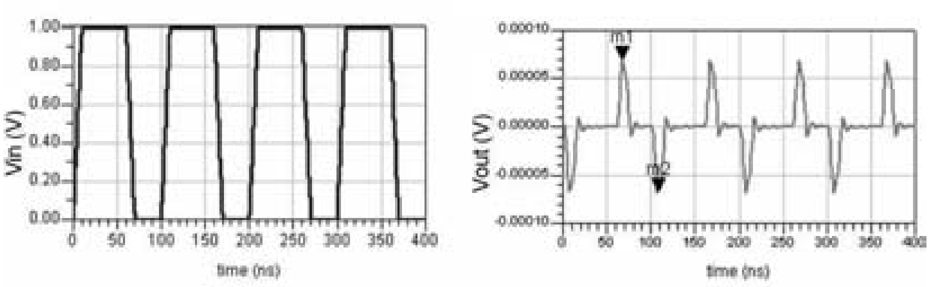

Figure 4. 31 Input pulse (left) and simulated output pulse at the neighboring cathode strip (right).

The crosstalk is proportional to the capacitance between the strips and therefore, it is proportional to the length of the strips and inversely proportional to their separation. Different models with different strip to strip distances are simulated (see **Table 4. 2**). A scaling law is extracted from this simulation.

Strip to strip distance [μm]	Scaling factor
20	1.00
30	0.92
40	0.77
50	0.72
75	0.60

Table 4. 2 Scaling factor of the crosstalk effects as a function of the strip to strip distance. This factor is valid for models similar to the optimized MRMC.

On the other hand, different models with the same strip to strip distance but with different number of cells, a different strip length, are simulated (see **Figure 4. 32** and **Figure 4. 33**). The crosstalk effect amplitude of the whole detector is extrapolated from both simulations.

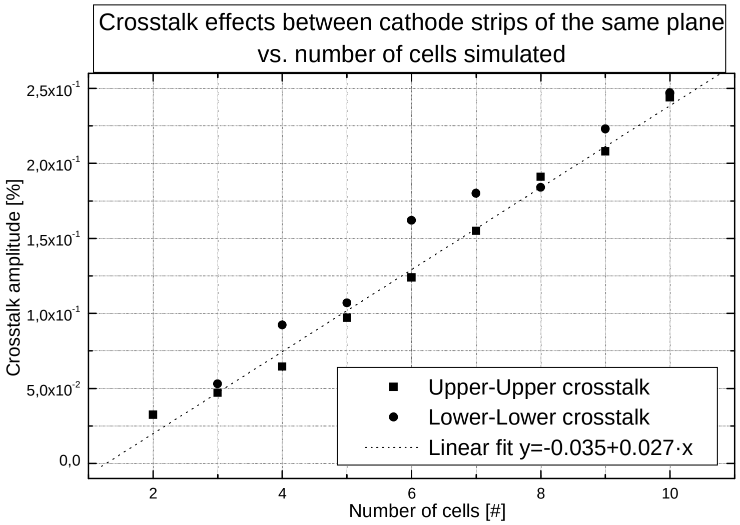

Figure 4. 32 Crosstalk effect amplitude between two strips of the same cathode plane.

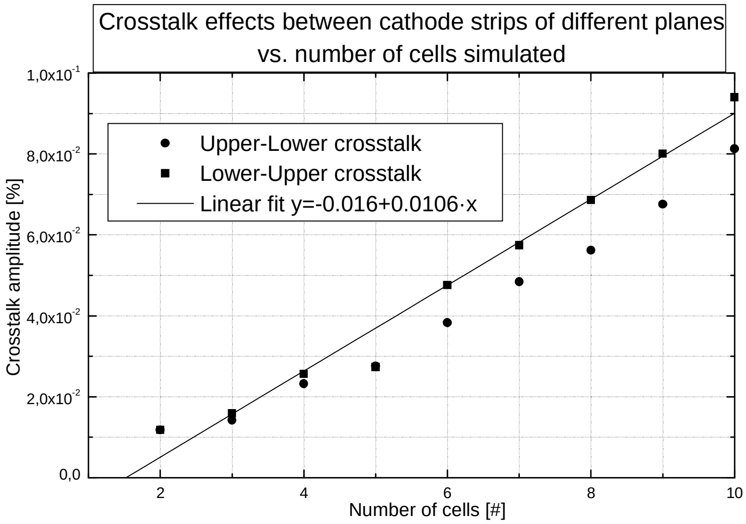

Figure 4. 33 Crosstalk effect amplitude between two strips of different cathode plane. In the upper-lower case, the input pulse is applied to an upper cathode strip and the output pulse is measured to a lower cathode strip.

For the prototype, the simulations shows a maximum crosstalk between cathode strips of the same plane equal to 3%; in the order of magnitude of the noise. Therefore, this effect can worsen the spatial resolution but it allows the good functioning of the prototype. However, the crosstalk can be a main problem if large areas are desired.

The predictions of the simulations must be crosschecked experimentally with the prototype prior to the construction of a large area detector.

5.Optimization

Every parameter of the detector (cathode shapes, distances, sizes, materials, gas mixture, electric potentials,…) influences the detector behaviour. The detector parameters, characteristics and features form a complex net of relationships. For this reason a global optimization is needed to decide the detector parameters. This work is described in this chapter.

In the first section, the relations between the detector parameters and features are described. This knowledge is useful not only for the decision of the parameters, but also to understand the behavior of the detector during its operation.

In the second section, the decision process of the different parameters is described. In it, the explanation of how every parameter has been chosen is given. This process has been done taking into account many different aspects such as the limitations of the building up technique, or the detector goals.

Finally, the optimized detector parameters and its features are summarized in the last section.

5.1. Links between parameters and features

The relations between the detector parameters and features are described in this section. First in subsection 5.1.1, an introduction to the links between detector parameters and features is given. In subsection 5.1.2 the relations between the features and parameters are described.

5.1.1. Introduction to the links between parameters and features

The detector parameters can be chosen/controlled during the design/operation of the detector. They are eight: the gas mixture; the cathodes mesh geometry; the multiplication field; the drift field; the pillars geometry; the cell size; the drift distance; and, the resistivity of the resistive layer. The cathodes mesh geometry includes the cathodes strips shape; the upper and lower cathode holes radius; the layers thicknesses; and, the separation between strips. The pillars geometry includes their height; their radius; and, their density and disposition over the anode surface.

On the other hand, the detector features are seven: the spatial resolution; the count rate; the efficiency; the gain uniformity; the effect of the sparks; the charging up; and, the mechanical instability. The first four features play a role on the quality of the data. The other three are functioning problems; that can inhibit the use of the detector. The effect of sparks includes the rate and intensity of the sparks, and the sparks hardness of the structure.

There is a complex net of relations which involves the detector parameters, characteristics and features. With the only intention of illustrating its complexity, the net is shown in **Figure 5. 1**.

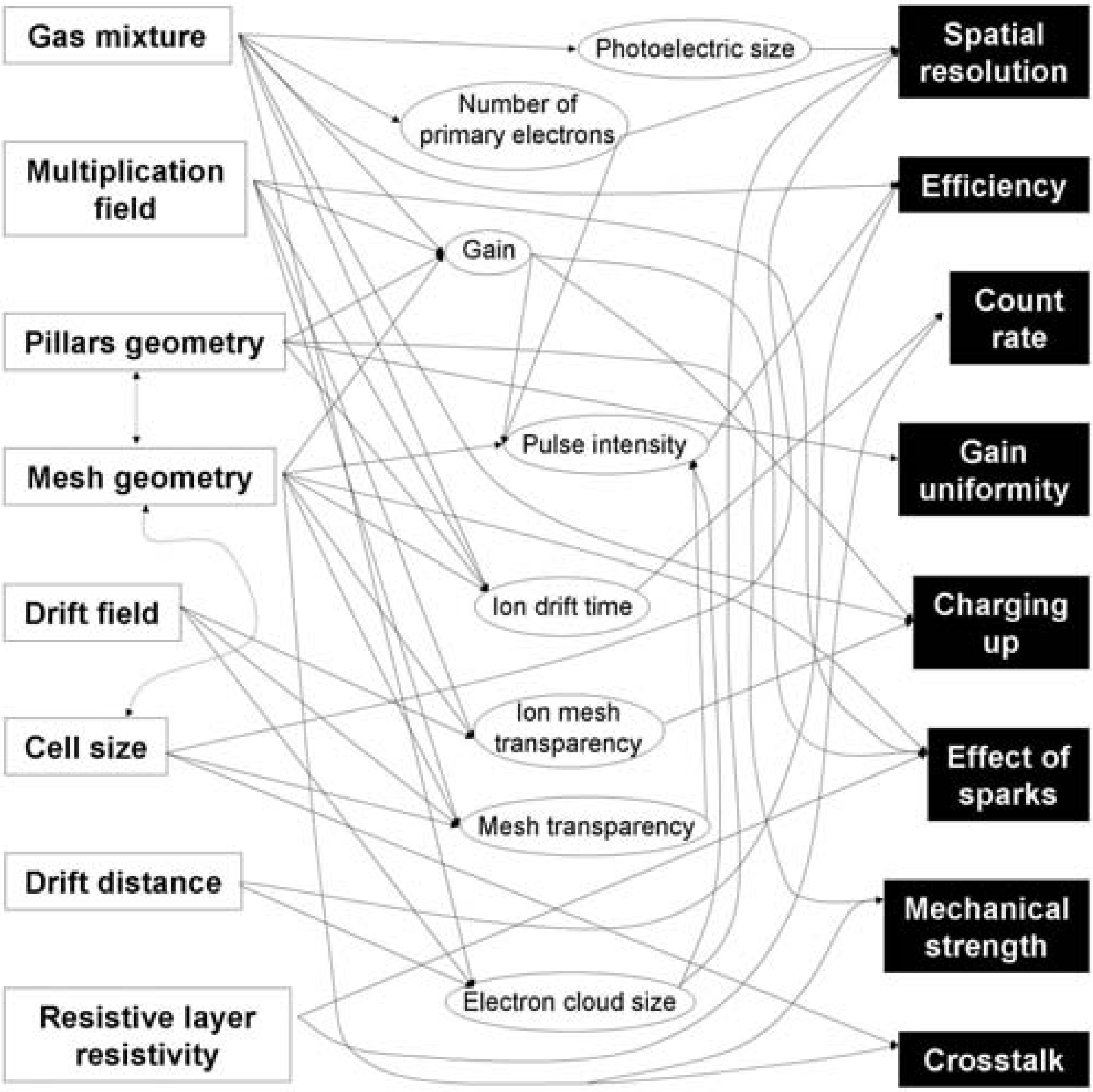

Figure 5. 1 Scheme of the links between the detector parameters (at left in white rectangles) and the detector features (at right in black rectangles). Some characteristics of the detection are shown inside the ellipses.

5.1.2. Features influenced by each parameter

In this subsection, the relations between parameters and features of the MRMC are explained. For this purpose, the consequences that a change on the parameters induces on the features are explained. This is done for the eight different parameters.

In this subsection the characteristics of the detection (electron cloud size, mesh transparency, gain,…) are underlined. The features are in bold and underlined.

Dependences on the gas mixture

The gas mixture is one of the most important parameters of the detector because it plays a role in all the physical processes involved in the detection.

- The probability of interaction of the x-rays with the gas atoms through photoelectric effect depends on the gas mixture. Depending on the noble gas, the quenching gas proportion and the gas pressure, the attenuation length is different. Therefore, the **detection efficiency** depends on the gas mixture (see subsection 2.1.1).
- The photoelectric size, which is determined by the photoelectron mean path, depends on the gas mixture characteristics. It has been seen that the spatial resolution, depends strongly on the photoelectric size. Consequently, the **spatial resolution** depends on the gas mixture (see subsections 2.1.2 and 4.1.2).
- Due to statistical reasons, the **spatial resolution** depends on the number of primary electrons released after the photoelectric effect. This number depends on the gas mixture (see subsection 4.1.2).
- The gas mixture rules the gain through the Townsend coefficient. On the other hand, the detection efficiency depends on the pulse intensity; which depends on the gain. Consequently, the gas mixture characteristics affect the **detection efficiency** (see section 2.3).
- The gain also rules the ion charging up of the detector. Consequently, the gas mixture affects the **charging up**. The charging up can be dramatic if organic gases are used as a quencher (see subsection 2.4.2).
- The gain plays a role on the effects of the sparks because it can increase they probability through the avalanche-to-streamer-to-spark process. Therefore, the gas mixture affects the **effect of the sparks** (see subsection 2.3.2).
- The **count rate** of the detector is affected by the gas mixture since this feature depends on the ion drift time; which is ruled by the ion mobility (see subsections 2.2.1 and 4.2.4).
- The primary electron cloud size at the cathodes mesh is governed by the diffusion coefficients of the gas mixture. The vertical size of the electron cloud size determines the pulse time width. This is important for the maximum pulse intensity, which is related to the **detection efficiency**. The pulse time width is also important for the **spatial resolution** if delay line is used. The transverse cloud size is directly related to the **spatial resolution** (see subsection 3.3.4).

Dependences on the drift distance

The drift distance is the distance between the window and the cathodes mesh. It is defined by the drift spacer.

- The drift distance affects directly the **efficiency** since it conditions the amount of x-rays that interact with the gas (see subsection 4.1.4).
- The drift distance contributes to the determination of the electron cloud size. This affects the **spatial resolution** and the **efficiency**, through the pulse intensity (see the dependences on the gas mixture).

Dependences on the drift field

The drift field is set by difference between electric field potentials of the cathodes (0V) and the window (~1000V).

- The drift field conditions the electron cloud size. This affects the **spatial resolution** and the pulse intensity; which affects the **efficiency** (see the dependences on the gas mixture).
- The drift field also affects the **efficiency** through the pulse intensity since the mesh transparency is affected by the drift field.
- The **charging up** is affected by the drift field since the ion mesh transparency depends on this field (see subsection 2.3.3).

Dependences on the multiplication field

The multiplication field is set by difference between electric field potentials of the cathodes (0V) and the anode plane (~2000V).

- The multiplication field intensity affects directly the **effect of sparks** as the voltage induced sparks are proportional to it. Moreover, a variation on the multiplication field intensity implies a variation on the gain. Consequently, it also affects the **effect of sparks** through the avalanche-to-streamer-to-spark process (see subsection 2.3.2).
- The multiplication field controls the gain and the ion mesh transparency. The **charging up** is directly affected by the ion mesh transparency. It is also affected by the gain since it depends on the generation rate of avalanche ions (see subsection 2.3.3).
- A variation on the multiplication field changes the pulse intensity, as it changes the gain. Consequently, it affects the **efficiency** (see section 2.3).
- The multiplication field intensity determines the ion drift time; which rules the **count rate** (see subsection 4.2.4).

Dependences on the cathodes mesh geometry

The cathodes mesh geometry includes the cathode strips shape; the upper and lower cathode holes radius; the layers thicknesses; and, the separation between strips.

- The cathodes mesh geometry defines the multiplication field during the first steps of the avalanche. Consequently, it plays an important role on the gain; which is related to the **charging up**, the **detection efficiency** and the **effect of sparks** (see the dependences on the gas mixture).
- The position and shape of the cathodes are optimized to enhance the pulse intensity of the induced signal; which affects directly the **detection efficiency**. It also allows a reduction on the multiplication field. The multiplication field affects the **spatial resolution**, the **detection efficiency**, the **count rate**, the **charging up** and the **effects of sparks**. (see the dependences on the multiplication field).
- The mesh geometry affects directly the **effects of sparks** because the sharper the edges end, the more probable the arising of sparks is.
- The ion drift time is affected strongly by the electric field near the cathodes mesh. Therefore, the cathodes mesh geometry affects the **count rate** of the detector (see subsection 4.2.4).
- The trajectories of the avalanche ions are determined by the holes radius and thicknesses of the different layers of the cathodes mesh. The dependence of the ion mesh

transparency on the mesh geometry has a direct impact on the **charging up** of the structure (see subsection 2.3.3).

- Similarly, the mesh geometry determines the mesh transparency (number of electrons that crosses the mesh over number of electrons that arrives to the mesh). The mesh transparency affects the pulse intensity, which is related to the **detection efficiency** (see subsection 4.2.2).
- The **mechanical strength** is determined by the thicknesses of the different layers of the mesh and the surface of contact between layers.
- The **crosstalk** has a strong dependence on both, the distance between cathode strips and the cathode strips thickness (see subsections 2.5.3 and 4.3.2).
- Finally, the strip-to-anode capacitance is determined by the strips geometry; which is included in the mesh geometry. This capacitance rules the **noise** of the induced pulse (see subsections 2.5.2 and 4.3.1).

Dependences on the cell size

The cell size is the distance between hole centers of adjacent mesh holes. It conditions (or is conditioned by) the mesh geometry.

- The cell size affects directly the **spatial resolution** of the detector. This dependence is especially strong if the cell size and the primary electron cloud size at the mesh are similar (see subsection 4.1.8).
- The cell size conditions the mesh transparency. Thus, it affects the **efficiency** through the pulse intensity.
- The cell size determines the area of overlapping between upper and lower cathode strips. This determines the capacitance between upper and lower cathode strips; which determine their **crosstalk** (see subsection 4.3.2).

Dependences on the pillars geometry

The pillars geometry includes the pillars height, radius, density over the anode surface and position with respect to the cathode holes. For a given cell size, the pillars radius determines the maximum hole radius of the lower cathodes; which conditions the upper cathode hole radius. Thus, the pillars geometry conditions the mesh geometry and the cell size.

- The pillars height determines the multiplication distance; which rules the gain. Therefore, it affects the **efficiency**, the **charging up** and the **effect of sparks** (see the dependences on the multiplication field).
- The density of pillars over the anode surface determines the **gain uniformity** because it guarantees the same multiplication distance for every hole.
- The pillars density over the anode surface, height and radius rule the **mechanical strength** of the structure.
- The **count rate** is affected by the pillars height since it conditions the ion drift time. (see subsection 4.2.4).

Dependences on resistivity of the resistive layer

The resistive layer consists on a mixture of conductive material and an epoxy. Its resistivity is controlled by means of the proportion of conductive material in the mixture. It is painted and baked on the anode plane.

- The electric potential difference generated at the resistive layer when a discharge is developing quenches the spark at an early stage. Therefore, the resistive layer resistivity determines the **effect of sparks** (see subsection 0 and 4.2.3).
- The resistive layer affects the **count rate** capabilities of the detector since it can decrease the multiplication field at high incoming rates (see subsection 4.2.3).

5.2. Parameters decision

The process of determination of the detector parameters is described in this section. In order to guarantee the good functioning of the device, the priority has been to reduce the aging effects, the dielectric breakdown and the effect they produce to the structure.

Gas mixture

The best aging resistant gas mixtures for high rate applications are: Ar or Xe + CO_2 (see section 2.4). The use of gas mixtures based on novel gases guarantees a low value of the attachment and recombination coefficients. This characteristic maximizes the number of primary electrons that reach the multiplication zone; minimizing the required multiplication field needed to increase the total charge up to the threshold value. Similarly, the Xe is preferred as its value of W is lower than the one of Ar. Besides, the value of the photoelectric coefficient is higher than the one of Ar. Moreover, the simulations have shown that Xe based gas mixtures perform better spatial resolution than Ar based ones. For these reasons the Xe + CO_2 gas mixture is used.

Typical values of the amount of quench gas vary from 5% to 20%. The MRMC is expected to suffer from photon feedback. Therefore the highest value of quench proportion is chosen: 0.8 Xe + 0.2 CO_2.

Drift

The drift distance and drift field intensity are determined. The drift distance conditions the detection efficiency and the primary electron cloud size. Required by the quality of the acquired data, a minimum efficiency of 50% is needed. However, the larger the drift distance is; the larger the primary electron cloud size arriving to the mesh is; and therefore, the lower the local count rate is. For this reason, the minimum drift distance (2 cm) that fulfills efficiency>50% for the energy range of interest (8-12 keV) is chosen (see **Figure 4. 3**).

For a given gas mixture, the intensity of the drift field determines the transport properties of the charged particles in the drift region. Firstly, it has to be higher than 400V/cm in order reach the plateau velocity of 5cm/μs (see subsection 2.2.1). The primary electron cloud size depends strongly on the transverse diffusion coefficient. The primary electron cloud size arriving to the mesh must be large enough to involve more than one strip in the detection. Otherwise the determination of the event position is not accurate as the readout system can not average the charge of different strips. We consider that, in the case the event is produced on a hole (worst case), the proportion of primary electrons arriving to the central strip can not exceed a 50%. The value of the drift field that matches this condition is ~1000 V/cm.

Multiplication field

The multiplication field is set during operation to the highest value that the detection is not inhibited by dielectric breakdowns. However, it is needed to set a value for the simulations as other parameters depend on it. The typical value for used in similar detectors is used; 10^5 V/cm [BRESSAN1999a]; [ANDRIAMONJE2004].

Cathodes mesh geometry

This group of parameters includes the thickness of the layers, the radius of the upper and lower cathode holes and the separation between strips. The cathode strips must be thicker to typical values (~5µm) in order to resist dielectric breakdowns [BRESSAN,1999a]. The standard of the CERN PCB workshop is used (25µm).

The radius of the upper cathode strip holes must be small because the larger the radius is; the lower the multiplication field in the hole axis is. This radius is set to the fabrication technique limit 75µm (see subsection 3.2.2). The mesh transparency and the ions paths are checked in the simulations showing good results (see next subsection).

The radius of the lower cathode strip holes is chosen in order to match the same induced signal amplitude with the upper cathode one. This criteria determines the value of the lower cathode strips radius: 155µm.

The separation between strips is set to the minimum value that the building technique allows (75µm) for two reasons. Firstly, avoid the electrons to try to cross the mesh between strips; what reduces the mesh transparency. Secondly, avoid the avalanche ions to go to the lower cathode strips separation, charging the device up. The crosstalk effect is checked showing good results (see subsection 4.3.2).

The mesh transparency and the ions paths are influenced by the cathodes mesh geometry parameters. Both are checked in the simulations showing good results (see next subsection).

Cell size

The smaller the cell size is; the better the spatial resolution, the local count rate and the gain are. Therefore, this parameter is set to its minimum possible value. However, there is a geometrical limitation: the lower cathode strips radius plus half of the separation between strips must be smaller than half of the cell size (see **Figure 5. 1**). Therefore, the cell size is set to 400µm [155+(75/2)=(385/2)µm].

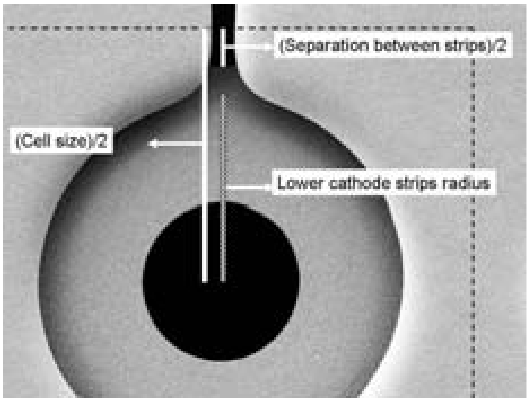

Figure 5. 2 Cell size geometric constrain.

Pillars

Without increasing the multiplication field, the taller the pillars are; the higher the gain is. However, the ratio between the height and the diameter of the pillars is limited by the construction process if vertical walls are desired. The maximum pillars diameter is limited by the space between the lower cathode holes, what constrains the maximum pillars diameter to 125µm. For this diameter, the maximum height of the pillars is equal to 200µm.

Resistive layer resistivity

The resistive layer protects the detector from sparks but also limits its local count rate. The local count rate is also limited by the ion drift time that sets a maximum of $1.25 \cdot 10^5$ Hz/mm^2 (see subsection 4.2.4). The maximum resistivity value that does decrease the gain for local count rates <$1.25 \cdot 10^5$ Hz/mm^2 is $2.25 \cdot 10^5$ Ω·cm (see **Figure 4. 22**).

5.3. Summary of the optimized detector

The parameters of the optimized MRMC are summarized in **Table 5. 1**. The detector features are shown in **Table 5. 2**.

Parameter	Value	Parameter	Value
Drift dist.	2cm	Separation between strips	75µm
Cell size	400µm	Pillars height	200µm
Upper cathode thickness	25µm	Pillars radius	125µm
Dielectric thickness	25µm	Drift field	1000V/cm
Lower cathode thickness	25µm	Multiplication field	10^5V/cm
Upper cathode holes radius	75µm	Resistive layer resistivity	$2.25 \cdot 10^5$Ω·cm
Dielectric holes radius	155µm	Resistive layer thickness	22.5µm
Lower cathode holes radius	155µm	Gas mixture	80% Xe + 20% CO_2

Table 5. 1 Optimized MRMC parameters

Feature	Value	Feature	Value
Detection efficiency (8-12keV)	**>50%**	Anode induced signal	~6.3pC (~0.30 mA)
Number of fired strips	2-3	Upp. cath. induced signal	~2.4pC (~0.12 mA)
Best achievable spatial resolution	**~250µm**	Low. cath. induced signal	~3.2pC (~0.16 mA)
Mesh transparency	~90%	Crosstalk (128x128 strips)	<4%
Gain (local count rate≤10^5 Hz/mm^2)	**~$4 \cdot 10^5$**	Ion drift time	~2µs
Electronic Noise Charge	<10^3e (RMS)	**Local count rate**	**~$1.25 \cdot 10^5$Hz/mm^2**

Table 5. 2 MRMC features. The most important detector features are in bold. The upper and lower cathode induced signal refers to the addition of the signals of all the cathode strips.

According to the simulations, the detector requirements (see **Table 1. 1**) are fulfilled.

6.Experimental tests

The experimental tests, that have been done with the prototype of the MRMC, are described in this chapter that is divided in five sections: characterization; experimental setup; x-ray detection; real prototype simulation; and, conclusions. In the first section the overall manufacture of the structure is evaluated and the geometric parameters are measured. An optical microscope and a *scanning electron microscope* (SEM) have been used for both tasks. In the second section the procedures of cleaning the structures and mounting the prototype are described, as well as the experimental setup for the x-ray detection tests. In the third section the results obtained when detecting the x-rays form the Fe^{55} x-ray source are presented. In the forth section the MRMC is simulated with the geometric parameters of the real prototype and the value of the multiplication field used during the tests. The results of these simulations are compared to the experimental results. Finally, the conclusions of this chapter are presented.

6.1. Characterization

In this section we want to verify the overall manufacture and measure the geometric parameters of the structure. In the overall manufacture of the structure three different issues are inspected: the cleaning; the shape of the structures; and, the state of the structure.

Two sets of pictures of the different parts of the MRMC have been taken. The first set of pictures has been taken with an optical microscope connected to a digital camera. The microscope is a Leica MZ-16; which has a magnification of 150. The overall aspect of the structures is evaluated and some geometric parameters such as the cell size over the whole area are measured. The second set of images is taken with a scanning electron microscope. The magnification of the images varies from 80 to 5000.

6.1.1. Optical microscope images

The images of the optical microscope are shown in this section that is divided in four different collections: cathode mesh from above; cathode mesh from below; anode layer; and, window. The conclusion of each image is shown in its caption.

Cathode mesh from above

In this set of images the upper strips can be observed. The lower strips are observed through the separation between upper strips, as well as the dielectric material (Kapton) that separates the two cathode planes.

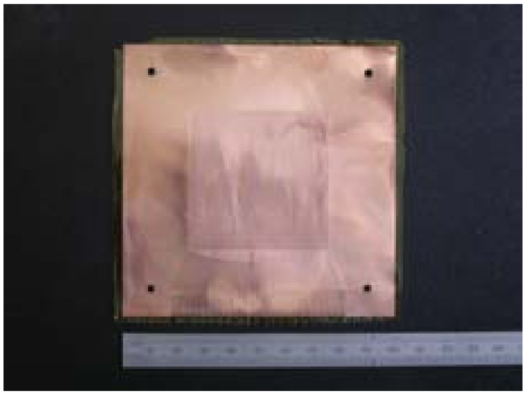

Figure 6. 1 General view of the cathode mesh. The overall aspect is not good because many in-homogeneities are observed. It can be seen that the foil has been blended many times. The structure area is 10x10cm^2 and the active area is 5x5cm^2.

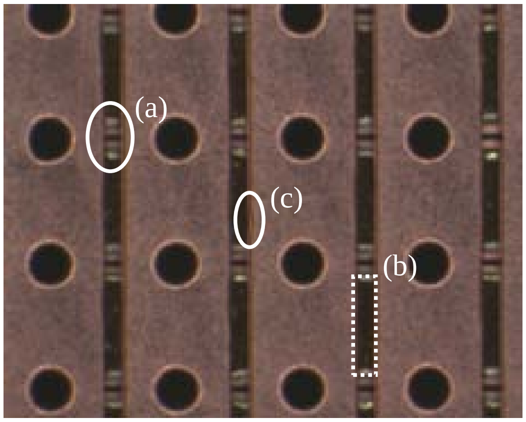

Figure 6. 2 The lower cathode strips separation is observed (a), as well as the dielectric material (Kapton) (b) placed between the two cathode planes. The circles pattern seems to be good defined. The strips separation layout is well defined (it is straight), but it has in-homogeneities (c). The slope of the edge at the separation between strips is observed.

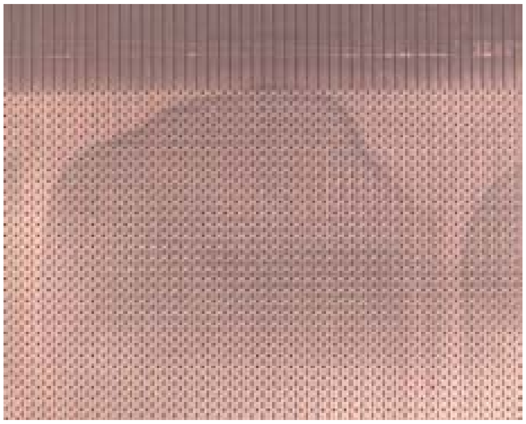

Figure 6. 3 Some regions with different color are observed. It is not known what it is. Some scrapes can be seen.

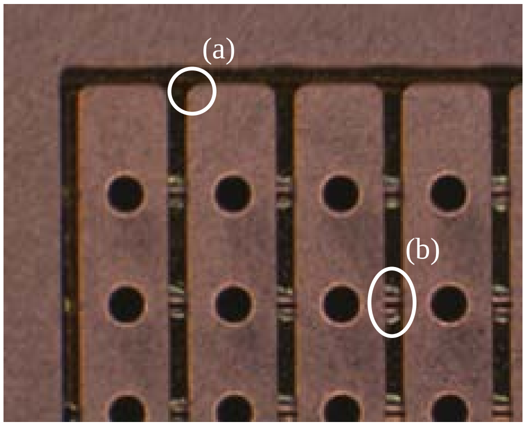

Figure 6. 4 Corner of the cathodes mesh. The edges of the strips have been rounded (a). The under-etching is observed because the Kapton material placed between the cathode planes cover less area than the lower cathode strips (b). The pattern of the Kapton material is not regular (b)

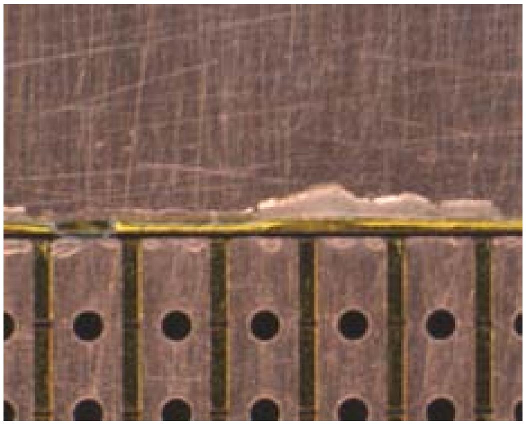

Figure 6. 5 Big in-homogeneities on the copper pattern are observed in some zones of the cathode plane. Many scrapes are also observed. In this zone, the Kapton material is not removed where the upper and lower cathode strips separation coincides (a).

Cathode mesh from below

In this set of images the lower strips can be observed. The upper strips are observed through the separation between upper strips, as well as through the lower cathode holes that have a larger radius compared to the upper cathode ones.

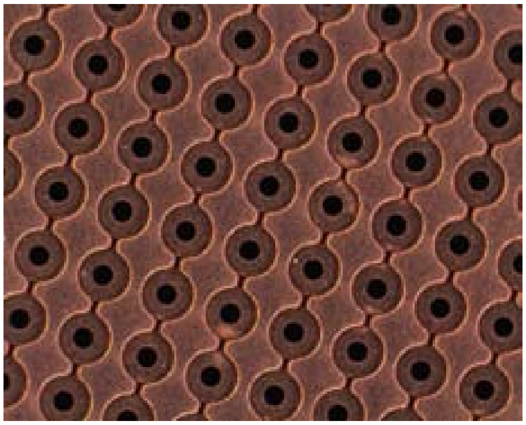

Figure 6. 6 Cathode mesh (view from the anode plane). The general layout is good. The sharp edges have been rounded. Nevertheless, it has some in-homogeneities and zones with different color. No Kapton material is observed due to the under-etching.

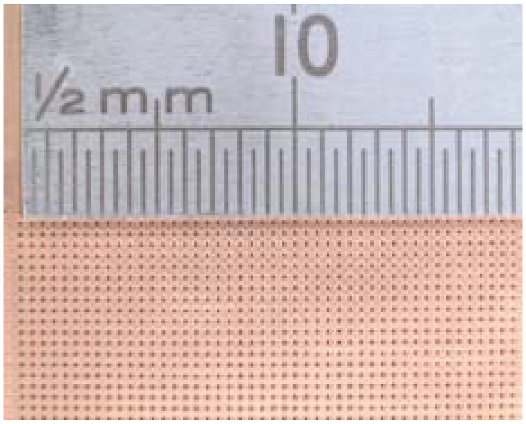

Figure 6. 7 The cell size is well defined (400µm) over the whole area. This measure has been repeated at different zones along the whole structure.

Figure 6. 8 Many in-homogeneities are observed in different zones. There are some deposits on the upper cathode surface which is facing to the avalanche zones. These can cause major problems related to charge up during operation. A better inspection is required.

Figure 6. 9 Similarly to **Figure 6. 5**, the Kapton material has not been completely removed at the edge of the active area. Again, this material can be charged up and produce instabilities during the operation of the detector.

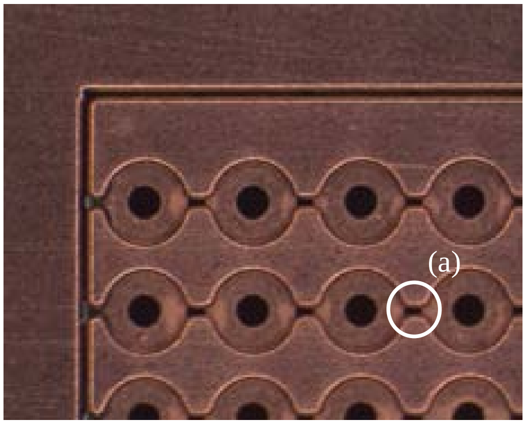

Figure 6. 10 The radius of the lower cathode holes is 155±3µm. The upper and lower strips are not well aligned (a).

Figure 6. 11 Some regions of the surrounding copper material are removed. It seems that it has been chemically attacked.

Anode layer

In this set of images the anode layer is observed. It consists on four parts: the ceramic layer (white); the anode plane (copper) that is not seen; the resistive layer (black); and, the pillars (orange quasi-transparent).

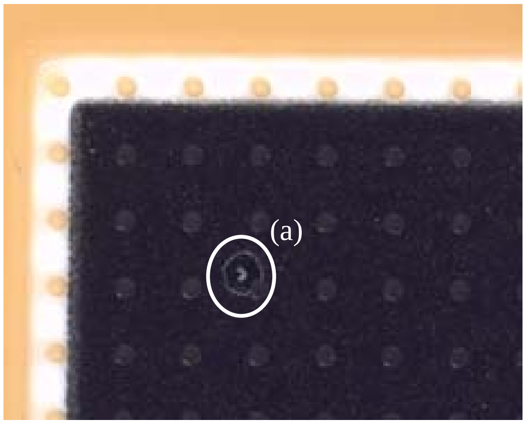

Figure 6. 12 The pillars material is observed (orange) around the active zone. The pillars; which are quasi-transparent, can be seen on the ceramic material and on the resistive layer. The connection of the anode is observed (a).

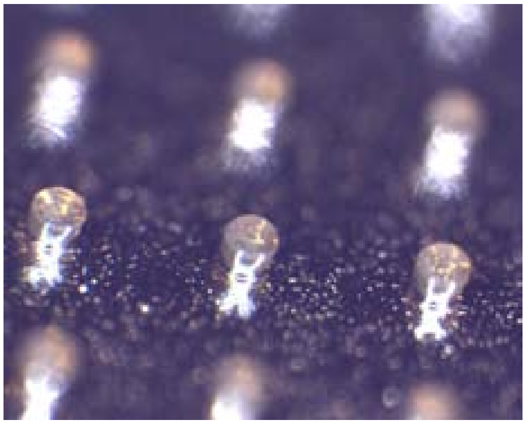

Figure 6. 13 Close view of the pillars on the resistive layer that is tilted for this picture. The pillars shape is well defined and their walls are vertical. The pillars radius is 113µm.

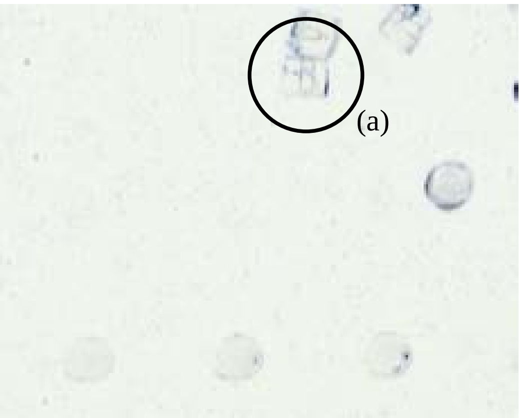

Figure 6. 14 After the use of one prototype, we de-attach the pillars from the resistive layer in order to measure their height. It can be seen that some of them are laying on the resistive layer (a). The negative image is shown in order to enhance the contrast. The pillars height is 210μm..

Window

The window layer is shown separated from the prototype (view from the drift region).

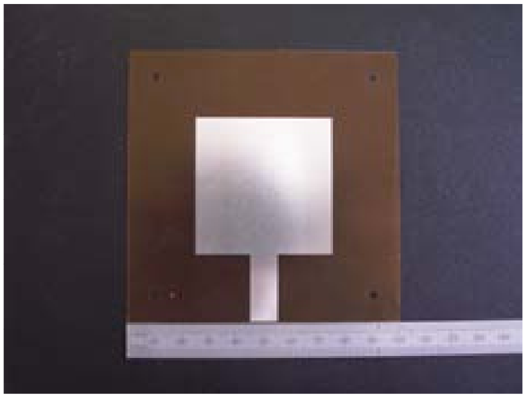

Figure 6. 15 View of the window. The aluminum foil area is 5x5cm^2. The thick track used for the connection to the high voltage can be observed at the lower part.

6.1.2. SEM images

Different images of the cathode mesh structure are taken with a SEM. With it, the details of the defects and the deposits are shown. The anode layer could not be characterized with the SEM because we were not sure if the SEM would be damaged or contaminated.

Cathode mesh from above

In this set of images the upper strips can be observed.

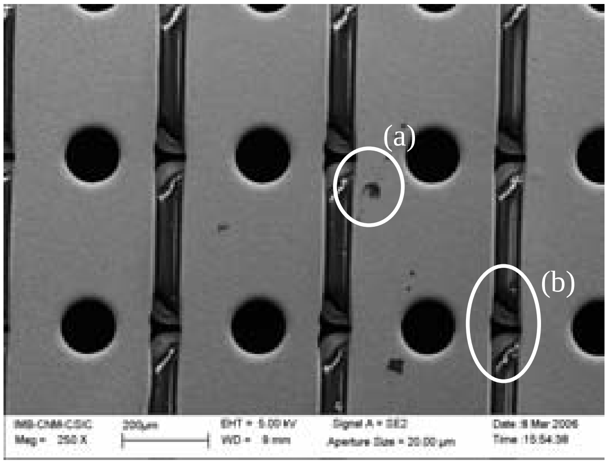

Figure 6. 16 The overall aspect is not good. Many deposited material is observed (a). The upper cathode strips are misaligned with respect to the lower cathode strips (b). We measure this error along the whole surface: 0-25µm. The Kapton material is not under-etched uniformly. The cell size is 400µm ±1µm.

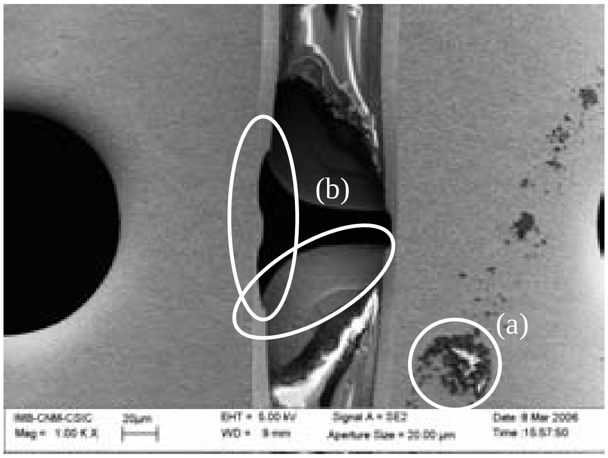

Figure 6. 17 The deposits (a) are formed by dielectric material because, like the Kapton parts, it charges during the electron exposition and it shines in the image. The upper and lower cathode strips are slightly affected by the etching from their other side (b).

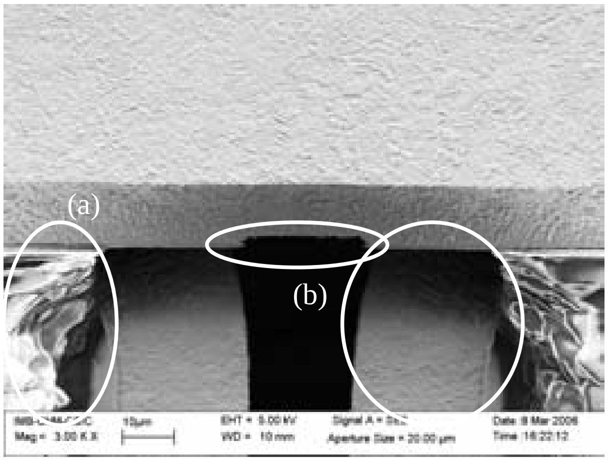

Figure 6. 18 The layered structure of the Kapton material placed between the two cathode planes can be seen (a). The upper and lower cathode strips are slightly reduced when etching from their other side (b).

The observed layout of the upper cathode hole and of the upper strip separation is shown.

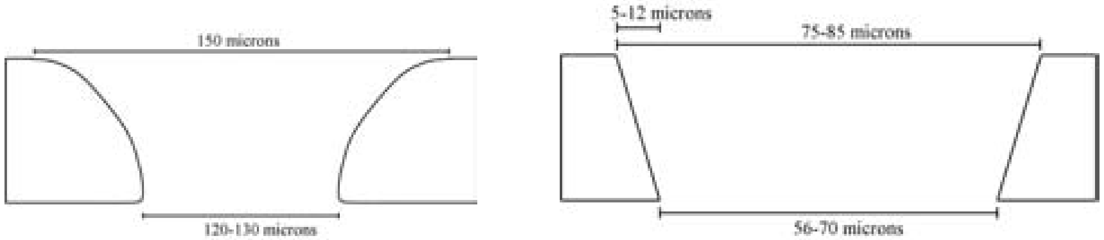

Figure 6. 19 Layouts of the holes (left) and the separation between strips (right) of the upper cathode. The minimum diameter of the upper cathode holes is 120-130µm. In **Figure 6. 22** the desired pattern of the upper cathode strips holes can be seen. The minimum separation between upper cathode strips is 56-70µm.

Cathode mesh from below

In this set of images the lower strips can be observed.

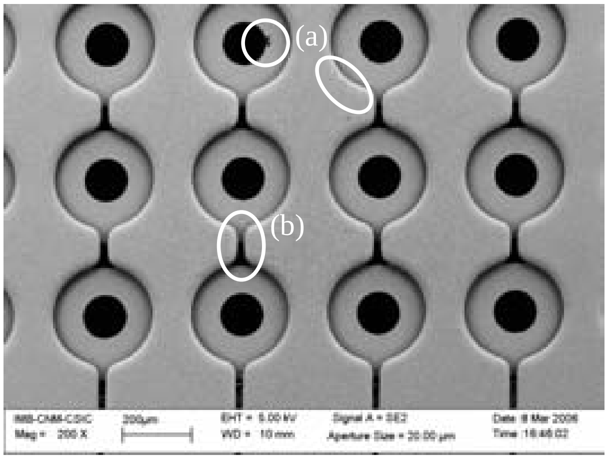

Figure 6. 20 Many in-homogeneities are observed (a). The upper strips are not aligned with respect to the lower ones (b). The radius of the lower cathode hole is 140µm.

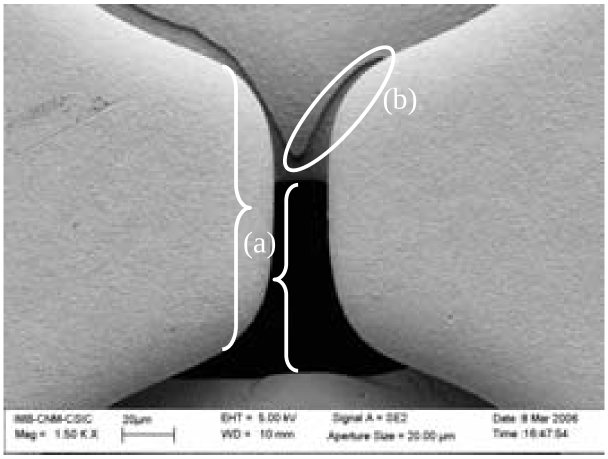

Figure 6. 21 The upper strips are not aligned with respect to the lower ones (a). Some strange shapes can be observed from a close look (b). Some scratches are also observed.

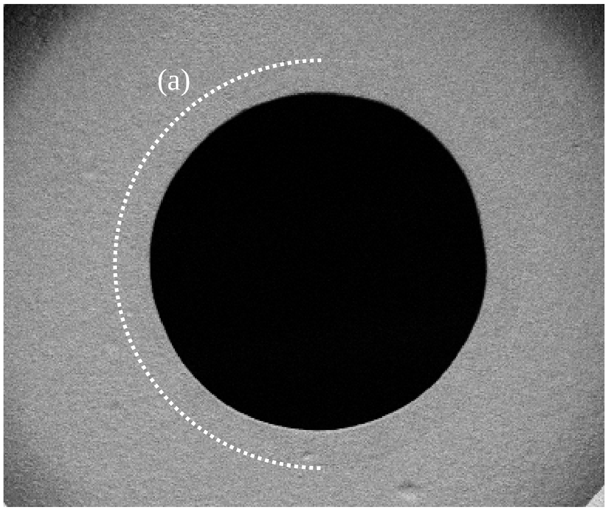

Figure 6. 22 The pattern of the desired upper hole (radius=75µm) is observed (a).

6.1.3. Characterization conclusions

The detector building requirements can be fulfilled using the techniques that have been chosen for the construction of the prototype. Some images show that the shapes can be well defined controlling the different geometric parameters and the structure can be finished without any remaining dielectric material. Moreover the structures are nicely smoothed to avoid sparks. Unfortunately, this is not done in the whole area of the detector.

The prototypes received show three different imperfections that can be worked out. The first one is the overall aspect. More care should be taken when building the cathodes mesh structure in order to avoid the blend of the mesh and the scratches. This is important because the multiplication distance suffers a large variation at the blended zones. The electric field variation can be important near the scratches.

The second aspect that must be improved is the different chemical attack processes that can solve three major issues. The first one is the presence of remaining dielectric material on the cathodes surface. This is a major problem regarding to the charging up of the structure; what can end up in discharges. The second issue that can be solved optimizing the chemical attack processes is the layout of the upper cathode strips. The prototypes that have been received show a smaller upper and lower hole radius, compared to the specified ones. These changes decrease the mesh transparency, the gain and the signal amplitudes. The strange shapes due to the etching of the cathode strips from their other side can be also solved. The third issue is the remaining Kapton seen at the edges of the active area. This material is a problem for the charging up.

Finally, the alignment of the different masks should be improved to solve the misalignment between the upper cathode strips separation with respect to the lower cathode strips and to the upper cathode strips holes.

6.2. Experimental setup

The setups of the prototype and the experiment are described in this section. It is divided in two subsections: prototype setup and experiment setup. In the first subsection, the cleaning and mounting of the prototype is described. In the second subsection, the experimental setup to realize the x-ray detection with the Fe^{55} x-ray source is shown.

6.2.1. Prototype setup

We describe in this subsection the prototype cleaning and mounting procedure.

Cleaning

It is well known that the MPGD are very sensitive to the cleaning and therefore, all the cleaning and mounting process is done in a clean room. It is a class 1000 clean room of the Universitat Autònoma de Barcelona.

The three parts built at CERN were already cleaned when they were delivered. The cathode mesh structure is cleaned in the ultrasound cleaner with ultra-pure isopropanol to ensure its cleanliness. The window and the drift frame are leaned following the same procedure. The anode layer structure is not cleaned following this process because the pillars de-attach from the resistive material (see **Figure 6. 14**). This piece was already cleaned of deposits when it was received. The little dusts are removed using the combination of a paintbrush and a microscope.

Mounting

As described in chapter 3, the different parts are assembled and aligned with four screws which are placed in the holes at the corners of the different layers. The cathodes mesh is stretched before mounting the detector in order to improve its flatness. This is done exploiting the different thermal expansion coefficients of the copper and the material of the drift frame.

The cathodes mesh and the drift frame, that has a much smaller thermal expansion coefficient, are baked to 100ºC. Then they are fixed with an epoxy. When the epoxy is cured, the parts are removed from the oven and their temperature is reduced. Thanks to the different thermal expansion coefficient of the two parts, the mesh is stretched. The temperature is chosen to maximize the stretch of the cathodes mesh without changing the cell size. During this process the pipe with the valve for the gas connection is fixed to the drift frame with the same epoxy.

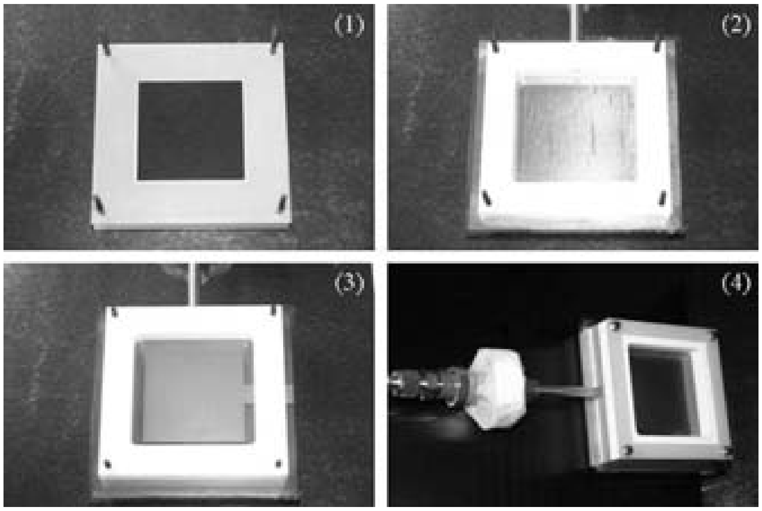

Figure 6. 23 Pictures of the assembly of the prototype. The anode layer can be seen in step (1) with the 4 alignment screws. In step (2) the cathode mesh and the drift spacer can be seen. The gas pipe is fixed to the drift spacer. In step (3) the window and the frame that fixes it are shown. In step (4), the finished assembly is shown. The gas valve connected to the gas mixture bottle can be seen at the left part of the image.

6.2.2. Experimental setup

In this subsection, the experimental setup to carry out the x-ray detection with the Fe^{55} x-ray source is described.

The objective of this experiment is to study the general behavior of the structure when detecting x-rays of 5.9keV that are generated with a Fe^{55} source. This is done monitoring the pulse generated at the anode plane that is larger than the signals induced at the cathode strips. The anode signal is amplified with a commercial preamplifier [FEMTO2005] that generates an output pulse whose voltage is proportional to the input pulse current (gain=10^5 V/A).

The anode can not be directly connected to the input of the preamplifier because it has a high applied voltage. The connection is done in a metallic box through a capacitor (220pF) and a resistor (33MΩ) (see **Figure 6. 24**). The low frequencies of the anode signal are therefore filtered. The cutoff frequency, which corresponds to a -3dB, is equal to $1/(2\cdot\pi\cdot RC)=22Hz$.

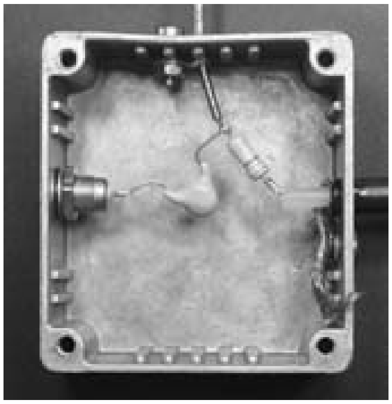

Figure 6. 24 Anode connection box. The upper cable is connected to the anode of the prototype. The cable of the right is connected to the high voltage power supply. The connection at the left releases the input signals to the preamplifier. The wire grounds are connected to the box that is connected to the main ground.

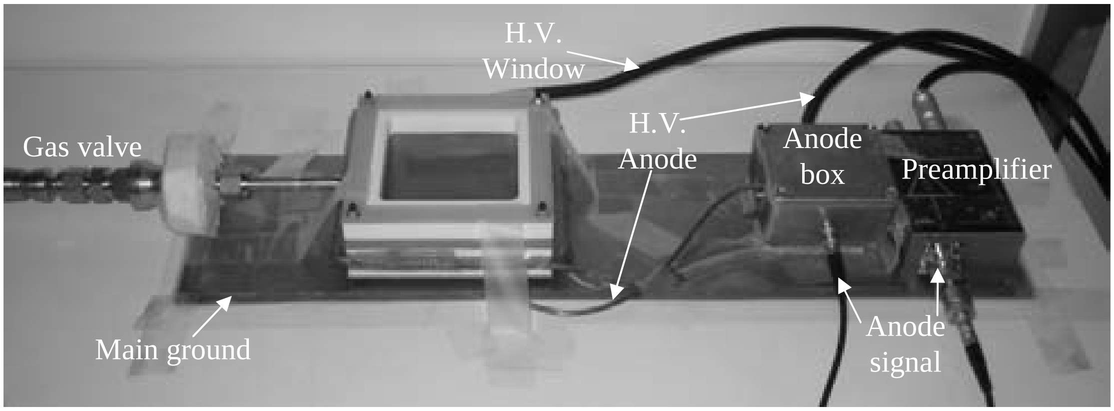

Figure 6. 25 Connections of the prototype.

The window and the anode are connected to the high voltage (H.V.) power supply (see **Figure 6. 25**). The cathode planes are connected to the main ground. For a 2D detection experiment, the cathode strips would be connected to a delay line or to the parallel readout. However, in this experiment we are interested only in the anode signal. The gas valve is connected to the gas mixture with continuous flow.

6.3. X-ray detection

The x-ray detection experience is described here. The first objective of this experiment is to study the general behavior of the structure when irradiating the detector with a Fe^{55} x-ray source. This is done monitoring the pulse generated at the anode plane that is amplified by a commercial transimpedance preamplifier.

Prior to the rise of the high voltages, the signal of the anode is inspected. The electronic noise is extremely high at the output of the preamplifier. A large modulation of the noise with a frequency of 55MHz, that is in the FM radio frequency (30MHz-300MHz), is observed; 200mV peak to peak (p.p.). The detector, the anode box and the preamplifier are shielded with aluminum paper. The noise is reduced to 80mV p.p. For the experience that the group has working with this preamplifier, is known that this noise is still very large. In order to enhance the shielding of the system from the outcoming electromagnetic fluctuations, all the parts are placed inside a metallic box that is grounded. The noise is not reduced. It is deduced that is possible that part of the noise is generated by the ground of the electric network.

The H.V. of the window is decreased to -1000V. The anode voltage is increased until the detector sparks. For anode applied voltages higher than 995V the sparks are very frequent. Big sparks of few µA are observed (they are so large that they can be heard clearly).

The anode voltage is reduced slightly to 983V and the Fe^{55} source is placed on the window. The pulse signal is observed (see **Figure 6. 26**). Some sparks take place from time to time (one per minute approximately). The detector is not destroyed or damaged.

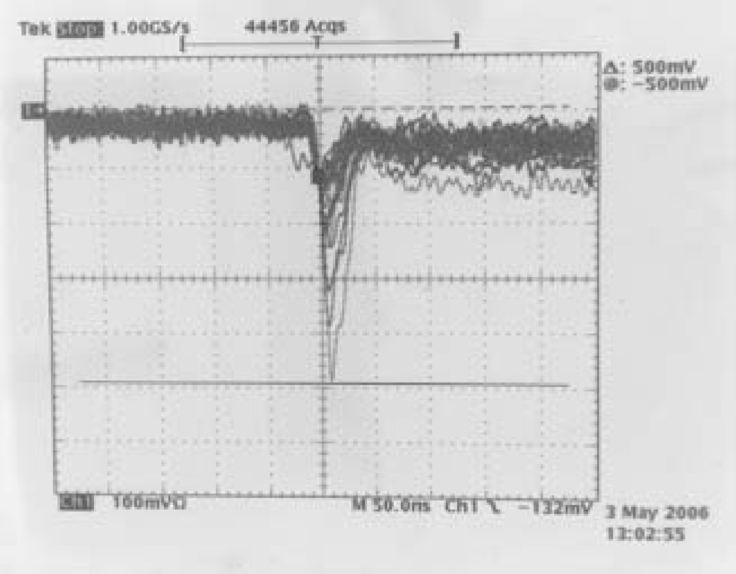

Figure 6. 26 Snapshot of the screen of the scope. Many events are shown at the same time. The trigger is decreased to -132mV in order to see only the event pulses.

In order to study the amplitude of the signals, a *Multi Cannel Analyzer* (MCA) should be used. Comparing and studying the histograms of the pulse amplitudes with and without the Fe^{55} source, the mean event pulse amplitude could be determined. Nevertheless, it is observed that after each pulse the mean level (offset) of the preamplifier output is shifted to large values, compared to the noise amplitude (see **Figure 6. 26**). Therefore the MCA results would not measure the real energy spectrum. The trigger at the scope is varied, and the difference of triggers rate is observed. It is estimated that the major part of the event pulses have an amplitude in the range of -40mV to -60mV. Some events of larger (up to 450mV) amplitudes are observed.

The noise amplitude and the amplitude of the event pulses are overlapped. This makes impossible to distinguish them in the CFD. Therefore, the count rate can not be evaluated. It is also not possible to carry out 2D detections.

After the experiment, the structure is examined with the optical microscope (see **Figure 6. 27**). Many deposits are observed along the whole surface on the upper cathode surface which is facing the multiplication region. They shine with the light of the optical microscope. The zones with different color which were observed during the characterization are not present. The dielectric deposits have been “burned” by the sparks.

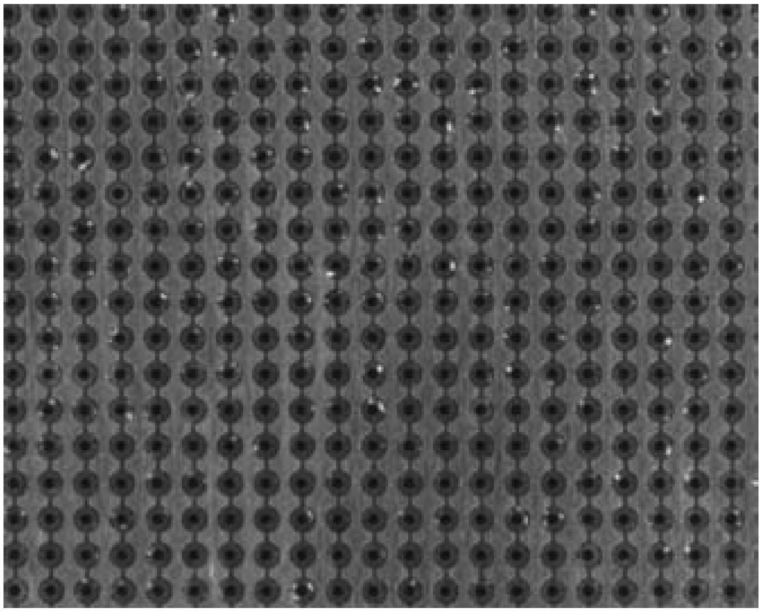

Figure 6. 27 Image of the cathodes mesh structure seen from below; the face that is in the multiplication region is observed. Many bright deposits are observed on the upper cathode surfaces.

6.4. Real prototype simulation

The simulation of the real prototype and the comparison with the experimental results are shown here.

The different geometric parameters of the prototype differ from the optimized ones. The received structures do not fulfill the specifications and therefore the anode applied voltage can not be set to its optimized value. We simulate the structure using the real parameters: the geometric obtained in the characterization work and the anode applied voltage used during the experimental test. The results of this simulation are shown:

- The mesh transparency is 60%. Thus, the number of primary electrons that the avalanche release is equal to $5900keV \cdot \frac{1\_primary\_e}{22eV} \cdot 0.6 = 161\_primary\_e$.
- The gain is 1250 (no saturation).
- The induced charge at the anode plane for an avalanche of one primary electron is $5.27 \cdot 10^{-17}$C and 20ns width.
- The maximum pulse intensity of one event at the anode is 0.42µA.
- The expected pulse amplitude at the output of the preamplifier is $4.2 \cdot 10^{-7}(A) \cdot 10^{5}(V/A) = 42mV$.

The multiplication distance is set by the pillars. However, some blends have been observed in the cathodes mesh foil, and therefore, the multiplication distance in these regions is modified. The simulations show that, for a 10% variation of the multiplication distance (20µm), the gain can differ from 220 to 8800. This corresponds to an expected output pulse variation from 9mV to 352mV.

6.5. Conclusions of the experimental tests

The received structures present some problems that must be solved if a good functioning is desired. The most important defect is the presence of dielectric deposits on the upper cathode surface which is facing the multiplication region. However, the characterization work have shown that process used to manufacture the detector can fulfill the specifications with some improvements.

During the tests, the detector suffers from discharges at a low multiplication field (~$5 \cdot 10^{4}$V/cm), compared to similar designs [FONTE1999a]. The inspection of the structure after the tests (see **Figure 6. 27**) have shown that these are caused by the dielectric deposits that are present on the upper cathode surfaces that are facing the multiplication region. This effect limits the capabilities of the detector and, therefore, the tests that can be done. Consequently, it has not been possible to study the main detector features, such as the count rate or the spatial resolution.

The pulse amplitude obtained with the simulation of the real prototype shows a good agreement with the experimental one. This demonstrates that the avalanche model used for the simulations is adequate. Consequently, one can rely one the expected behavior of the optimized MRMC.

7.Conclusions

A 2D x-ray detector concept and its testing are presented. The device, built with PCB technology, aims to deliver a high local count rate (>10^5Hz/mm^2), to reduce sparking events and to minimize the resulting damage on the electrodes structure. To analyze and optimize the detector, a detailed simulation work has been carried out. Firstly, a Monte-Carlo based program to simulate the spatial resolution as a function of different parameters has been built. Secondly, the three dimensional drifts of ions and electrons near the mesh have been built to simulate the mesh transparency and the ion drift time. Thirdly, an avalanche and signal development code has been developed showing good agreement with experimental data. Finally, the crosstalk and the anode-to-strip capacitances have been simulated to estimate the pulse noise.

A prototype has been built and characterized. The SEM images show that the building technique can fulfill the requirements. However, some geometric parameters do not match the specifications and many dielectric depositions are observed on the cathodes surface.

The testing of the prototype has shown good agreement between the simulated and the experimental gain. This agreement on the space charge calculations demonstrates that the MRMC can deliver local count rates >$1.25\cdot10^5$Hz/mm^2. Moreover, due to the resistive layer and the strength of the structure, the detector survived without noticeable damage. This is a key advantage compared other devices that are very sensible to dielectric breakdowns. However, the detector suffers from discharges because of dielectric deposits on the cathode surface. Therefore, to turn this device into a detector for routine use, it will be necessary to both improve the construction process of the mesh structure and to develop an exhaustive cleaning procedure.

In conclusion, more experimental work have to be done to obtain a spark protected functional detector; for which the simulations predict a high local count rate (>$1.25\cdot10^5$Hz/mm^2) and a good spatial resolution (>250μm).

8.References

[AGILENT2004] http://eesof.tm.agilent.com/products/momentum_main.html.

[AGILENT2005] http://cp.literature.agilent.com/litweb/pdf/5988-3780EN.pdf

[AGILENT2006] http://cp.literature.agilent.com/litweb/pdf/N1996-90003.pdf.

[AKSELA1984] H. Aksela, S. Aksela, and H. Patana, "Auger energies of free atoms: Comparison between experiment and relativistic theory", *Phys. Rev. A*, vol. 30, pp. 858-864, August 1984.

[ANDRIAMONJE2004] S. Adriamonje, S. Aune, E. Ferrer, A Gignaon, Y. Giomataris et.al., " Preamplification structures based on Micromegas" *IEEE Nuclear Science symposium conference record*, vol. 1, pp 461-464, 2004.

[ANGELINI1993] F. Angelini, R. Bellazzini, A. Brez, M. M. Massai, R. Raffo et.al., "The micro-gap camber", *Nucl. Inst. and Meth.*, vol. 335, pp. 69-77, October 1993.

[ALTUNBAS2003] M.C. Altunbas, K. Dehmelt, S. Kappler, B. Ketzer, L. Ropelewski, F. Sauli and F. Simon, "Aging measurements with the Gas Electron Multiplier (GEM)", *Nucl. Inst. and Meth.*, vol. 515, pp. 249-254, December 2003.

[BAMBYNEK1972] W. Bambynek, B. Crasemann, R.W. Fink, H.U. Freund, H. Mark et. al., "x-ray fluorescence yields, Auger, and Coster-Kronig transition probabilities", *Reviews of Modern Physics*, vol. 44, pp. 716-813, October 1972.

[BAROUCH1999] G. Barouch, A. Bay, S. Bouchigny, G. Charpac, J. Derré et-al, "Development of a fast gaseous detector: Micromegas", *Nucl. Inst. and Meth.*, vol. 423, pp. 32-48, June 1999.

[BATEMAN1976] J.E. Bateman, M. W. Waters and R. E. Jones, "Spatial resolution in a Xenon filled MWPC x-ray imaging detector – a computing physics approach", *Nucl, Instr, and Meth.*, vol. 135, pp. 235-249, 1980.

[BATEMAN1980] J.E. Bateman and J.F Connolly, "Imaging of hard x-rays with sub-millimeter spatial resolution by means of a Xenon filled MWPC", *Nucl, Instr, and Meth.*, vol. 173, pp. 525-530, February 1976.

[BELLAZZINI1999] R. Bellazzini, M. Bozzo, A. Brez, G. Gariano, L. Latronico et.al. "The WELL detector" *Nucl, Instr, and Meth.*, vol. 423, pp. 125-134, February 2000

[BELTRAN2002] D. Beltrán and J.A. Perlas, "A fast low noise charge preamplifier for position sensitive detectors" *Rev. Sci. Instr.* vol, 73 (8), pp. 3075-3078, august 2002.

[BERENGUER2005] x-ray diffraction studies of living muscle tissues using synchrotron radiation: Obtaining the structure factor phases for the myosin heads with high time resolution" Master thesis at the Universitat Autònoma de Barcelona, March 2005.

[BERG2000a] F.D. van den Berg, C.W.E. van Eijk, R.W. Hollander and P.M. Sarro "Micro-CAT with redundant electrodes (CATER)" *Nucl, Instr, and Meth.*, vol. 453, pp. 530-535, October 2000.

[BERG2000b] F.D. van den Berg. (2000). Gas-filled micro-patterned radiation detectors. Doctoral thesis. 1st edition.

[BERRY2003] A. Berry, William I. Helsby, Brian T. Parker, Chris J. Hall, Paul A. Buksh, et. al. "The Rapid2 x-ray detection system", *Nucl. Instr. and Meth.*, vol 513, pp. 260–263, November 2003.

[BIAGGI2000] http://consult.cern.ch/writeup/magboltz/

[BIAGI1995] S. F. Biagi and T. J. Jones "The microdot gas avalanche chamber: an investigation of new geometries", *Nucl. Inst. and Meth.*, vol. 361, pp. 72-76, July 1995.

[BONDARENKO1991] V. Bondarenko, V.G, Grigoriev, V.A. Zverev, S.A. Kruglov, A.A. Markina, S. Peskov, V. Portnov and A.A. Sosnovtsev1 "Radiation hardness studies of straw proportional tubes", *CERN-PPE/91-19*, November 1991.

[BOUCLIER1995] R. Bouclier, M. Capeáns, C. Garabatos, G. Manzini, G. Million et.al. "Development of micro-strip gas chambers for high rate operation", *Nucl. Inst. and Meth.*, vol. 367, pp. 168-172, December 1995.

[BOUIANOV2001] O. Bouinanov, M. Bouianov, R. Orava and V. Tikhonov. "Foil geometry effects on GEM characteristics", *Nucl. Inst. and Meth.*, vol. 458, pp. 698-709, February 2001.

[BOUIANOV2004] O. Bouinanov, "The ion trap: a new approach to gaseous microstructure detectors", *Nucl. Inst. and Meth.*, vol. 526, pp. 413-419, July 2004.

[BOYARSKY2003] A.M. Boyarski, "Additives that prevent or reverse cathode aging in drift chambers with helium–isobutane gas", *Nucl. Inst. and Meth.*, vol. 515, pp. 190-195, December 2003.

[BRESSAN1999a] A. Bressan, M. Hoch, P. Pagano, L Ropelewski, F. Sauli, S. Biagi, et al., "High rate behavior and discharge limits in micro-pattern detectors", *Nucl. Inst. and Meth.*, vol. 424, pp. 321-342, March 1999.

[BRESSAN1999b] A. Bressan, R. De Oliveira, A. Gandi, J. -C. Labbé, L. Ropelewski, F. Sauli, et al., "Two-dimensional readout of GEM detectors", *Nucl. Intr. and Meth.*, vol. 425, pp. 254-26, April 1999.

[BRÖNNIMANN2006] Ch. Broennimann, E.F. Eikenberry, B. Henrich, R. Horisberger, G. Huelsen et al., "The Pilatus 1M Detector", *Journal of Synchrotron Radiation*, vol. 13, pp. 120-130, March 2006.

[BYRNE1969] J.Byrne, "Properties of compound Poisson processes with applications in statistical physics", *Physica*, vol. 4, pp. 575-587, March 1969.

[CERN2002] http://technologytransfer.web.cern.ch/TechnologyTransfer/Technologies/chemicalvia/

[CHRISTOPHEL1997] E. Christophel and M. Dracos, "The micro-gap wire chamber", *Nucl. Intr. and Meth.*, vol. 398, pp. 195-195, October 1997.

[CROTTY2003] I. Crotty, P. Fonte, T. Francke, V. Peskov and J. Rantanen, “High-rate, high-position resolution microgap RPCs for x-ray imaging applications ”, *Nucl. Intr. and Meth.*, vol. 505, pp. 203-206, June 2003.

[DICK2004] M. S. Dixit, J. Dubeau, J. P. Martin and K. Sachs, “Position sensing from charge dispersion in micro-pattern gas detectors with a resistive anode”, *Nucl. Intr. and Meth.*, vol. 518, pp. 721-727, February 2004

[DIXIT2004] L. Dick, R. De Oliveira and D. Watts, “FGLD: a noble and compact micro-pattern gas detector”, *Nucl. Intr. and Meth.*, vol. 535, pp. 347-351, December 2004.

[EPSTEIN1998] A. Epstein and C. Boulin, “A fast position encoding system for a delay line based gas filled area detector”, *IEEE Trans. on Nucl. Sci.*, vol. 45 (4), pp. 1931-1933, August 1998.

[FEMTO2005] http://www.femto.de/datasheet/de-hca-40m-100k-c_2.pdf

[FERNANDEZ2004] F. Fernández. “Optimization of a Multi-Wire Proportional Counter” Master thesis at the Universitat Autònoma de Barcelona, November 2004.

[FONTE1997] P. Fonte, V. Peskov and B.D. Ramsey “Streamers in MSGC’s and other gaseous detectors*” ICFA Instrum. Bull.* (online), Fall 1997.

[FONTE1999a] P. Fonte, N. Carolino, L. Costa, Rui Ferreira-Marques, S. Mendiratta, V. Peskov and A. Policarpo, “A spark-protected high-rate detector” *Nucl. Inst. and Meth.*, vol. 43, pp. 154-159, July 1999.

[FONTE1999b] P. Fonte, V. Peskov and B. Ramsey, “The fundamental limitations of high-rate gaseous detecors” *IEEE Trans. Nucl. Sci.*, vol. 46, pp. 321-325, June 1999.

[GERONIMO2001] G. De Geronimo, P. O’Connor, V. Radeka and B. Yu, “Front-end electronics for imaging detectors”, *Nucl. Instr. and Meth.*, vol 47, pp. 192-199, September 2001.

[GIOMATARIS1996] Y. Giomataris, Ph. Rebourgeard, J.P. Robert and G. Charpak, “MICROMEGAS: a high-granularity position-sensitive gaseous detector for high particle-flux environments”, *Nucl. Instr. and Meth.*, vol 376, pp. 29-35, June 1996.

[GUEDES2003] G.P. Guedes, A. Breskin, R. Chechik, D. Vartsky, D. Bar, A.F. Barbosa and P.R.B. Marinho, “Two-dimensional GEM imaging detector with delay-line readout” *Nucl. Inst. and Meth.*, vol 513, pp. 473-483, November 2003.

[HEED1995] http://consult.cern.ch/writeup/heed/.

[HERVE2004a] C. Hervé, http://www.esrf.fr/computing/cs/csel/inhouse/c500/interface/main.html (only available from the ESRF).

[HERVE2004b] C. Hervé, http://www.esrf.fr/computing/cs/csel/released/s110/n110.html.

[HOCH2004] M. Hoch “Trends and new developments in gaseous detectors” *Nucl. Inst. and Meth.*, vol 535, pp. 1-15, December 2002.

[HOHLMANN2002] M. Hohlmann, C. Padilla, N. Tesch and M Titov “Aging phenomena in gaseous detectors – perspectives from the 200, workshop” *Nucl. Inst. and Meth.*, vol 494, pp. 179-193, November 2002.

[IVANIOUCHENKOV1998] I. Ivaniouchenkov, P. Fonte, V. Peskov, R. Ferreira-Marques and A. Policarpo, “The high-rate behavior of parallel mesh chambers*” IEEE Trans. Nucl. Sci.*, vol 45, pp. 258-262, June 1998.

[IVANIOUCHENKOV1999] I. Ivaniouchenkov, P. Fonte, V. Peskov and B.D. Ramsey, “Breakdown limit studies in high-rate gaseous detectors**”** *Nucl. Inst. and Meht.*, vol 422, pp. 300-304, February 1999.

[KANE2003] S. Kane, J. May, J. Miyamoto and I. Shipsey, “An aging study of a MICROMEGAS with GEM preamplification”, *Nucl. Inst. and Meht.*, vol. 515, pp. 261-265, December 2003.

[KATZ1952] L. Katz and A.S. Penfold, “Range-Energy relations for electrons and the determination of beta-ray end-point energies by absorption”, *Rev. of Mod. Phys.*, vol. 24, pp. 28-44, January 1952.

[KHAZINS2004] D.M. Khazind, B. L. Becker, Y. Diawara, R.D. Durst, B.B He, et. al., ”A parallel-plate resistive –anode gaseous detector for x-ray imaging”, *Nucl. Inst. and Meth.*, vol. 51, pp. 943-947, June 2004.

[KNOLL2000] G. F. Knoll. (2000). Radiation Detection and Measurement. (3rd edition).

[KOCSIS2001] M. Kocsis, “The status of gas-filled detector developments at a third generation synchrotron source (ESRF)”, *Nucl. Inst. and Meth.*, vol 47, pp. 103-108, September 2001.

[KRAUSE2001] M.O. Krause, “Atomic Radiative and Radiationless Yields for K and L shells”, *J. Phys. Chem. Ref. Data*, vol 8, pp. 307-327, 1979.

[LABBE1999] [22] J. C. Labbé, F. Gómez, T. Núñez, A. Pazos and P. Vázquez, “The micro slit gas detector” *Nucl, Instr, and Meth.*, vol. 430, pp. 54-59, June 1999.

[LEO, 1994] W. R. Leo. (1994). Techniques for Nuclear and Particle Physics Experiments. (2nd edition).

[LEWIS1994] R. Lewis, “Multiwire Gas Proportional Counters: decrepit antiques or classic performers”, *J. Synchrotron Rad..*, vol. 1, pp. 43-53, 1994.

[LEWIS1997] R. Lewis, W.I. Helsby, A.O. Jones, C.J. Hall, B.T. Parker, et. al., “The “RAPID” high rate large area x-ray detector system”, *Nucl. Inst. and Meth.*, vol. 392, pp. 32-4, June 1997.

[LEWIS2000] R. Lewis, A. Berry, C.J. Hall, W.I. Helsby and B.T. Parker, “The RAPID detector system - first user data”, *Nucl. Inst. and Meth.*, vol. 454, pp. 165-172, November 2000.

[LEWIS2003] R. Lewis, “Position Sensitive Detectors for Synchrotron Radiation Studies: The Tortoise and the Hare?”, *Nucl. Inst. and Meth.*, vol. 513, pp. 172-177, November 2003.

[LIPPMANN2003] C. Lippmann and W. Riegler, “Space charge effects and induced signals in resistive plate chambers”, *Nucl. Instr. and Meth.*, vol 508, pp. 19-22, August 2003.

[LIPPMANN2004a] C. Lippmann and W. Riegler, “Space charge effects in resistive plate chambers”, *Nucl. Instr. and Meth.*, vol 517, pp. 54-76, January 2004.

[LIPPMANN2004b] C. Lippmann and W. Riegler, “Detailed RPC simulations”, *Nucl. Instr. and Meth.*, vol 533, pp. 1-15, November 2004.

[MAGBOLTZ1995] http://consult.cern.ch/writeup/magboltz/.

[MARTINEZ2005] J.C. Martínez, I. Ramos-Lerate, F. Fernandez, D. Beltrán and J. Bordas, “Automatic method to manufacture Multi Wire Proportional counter frames” Proceedings of the 7th international Position Sensitive Detectors at Liverpool, November 2005.

[MUÑOZ2006] M. Muñoz, D. Einfeld and T.F. Günzel “Closed Orbit Correction and Beam Dynamics Issues at ALBA” Proceedings of the EPAC conference at Edinburgh, July 2006.

[NIST2003] http://physics.nist.gov/PhysRefData/XrayMassCoef/ElemTab/z18.html.

[OED1998] A. Oed "Position-sensitive detector with microstrip anode for electron multiplication with gases" *Nucl. Instr. and Meth.*, vol 263, pp. 351-359, January 1998.

[OED2001] A. Oed, "Micro patter structures for gas detectors", *Nucl. Instr. and Meth.*, vol 47, pp. 109-14, September 2001.

[OPERA1998] Vector Fields, Inc. 1700 N. Farnsworth Ave., Aurora, IL 60505.

[PENNING1934] F. M. Penning, "The starting potential of the glow discharge in neon argon mixtures between large parallel plates: II. Discussion of the ionization and excitation by electrons and metastable atoms", *Physica*, vol 1, pp. 1028-1044, May 1934.

[PESKOV2001] V. Peskov, P. Fonte, M. Danielsson, C. Iacobaeus, J. Ostling and M. Walkman, "The study and optimization of new Micro Pattern Gas Detectors for High-Rate applications", *IEEE Trans. on Nucl. Sci.*, vol 48, pp. 1070-1074, August 2001.

[PETRUS2002] A.Yu. Petrus and B.Zh. Zalikhanov "Electro-mechanical properties of narrow-gap multiwire proportional chambers" *Nucl. Instr. and Meth*., vol 485, pp. 399-410, June 2002.

[PITTS1999] W.K. Pitts, M.D. Martin, S. Belolipetskiy, M. Crain. J.B. Hutchins et.al., "Development and operation of laser machined microwell detectors" *Nucl. Instr. and Meth*., vol 438, pp. 277-28, December 2002.

[PITTS2000] W.K. Pitts, M.D. Martin, S. Belolipetskiy, M. Crain. J.B. Hutchins et.al., "Effect of Well Diameter upon MicroWell detector performance" *IEEE. Trans. Nucl. Sci.*., vol 47, pp. 920-922, June 2000.

[PROTEL2004] http://www.protel.com

[RADEKA1988] V. Radeka, "Low-noise techniques in detectors", *Ann. Rev- Nucl Part. Sci*., vol 38, pp. 217-277, December 1988.

[RAMO1939] S. Ramo "Currents induced by Electron Motion" *Proc. IRE.* vol. 27, pp. 584–585, September 1939.

[RAMOS2003] I. Ramos-Lerate, D. Bel0trán, I. Magrans, J.C. Martínez, J.A. Perlas and J.Bordas, "Design, implementation and methods for the manufacture of components of a two-dimensional x-ray detector" *Nucl. Instr. and Meth*., vol 513, pp.197-200, November 2003.

[RAMOS2004] I. Ramos-Lerate, M. Kocsis, J. C. Martínez, D. Beltrán, F. Fernández, "Comparative tests between commercial and in-house transimpedance preamplifiers for multiwire detectors at synchrotron facilities ", *Nucl. Instr. and Meth*., vol 525, pp. 90-97, June2004.

[RAETHER1964] H. Raether. "Electron Avalanches and Breakdowns in Gases" Butterworths, Washington, 1964.

[RIEGLER2002a] W. Riegler and D. Burgardth, "Signal propagation, termination, crosstalk and losses in resistive plate chambers", *Nucl. Inst. and Meth*., vol 48, pp. 130-143, April 2002.

[RIEGLER2002b] W. Riegler, "Induced signals in resistive plate chambers", *Nucl. Instr. and Meth.*, vol 49, pp. 258-27, September 2002.

[RIEGLER2003] W. Riegler and C. Lippmann, "Detector physics and simulation of resistive plate chambers", *Nucl. Instr. and Meth.*, vol 500, pp. 144-162, March 2003.

[RIEGLER2004a] W. Riegler and C. Lippmann, "The physics of resistive plate chambers", *Nucl. Instr. and Meth.*, vol 518, pp. 86-90, February 2004.

[RIEGLER2004b] W. Riegler, "Extended theorems for signal induction in particle detectors VCI 2004", *Nucl. Instr. and Meth.*, vol 535, pp. 287-293, December 2004.

[SARVESTANI1999] A. Sarvestani, H. Amenisch, S. Bernstorff, H.J. Besch, A. Orthen, et. al. “Biological x-ray diffraction measurements with a a noble two-dimansional gaseous pixel detector”, *J. Synchrotron Rad.*, vol 6, pp. 985–994, September 1999.

[SARVESTANI2001] A. Sarvestani, N. Sauer, C. Strietzel, H.J. Besch, A. Orthen, et. al. “Microsecond time-resolved 2D x-ray imaging”, *Nucl. Instr. and Meth.*, vol 465, pp. 354–364, June 2001.

[SAULI1997] F. Sauli “GEM: A new concept for electron amplification in gas detectors”, *Nucl. Inst. and Meht*., vol 386, pp. 531-534, February 1997.

[SAULI1999] F. Sauli and A. Sharma, “Micropattern Gaseous Detectors” Annu. Rev. Nucl. Part. Sci. vol. 49, pp. 341-388, December 1999.

[SAULI2002] F. Sauli, “Micro-pattern gas detectors”, *Nucl. Inst. and Meth.*, vol 477, pp.1-7, January 2002.

[SHEKHTMAN2002] L. Shekhtman, “Micro-pattern gaseous detectors”, *Nucl. Inst. and Meth.*, vol. 492, pp. 128-14, October 2002.

[SHOCKLEY1938] W. Shockley “Currents to Conductors Induced by a Moving Point Charge”, *J. Appl. Phys.*, vol. 9, pp. 635-636, October 1938.

[SLIVINSKY1972] V.W. Slivinsky and P.J. Ebert, “Kβ/Kα x-ray transition-probability ratios for elements 18≤Z≤39” *Phys. Rev. A*, vol. 5, pp. 1581-1586, April 1972.

[TOLEDO2004] J. Toledo, D. Beltrán, J. Bordas, I. Ramos-Lerate, J. C. Martínez, and F. Fernández , “Fast and Compact Data Acquisition for Gas-Filled Detectors With Delay Line” *IEEE Nucl. Trans. and Nucl. Sci*., vol. 5, (4), pp. 1488-149, august 2004.

[THOMPSON2001] Albert C. Thompson, David T. Attwood, Eric M. Gullikson, Malcolm R. Howells, Jeffrey B. Kortright, et. al. (2001) x-ray data booklet (2^{nd} edition).

[TIKHONOV2002] V. Tikhonov and R. Veenhof “GEM simulation methods development”, *Nucl. Inst. and Meth*., vol. 478, pp. 452-459, February 2002.

[TOLEDO2006] J.F. Toledo “THM40” internal report (2006).

[TROW1994] M. W. Trow, A. C. Bento, A. Smith, “Rate dependent image distortions in proportional counters”, *Nucl. Instr. and Meth.*, vol 348, pp. 232-236, September 1994.

[TSUTOMU2005] T. Nagayoshi, A. Takada, H. Kubo, K. Miuchi, R. Orito, et. al. “Simulation study of electron drift and gas multiplication in Micro Pixel Chamber”, *Nucl. Inst. and Meth.*, vol. 546, pp. 457-465, July 2005.

[VEENHOF2001] R. Veenhof, Garfield, A drift-chamber simulation program, CERN Program Library, entry W5050.

[VRA2003] J. Va’vra, “Physics and chemistry of aging-early developments” *Nucl. Instr. and Meth.*, vol 515, pp. 1-14, December 2003.

[VRA2005] J. Va’vra and T. Sumiyoshi, “Ion feedback suppression using inclined MCP holes in a single-MCP+microMEGAS+pads detector” *Nucl. Instr. and Meth.*, vol 553, pp. 76-84, November 2005.

[WALENTA1991] A.H. Walenta, “Proceedings of the European Workshop on X-Ray Detectors for Synchrotron Radiation Sources”, Aussois, France, Sep. 30 - Oct. 4, 1991.

[WEBER1964] K.H. Weber, “Eine einfache reixhweite-energie-beziehung für electronen im energiebereich 3 eV bis 3 MeV” *Nucl. Instr. and Meth.*, vol 25, pp. 261-269, December 1963.

[YEH1985] J.J. Yeh and I. Lindau, “Atomic Subshell photoionization cross sections and asymmetry parameters: 1<Z<103” *Att. Data and Nucl. Data Tabl.*, vol 32, pp 1-155, January 1985.